2002

EXPERIMENTAL INVESTIGATION OF LINEAR BUBBLE DYNAMICS IN A VISCOELASTIC XANTHAN GEL

https://hdl.handle.net/2144/1380

BOSTON UNIVERSITY

COLLEGE OF ENGINEERING

Thesis

EXPERIMENTAL INVESTIGATION OF LINEAR BUBBLE DYNAMICS IN A VISCOELASTIC XANTHAN GEL

by

RYAN DANIEL McCORMICK

B.S., Georgia Institute of Technology, 1999

Submitted in partial fulfillment of the
requirements for the degree of
Master of Science
2002

Approved by

Advisor: ______________________________

Ronald A. Roy, Ph.D.
Associate Professor, Aerospace and Mechanical Engineering

Second Reader: ______________________________

R. Glynn Holt, Ph.D.
Assistant Professor, Aerospace and Mechanical Engineering

Third Reader: ______________________________

William M. Carey, Ph.D.
Professor, Aerospace and Mechanical Engineering

Acknowledgments

This thesis and the work that led to it could not have happened without the help and support of many people. I would like to thank first my fellow graduate students: Preston Wilson for tireless tutelage and being a great friend; Charlie Thomas for many lunch breaks and cool esoteric knowledge; Xinmai Yang, Jinlan Huang, Patrick Edson, Ben Davenny, Eun-Joo Park, Li Liu, Lei Sui, Cory Clarke, and everyone I've unintentionally left out, for illuminating talks, and for being my surrogate family for 2 years.

I would especially like to thank my advisor, Dr. Ron Roy, whose infinite ideas and metaphorical swift kicks to my rear kept me on track and looking at the big picture. Dr. William Carey allowed me to experience experimental situations and knowledge as they are handled in the "real world". Dr. Glynn Holt raised the bar to a higher standard of scientific excellence that, although I tried, I am sure I did not reach. I would also like to acknowledge the professors at B.U. who taught me a great deal through classes or otherwise. I am grateful to the U.S. Navy Office of Naval Research and Boston University who both provided financial support that allowed me to pursue my graduate career.

A large debt of gratitude is also owed to many of my roommates, Matt Giunta, Jose Torres, Ed Hoopman, and Allan Friedman, whose company and silliness has kept me sane on many stressful nights. Friends too numerous to count also deserve mucho credito: particularly Lila Wilson, Amy Wong, and Patrick McCrann — may the best moments of the past be the worst of the future.

Finally, I would like to thank my entire family for supporting me: my Step-Dad and Mom, Richard and Kathy Gunn, my Dad and Step-Mom, Richard and Brigid McCormick, Grandparents Bockes and McCormick, all my brothers and sisters: Allison, T.J., Jon, Andrew, Lauren, and Jack, and the rest of my extended family. In particular, I would like to thank Kent and Maureen Bockes for the rejuvenating trips to New Hope every few months. I would most especially like to thank my sister, Tara McCormick, who is an excellent friend and a wonderful human being.

EXPERIMENTAL INVESTIGATION OF LINEAR BUBBLE DYNAMICS IN A VISCOELASTIC XANTHAN GEL

RYAN DANIEL McCORMICK

ABSTRACT

Oceanic bubble plumes caused by ship wakes or breaking waves disrupt sonar communication because of the dramatic change in sound speed and attenuation in the bubbly fluid. Experiments in bubbly fluids have suffered from the inability to quantitatively characterize the fluid because of continuous air bubble motion. Conversely, single bubble experiments, where the bubble is trapped by a pressure field or stabilizing object, are limited in usable frequency range, apparatus complexity, or the invasive nature of the stabilizing object (wire, plate, etc.).

Suspension of a bubble in a viscoelastic Xanthan gel allows acoustically forced oscillations with negligible translation over a broad frequency band. Assuming only linear, radial motion, laser scattering from a bubble oscillating below, through, and above its resonance is measured. As the bubble dissolves in the gel, different bubble sizes are measured in the range 240 – 470 μm radius, corresponding to the frequency range 6 – 14 kHz. Equalization of the cell response in the raw data isolates the frequency response of the bubble. Comparison to theory for a bubble in water shows good agreement between the predicted resonance frequency and damping, such that the bubble behaves as if it were oscillating in water. (Work supported by U.S. Navy Office of Naval Research)

Contents

List of Tables

List of Figures

Chapter 1

Introduction and Motivation

1.1 Background

Bubbly fluids have been studied for almost 100 years because of the remarkable changes in sound speed and attenuation that even a few bubbles can effect in a volume of water [29, 32]. A typical bubbly fluid has nearly the same density as pure water, but the air bubbles give it a much greater compressibility, in some cases lowering the speed of sound in the mixture to levels lower than the sound speed of air alone. A bubble itself is a resonant oscillator; when a pressure wave of a frequency near its resonance frequency impinges upon it, much of the energy of the wave is transferred from the wave to the radial oscillation of the bubble. The whole process is found often in nature, but not on any scale grander than in the ocean, where it is responsible for the largest portion of ambient noise at the ocean surface. This has not always been known to be the case.

Sound generation mechanisms of ambient noise in the ocean have been debated since World War II. Shipping traffic, sea creatures, seismic activity, and thermal molecular agitation all have been identified as contributions to the total oceanic ambient noise spectrum. However, it has only been recently understood that most sea-surface noise and scattering is caused ultimately by bubbles. Ship wakes and breaking waves entrain air in the upper layers of the ocean in the form of clouds of bubbles. This can have pejorative effects on intentional sound communications, such as propagating sonar pulses, because of the increased attenuation and dramatically lowered and highly dispersive sound speed introduced.

1.2 Literature Overview

1.2.1 Sound Speed and Attenuation

Wood [48] first modelled bubble clouds as acoustically uniform scatterers and treated the bubbly fluid as a continuum. Acoustically uniform in this sense means that the wavelength of sound is much greater than the radii of and spacing between the bubbles. An effective density and sound speed can be calculated using the gas volume fraction, or void fraction, χ, which is the proportion by volume of air, V_a, to the total volume of air plus water,V_w, in the bubbly fluid as shown below

$$\chi = \frac{V_a}{V_a + V_w}. \tag{1.1}$$

The average mixture density, ρ_m, and compressibility, κ_m, can be calculated from

$$\begin{aligned} \rho_m &= \chi\rho_g + (1-\chi)\rho_\ell && (1.2) \\ \kappa_m &= \chi\kappa_g + (1-\chi)\kappa_\ell, && (1.3) \end{aligned}$$

where m stands for mixture, ℓ is for the liquid, and g is for the gas. Using the definition $c^2 = (\kappa\rho)^{-1}$, where c is sound speed with Equations 1.2 and 1.3, we get for the mixture sound speed, c_m,

$$c_m = \left(\left(\frac{\chi}{c_g}\right)^2 + \left(\frac{1-\chi}{c_\ell}\right)^2 + \chi(1-\chi)\left[\frac{\rho_g}{\rho_\ell c_\ell^2} + \frac{\rho_\ell}{\rho_g c_g^2}\right]\right)^{-1/2}, \tag{1.4}$$

which is plotted in Figure 1.1. It is remarkable that, for example, a mixture of 1% air by volume gives rise to a tenfold decrease in sound speed. Note that in the limit of pure water ($\chi = 0$) and pure gas ($\chi = 1$), you recover c_l and c_g, respectively.

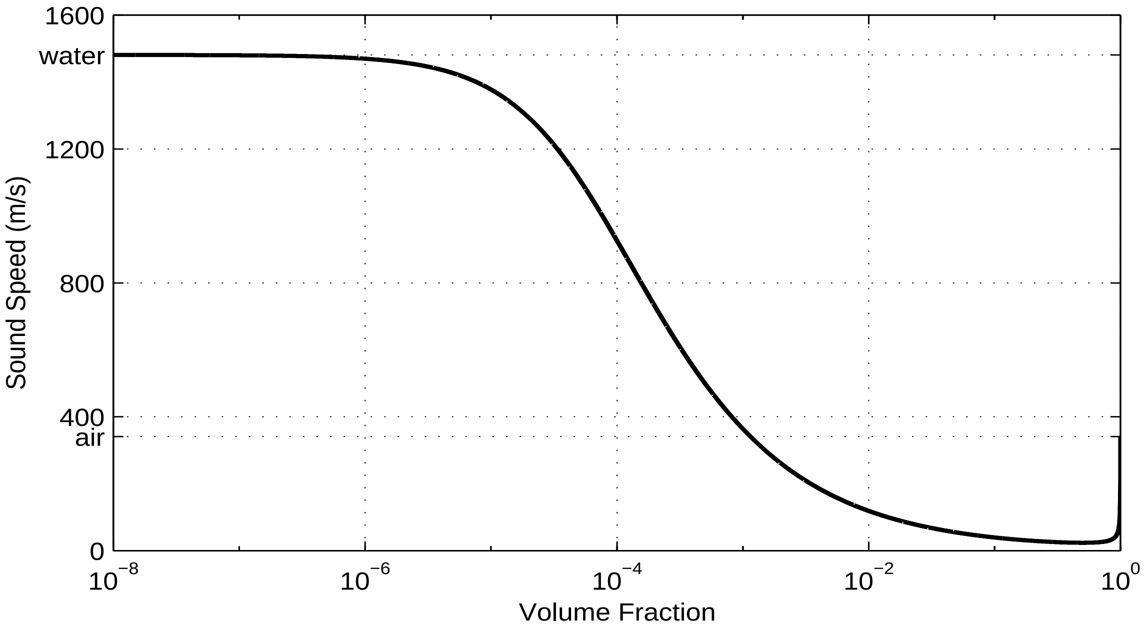

Figure 1.1: Sound speed versus void fraction in bubbly water.

Carstenson and Foldy [7] carried out experiments where the sound speed was measured in an artificially generated bubble column of known void fraction and bubble size distribution. Their experiments verified that bubbles were the primary cause of the dramatic drop in sound speed and increase in attenuation. However, they could not *a priori* determine the root causes of the bubble-enhanced damping they measured from the fluid.

Devin [10] later determined that three mechanisms govern the conversion of vibrational energy to heat in and around the pulsating bubble. The first is thermal conduction between the bubble and the surrounding fluid. It is the dominant mechanism of energy loss for most bubbles, except at very small sizes and high excitation frequencies. Reradiation by the bubble of incident pressure waves is the second loss mechanism and becomes important at frequencies much greater than the bubble's resonance frequency. Viscous losses at the bubble walls due to the surrounding fluid account for the third loss mechanism. This becomes important for small bubbles (on the order of 1 μm radius) driven at high frequencies.

Further study of the thermal damping component was undertaken because under most conditions relevant to oceanic bubbles, thermal conduction is the primary loss mechanism in bubbles [8]. Initial attempts at modelling thermal losses assumed the pressure and temperature field inside the bubble was uniform. Later, Prosperetti [35] removed the assumption of uniform temperature inside the bubble and rederived the thermal component of the damping for linear oscillations. Thermal damping of nonlinear bubble pulsations has been the subject of ongoing study, but as our interest will be in bubbles responding in a linear fashion to incident pressure waves, we shall follow the theory outlined by Properetti.

1.2.2 Bubbles and Low Frequency Ambient Noise 0.2–2 kHz

It is well known that wind plays a significant role in noise generated at the sea surface. Knudsen's [23] famous curves show a marked dependence of ambient noise on sea state, or equivalently the wind speed over the surface, but primarily at frequencies above 500 Hz. In 1962, Wenz [45] published a comprehensive paper outlining the possible sources of noise in the sea. In the absence of manmade traffic noise, there is a broad peak near 500 Hz that could not be explained. Single bubbles that resonate near that frequency would be nearly 1 cm in radius and tend to rise to the surface very quickly. However, plumes on the order of 1 meter in diameter with void fractions of 10^{-2} to 10^{-5} will persist in the turbulent mixing area within 10 meters of the surface.

It was postulated independently by Carey and Bradley [5] and by Prosperetti [36] in 1988 that clouds of bubbles oscillate together coherently, and bubble assemblages can be driven to resonate at a frequency lower than the resonance frequencies of the individual bubbles. This was verified by laboratory experiments [49, 33, 28], as well as by a series of scattering and noise experiments at Lake Seneca in New York [38, 6], where the monopole mode of the collective cloud was measured. Nevertheless, the artificial bubble clouds generated had to be characterized statistically by recording bubbles on videotape and then inferring a volume from nonspherical bubbles that were not in equilibrium [39]. Moreover, the transient cloud was continually changing properties as it rose to the surface. As the static pressure decreased, the bubbles would grow larger and the size distribution would segregate due to different rise times caused by differences in buoyancy.

1.2.3 Bubbles and High Frequency Ambient Noise 2–20 kHz

For higher frequencies in the range 2–20 kHz, wind and rain production of bubbles, as well as turbulent excitation of the volume mode of individual bubbles at the sea surface, are the major contributors to ocean surface noise.

As a rain drop enters the ocean, there is initial radiation from the impact, but then a bubble is formed by pinching off of the cavity formed directly behind the impinging drop [13]. This bubble will exhibit volume oscillations and radiate at its natural frequency.

Similarly, when a wave breaks at the surface in the spilling mode, air becomes entrained to void fractions as high as 20% [27]. Upon formation, these bubbles possess mechanical energy in the form of an initial velocity of the water particles on its surface [36]. This energy is released in the form of volume oscillations at each bubble's particular resonance frequency.

1.2.4 Single Bubble Experiments

Minnaert [32] first described freely oscillating bubbles as damped harmonic oscillators and derived an expression for resonance frequency of the form

$$f_0(R_0) = \frac{1}{2\pi R_0}\sqrt{\frac{3\gamma P_0}{\rho_l}}, \tag{1.5}$$

where R_0 is the equilibrium bubble radius, γ is the ratio of specific heats of the air, P_0 is the equilibrium pressure in the liquid, and ρ_l is the liquid density. This is plotted in figure 1.2 for bubbles of $200 - 500$ μm radius in water. Note that as the bubble gets larger, the resonance frequency drops proportionately. Also, it is equally valid to think in terms of a *resonance frequency* for a given bubble size, or a *resonance size* for a given driving frequency. For example, a bubble that is being driven below its resonance frequency can also be said to be smaller than resonance size. In this thesis, we employ the concepts of resonance frequency and size interchangeably.

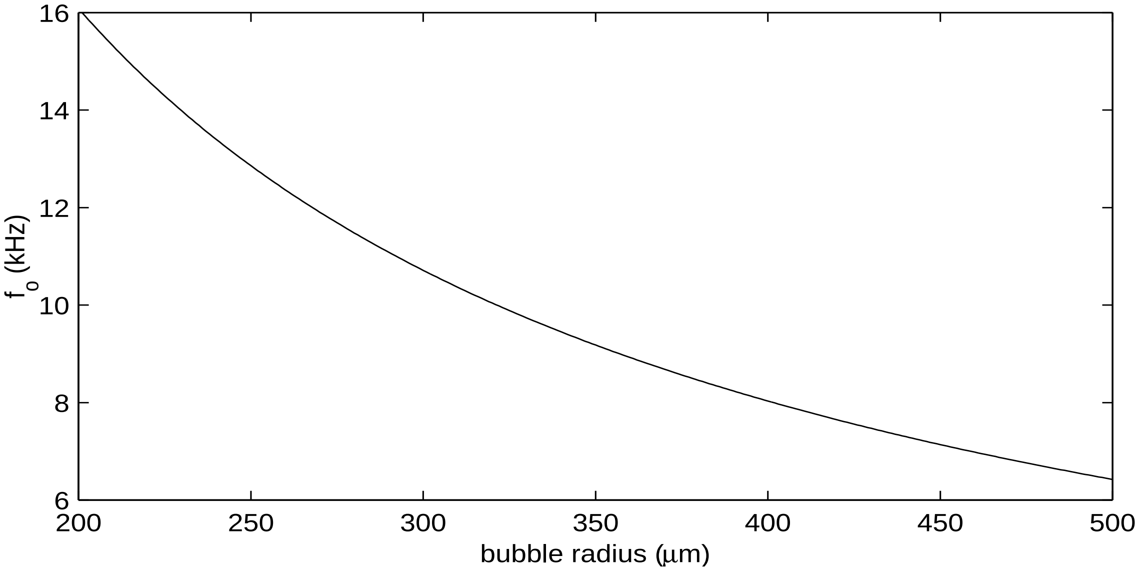

Figure 1.2: Resonance frequency for a bubble in water (cf. Eqn 1.5)

Unfortunately, most controlled single bubble experiments in the past have required some sort of stabilizing mechanism to hold the air bubble stationary in order to measure its oscillations. This has typically been either a physical object or radiation pressure from a standing wave in a resonant cell. In most cases, the fundamental resonance of the bubble is not directly measured, but is inferred from other experimental observations.

The first mechanism is an object, such as a plate or wire, physically holding the bubble in place. Strasberg [43] first calculated that the resonance frequency of a bubble in contact with a plane boundary would be 83% that of a bubble in an unbounded medium. Experiments by Howkins [19] confirmed this using a rod, but relied on shape oscillations to determine resonance. Blue [4] presented and experimentally verified a theory for resonance frequency of a bubble flattened near a plate, but used bubble translation as a resonance criterion.

A resonant acoustic cell is the other methodology commonly employed to hold the bubble. A cell in which standing waves are generated will trap a bubble because the primary Bjerknes force, dependent upon the bubble volume and pressure gradient, will offset the bubble's buoyancy force, effectively levitating it in place [37, 3, 50, 11]. The frequency of the cell must be lower than the resonance frequency of the bubble so that the bubble remains near a pressure antinode. If driven above its resonance frequency (i.e., the bubble is smaller than resonance size), the bubble will move to a pressure node and will experience minimal driving amplitude. Nevertheless, one must remain near the standing wave frequency in order to avoid translation or losing the bubble altogether while performing experiments. Thus, the acoustic levitation technique for studying driven bubble dynamics is limited to studying bubbles smaller or larger than their resonant size, but prohibits bubbles at or near resonant size. Measuring the frequency-dependent response of a bubble is impossible using such an arrangement, except at discrete harmonics of the levitater.

1.3 Xanthan Gel and Its Novel Uses for Suspending Bubbles

Use of a gel to study bubble dynamics has been done previously by Storm [41, 42], who studied nonlinear shape oscillations of bubbles 2–6 mm in radius at sub-kilohertz frequencies. The focus of the present work is the linear dynamics of bubbles 240–470 μm in radius in the frequency range 6–14 kHz using Xanthan gel to suspend the bubble.

The polymer Xanthan gum is an polysaccharide gum created from the fermentation processes of the bacterium *Xanthomonas campestris*. It is widely used as a food thickener, and can be made into a transparent gel, which will suspend small bubbles until dissolution. Introduced in 1995, Hwang et al. [20] performed sound speed measurements in a tube filled with bubbly gel of concentrations $\leq 1\%$. They demonstrated that bubbly gel undergoes the same decrease in sound speed as bubbly water.

The added viscoelasticity of Xanthan gel gives it the property of a pseudoplastic, or shear-thinning fluid, which is a subcategory of a larger class of fluids called non-Newtonian fluids. Unlike Newtonian fluids, such as water, non-Newtonian fluids display a dependence of viscosity on shear strain rate. The viscosity of Xanthan gel decreases as the shear strain rate increases. In addition, at a constant shear rate over a length of time, the viscosity will decrease slightly, making it weakly thixotropic [21].

The gel can be used in different capacities to hold bubbles. The amount of air dissolved in the water before gel fabrication determines the bubble number density that will eventually form in the gel upon mixing. If air-saturated water is used, a stable cloud of bubbles with a distribution of radii peaked near 100 μm will form relatively uniformly throughout the gel. This cloud can be well characterized because the bubbles do not move, and the fluid properties of density and sound speed are nearly the same as those of water.

If slightly degassed water is used while preparing the gel, it will form with no bubbles. In this case, a single bubble may be injected and held stationary in its spherically shaped equilibrium state, easily characterized by optical imaging techniques. But the question ultimately remains: is a bubble oscillating in Xanthan gel affected by the added viscoelasticity of the gel, or will it respond more like a bubble oscillating in water?

1.4 Summary of the Thesis

Thus motivated, we set out to measure the frequency-dependent linear radial response of a single bubble suspended by the Xanthan gel in an acoustic cell. The objective is twofold: (1) to assess the viability of this technique for studying the driven response of individual bubbles, and (2) to determine if bubbles suspended in a Xanthan gum solution behave in a manner similar to those in water. More specifically, does the non-Newtonian nature of the Xanthan material significantly impact the linear response of bubbles with sizes similar to those found in oceanic bubble clouds (240–500 μm radius)?

To measure the oscillations, laser light was scattered and collected from the bubble using a photomultiplier tube (PMT). Following the light-scattering measurement, an acoustic measurement was taken of the pressure field in the cell after the bubble was removed. This allowed us to negate the cell's frequency response, leaving only the bubble's response. Also, an independent measure of the bubble's equilibrium size was recorded with a CCD camera utilizing the gel's transparency.

Using optical sensing techniques allowed a less-invasive, yet more direct, measurement of the bubble motion as compared with acoustical techniques. Light-scattering from spheres is a well-developed method for sizing bubbles as will be described in the next Chapter. It does not rely on the measurement of acoustic emissions, nor does it disturb the pressure field experienced by the bubble.

Current theories for bubble motion assume an infinite fluid surrounding the bubble [9]. However, since only a small amount of fluid surrounding the bubble accounts for the majority of the effects observed, an experiment performed in a cell will give similar results as long as the bubble is located many bubble radii away from a cell wall.

The thesis will be structured as follows. Chapter 2 describes the theory to which the experimental data was eventually compared. It outlines Mie's theory of scattered light from dielectric spheres, which is used in predicting and interpreting what the PMT will detect. The bubble's response as a damped harmonic oscillator is also detailed. Finally, the main mechanisms associated with the damping of an oscillating air bubble submerged in a liquid are discussed.

In Chapter 3, the apparatus built to perform the experiments will be detailed. This includes the optical, acoustical, and data acquisition systems. Gel preparation and experimental methods, including bubble insertion and alignment, are discussed.

Chapter 4 presents experimental data and its processing and analysis — included here are bubble response versus frequency plots for different bubble sizes. Following this will be a discussion of the experimental error and uncertainty involved in the experiment.

Chapter 5 summarizes experimental results and their comparison with models. Also included are conclusions and recommendations for future work.

Chapter 2

Theoretical Modelling

In this chapter, the theoretical models used for comparison to data taken in this experiment will be discussed. For this experiment, two independent measurements were taken. The first is an optical measurement of the pulsating bubble using a photomultiplier tube (PMT) to sense scattered laser light. This served as a non-invasive, non-acoustical measurement of the dynamical response of the acoustically driven bubble. It is important to note that the optically measured frequency response of the bubble is going to be a convolution of the bubble's dynamic response and the frequency response of the acoustical cell in which the bubble is suspended. We assume for the time being that the photodetector's response is flat in amplitude and phase. (Although the cell is driven by a constant voltage amplitude, it does exhibit a weakly resonant frequency response.)

The second measurement is a measurement of the frequency-dependent acoustic pressure experienced by the bubble as measured with a miniature calibrated hydrophone. Since the cell's pressure response is measured *a priori* and used to equalize the cell's response from the total measured response, no modelling of the cell's frequency response is necessary.

So, two aspects of this experiment need to be modelled: 1) the scattering of light from a bubble undergoing linear radial pulsations, and 2) the bubble's dynamic response through it resonance frequency. We shall begin with a model for the expected response from the PMT.

2.1 Mie's Solution for the Scattering of Light from Dielectric Spheres

Hansen showed that Mie scattering of laser light could be used to size bubbles in water [16]. Holt and Crum built on this technique to follow the dynamic response of a bubble in water [18]. By calibrating a photodetector, such as a PMT or a photodiode, at scattering and collection angles that give a monotonic relationship between scattered intensity and bubble radius, a curve for scattered intensity as a function of bubble radius, I(R), can be obtained. This curve can then be inverted to get R(I), which can be used to transform a measured fluctuating light intensity to a radius versus time curve for the bubble. This experiment was designed to exploit this knowledge.

The complete set of equations describing scattering of light from spheres of arbitrary size can be derived from Maxwell's equations and are attributed to Gustav Mie [31], who first formulated the complete solution in 1908. Mie's solution asymptotes to Rayleigh scattering, or predominantly diffraction effects, for $ka \ll 1$, or to specular scattering, or mainly reflection and refraction effects, for $ka \gg 1$, where k is the wavenumber $2\pi/\lambda$ of light in the host medium, and a is the sphere's radius.

What follows are the resulting equations of scattered intensity as a function of scattering angle and bubble radius. The entire derivation will be omitted, but can be found in van de Hulst [44], whose notation will be followed. Mie's theory assumes a dielectric sphere of refractive index, m_1, is enveloped by a medium with refractive index, m_2, where a spatially-plane, electromagnetic wave of known polarization is incident upon the sphere. The relative refractive index, which is defined as

$$m = \frac{m_1}{m_2}, \tag{2.1}$$

is the index of the sphere with respect to the surrounding medium and can be complex to account for absorption of light. We will assume the Xanthan gel to have the same refractive index as water ($m_2 = 1.33$). The gas in the bubble we will assume to have a refractive index, $m_1 = 1.00$, so that $m = 0.75$. The scattering angle is measured from the forward direction, which is defined as the direction of propagation of the incident light. The components of the scattered intensity perpendicular and parallel to the plane of scattering at a large distance ($kr \gg 1$) from the sphere are given by

$$I_{\perp} = I_0 \frac{|S_1(\theta)|^2}{(kr)^2} \sin^2 \varphi \tag{2.2}$$

$$I_{\parallel} = I_0 \frac{|S_2(\theta)|^2}{(kr)^2} \cos^2 \varphi, \tag{2.3}$$

where I_0 is the incident intensity amplitude, and S_1 and S_2 are scattering-angle-dependent amplitude functions given in Appendix A. The scattering angle θ is the plane defined by the incident plane wave and the scattered spherical wave, and φ is the azimuthal angle.

For this experiment the polarization of laser was aligned with the horizontal, so the quantity of interest is Equation 2.3. Figure 2.1 shows the angular dependence for a bubble radius of 350 μm using a Helium-Neon (HeNe) laser with wavelength in air, $\lambda = 632.8$ nm, and for $m = 0.75$. There is minimal fine structure near $\theta = 80°$, and yet it is only one order of magnitude less than most of the scattering near the forward direction. It is also near the critical angle at $\theta = 82°$, where others have worked before [30, 24]. It appears to be an ideal angle at which to place a detector. This is confirmed when we plot the magnitude squared of the scattering amplitude versus bubble radius for $\theta = 80°$ in Figure 2.2, and we notice a gross monotonic trend between bubble radius and scattered intensity, but the fine structure introduces an uncertainty in radius. However, a "real" photodetector will have a finite aperture. So, if we integrate over a finite aperture of $80° \pm 12.7°$, the aperture of the experimental apparatus described in the next Chapter, we see in Figure 2.3 that the fine structure diminishes and a true monotonic relationship becomes apparent.

It is interesting to note that the collection angle of the optical detector is not the same in the gel as outside the cell. Differences in refractive index must be accounted for in the light propagation. Assuming a refractive index of 1.33 for the gel, 1.51 for the glass window, and 1.00 for the air outside the cell, we can calculate a total collection angle inside the gel in the cell from the known collection angle outside the cell, which is $\theta_{col,out} = 25.4°$. With the use of Snell's Law, we calculate that light from a solid angle of $\theta_{col,in} = 19.0°$, centered at 80°, in the gel becomes $\theta_{col,out}$ upon exiting the cell. This has the effect of lowering the magnitude of the plot in Figure 2.3, but does not change the R_0^2 dependence of the scattered intensity. This has no bearing on our results, because we are interested only in *relative*, not absolute, changes in scattered intensity.

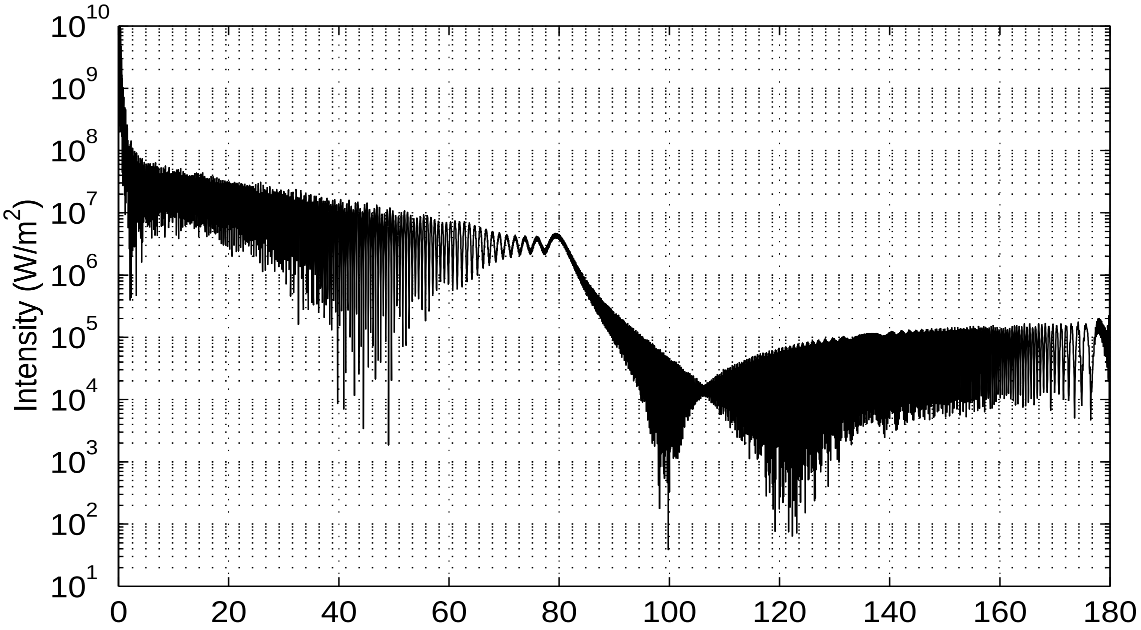

Figure 2.1: Scattered intensity for a 350 μm radius bubble; $\lambda = 632.8$ nm in air (HeNe laser); m = 0.75. The scattered intensity plotted is the component with polarization parallel to the scattering plane.

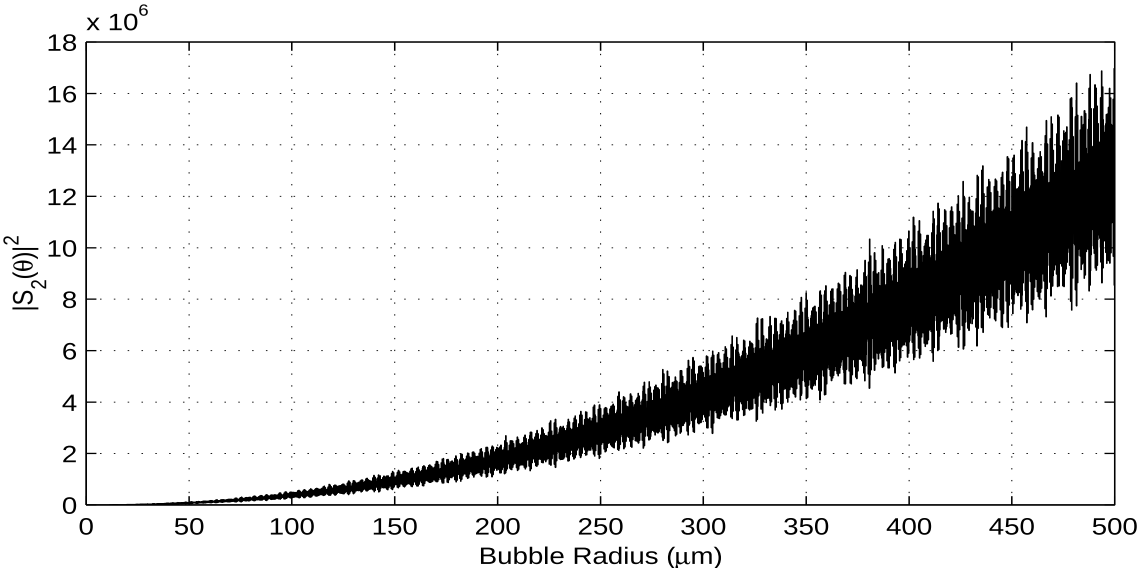

Figure 2.2: Magnitude squared of scattering amplitude vs radius for $\theta = 80°$; $\lambda = 632.8$ nm in air (HeNe laser); m = 0.75. $|S_2(\theta)|^2$ is proportional to the scattered intensity polarized parallel to the scattering plane.

2.2 Linearized Theory of Small Radial Displacements

The scattering angle used in this experiment, 80° ± 12.7° from forward, was chosen such that a monotonic relationship between scattered intensity and bubble radius existed. In this instance, scattered intensity is very nearly proportional to bubble radius squared [16, 18, 17]

$$I_{scat} \propto r^2, \tag{2.4}$$

so that we can write an equality of this form

$$I(R) = A + B(R_0)(R(t))^2, \tag{2.5}$$

where A is the DC component of background and scattered light and $B(R_0)$ is a proportionality constant dependent on equilibrium radius, R_0. The reason for this dependence is because the gel itself is not perfectly transparent and tends to diffuse more scattered light

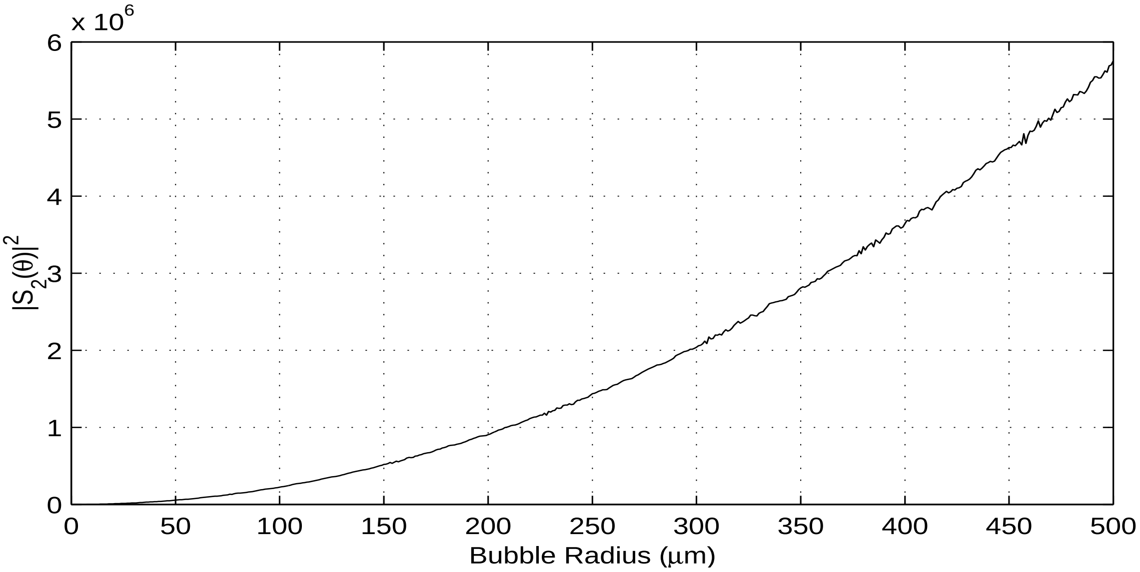

Figure 2.3: Magnitude squared of scattering amplitude vs radius integrated over a 25.4° solid angle centered at $\theta = 80°$; $\lambda = 632.8$ nm in air (HeNe laser); m = 0.75. $|S_2(\theta)|^2$ is proportional to the scattered intensity polarized parallel to the scattering plane.

with increasing bubble radius size. This extra diffused light gets scattered back into the collection angle of the detector.

We can write the instantaneous radius of a pulsating bubble as a sum of a constant equilibrium radius and a time-varying radial deviation from that equilibrium value

$$R(t) = R_0 + r(t), \tag{2.6}$$

where $r(t)$ is taken to be much smaller than R_0. Upon substitution of this expression into the intensity expression above, and suppressing explicit time dependence, we get

$$I(R) = A + B(R_0)(R_0^2 + 2R_0 r + (r)^2), \tag{2.7}$$

which, upon factoring out R_0^2, becomes

$$I(R) = A + B(R_0)R_0^2 \left(1 + \frac{2r}{R_0} + \left(\frac{r}{R_0}\right)^2\right). \tag{2.8}$$

We shall then define $K \equiv B(R_0)R_0^2$ as a calibration constant which we shall neglect because a normalized response will be used. Because we assume small amplitude oscillations, we can neglect the quadratic term. To first order, then we have

$$I(R) = A + K\left(1 + \frac{2r}{R_0}\right), \tag{2.9}$$

which has two DC components and an oscillatory component linear in radius. So, we should expect the scattered intensity variations to be proportional to r, the instantaneous radial excursions of the bubble from equilibrium.

2.3 Damped Linear Oscillator Model

A bubble oscillating in a liquid can be modelled as a damped linear oscillator. In this section, an overview of damped linear oscillators will be given with the relevant equations we used for analysis of data. Then the theory of a bubble oscillating in water will follow, demonstrating the parallels to a damped linear oscillator, and thus justifying the use of the model.

Theory on damped linear oscillators can be found in a variety of texts, but French's development will be followed here [14]. A mass coupled to a spring and dashpot and forced into oscillatory motion can be described by the differential equation

$$m\ddot{x} + b\dot{x} + kx = F_0 e^{-i\omega t}, \tag{2.10}$$

where x is the spatial displacement of the mass, m, b is the damping coefficient, k is the spring constant or stiffness, F_0 is the forcing amplitude, ω is the excitation frequency, and a dot denotes differentiation with respect to time.

This equation can be rewritten in the form [12]

$$\ddot{x} + 2\zeta\omega_n\dot{x} + \omega_n^2 x = \frac{F_0}{m} e^{-i\omega t}, \tag{2.11}$$

where

$$\omega_n = \sqrt{\frac{k}{m}}, \tag{2.12}$$

$$\zeta = \frac{b}{2\sqrt{km}}, \tag{2.13}$$

define the natural frequency and the dimensionless damping ratio, respectively. The Quality factor, a measure of the amplitude response at the resonance frequency of the system, can be defined in terms of the damping ratio as

$$Q = \frac{1}{2\zeta\sqrt{1-\zeta^2}}. \tag{2.14}$$

However, for light damping ($\zeta^2 \ll 1$), Q becomes

$$Q \simeq \frac{1}{2\zeta}. \tag{2.15}$$

It will be shown in Appendix B that the smallest value of Q measured for this thesis is 13.2. Computing the dimensionless damping ratio using $Q = 13.2$, and Equations 2.14 and 2.15, yields $\zeta_{full} = 0.001$ and $\zeta_{approx} = 0.038$, respectively. In both cases $\zeta^2 \ll 1$, so the approximation of light damping is valid. We can also define the resonance frequency as

$$\omega_0 = \omega_n\sqrt{1-2\zeta^2}, \tag{2.16}$$

which is a property of the measurement system. For the above value of the damping ratio, the resonance frequency will be 0.3% lower than the natural frequency, which it will be shown in Chapter 4, to be smaller than any incurred experimental error. When we measure the frequency response of the bubble, we will be measuring the resonance frequency and not the natural frequency, although they will be almost equivalent. As such, we will use the term resonance frequency for the remainder of the thesis for data comparison purposes.

So, rewriting Equation 2.11 using Equation 2.15 we get:

$$\ddot{x} + \frac{\omega_n}{Q}\dot{x} + \omega_n^2 x = \frac{F_0}{m}e^{-i\omega t}. \tag{2.17}$$

where we now have as a definition of the Quality factor,

$$Q = \frac{m\omega_0}{b}. \tag{2.18}$$

The greater the damping of a given system, the smaller the Quality factor becomes. This is important to keep in mind as it will be a parameter, along with the resonance frequency, that will be used to characterize the experimental data later.

Choosing a displacement of the form

$$x = x_0 e^{-i(\omega t - \delta)}, \tag{2.19}$$

results in an equation for the amplitude, x_0, and phase, δ

$$\begin{aligned} x_0(\omega) &= \frac{F_0/m}{\sqrt{\left(\omega_0^2 - \omega^2\right)^2 + \left(\frac{\omega\omega_0}{Q}\right)^2}}, && (2.20) \\ \delta &= \arctan\left(\frac{\omega\omega_0}{Q(\omega_0^2 - \omega^2)}\right). && (2.21) \end{aligned}$$

However, we will be working with an amplitude response normalized to the peak at resonance, so finally we have

$$A(\omega) \equiv \frac{x_0(\omega)}{x_o(\omega = \omega_0)} = \frac{\omega_0^2/Q}{\sqrt{\left(\omega_0^2 - \omega^2\right)^2 + \left(\frac{\omega\omega_0}{Q}\right)^2}}. \tag{2.22}$$

Differentiating Equation 2.21 with respect to ω, and evaluating at ω_0, gives a more practical expression for Q

$$Q = \frac{\omega_0}{2}\left(\frac{d\delta}{d\omega}\right)_{\omega=\omega_0}, \tag{2.23}$$

that will be useful in conjunction with the phase plots computed from the raw PMT data to find a starting value for Q when we fit the model of this section to the equalized PMT data of a bubble's frequency response.

We now demonstrate the parallels of an air bubble oscillating in water to the above derivation. But first, we will once again assume small amplitude radial oscillations of a bubble about its equilibrium radius, so we can write

$$R(t) = R_0 + r(t) \text{ where } r \ll R_0. \tag{2.24}$$

The bubbles of interest in this work are acoustically compact ($R \ll \lambda$, where λ is the acoustic wavelength), so we can use a lumped element approach and model the bubble as a mechanical system with an effective mass, m_{eff}, an effective damping, b, and an effective stiffness, k_{eff}. The force balance for this bubble is

$$m_{eff}\ddot{R} = -f(t) - b\dot{R} - k_{eff}R, \tag{2.25}$$

where $f(t)$ is the total force on the bubble and includes contributions from both hydrostatic and dynamic forcing:

$$f(t) = f_s + F_0 e^{-i\omega t}, \tag{2.26}$$

where we assume the dynamic portion of the force to be time-harmonic. Combining Equations 2.24–2.26 results in

$$m_{eff}\ddot{r} + b\dot{r} + k_{eff}r = -F_0 e^{-i\omega t} - (f_s + k_{eff}R_0). \tag{2.27}$$

If the static case is considered ($r = 0$ and $F_0 = 0$), the resulting force balance becomes

$$f_s = -k_{eff}R_0, \tag{2.28}$$

and Equation 2.27 becomes

$$m_{eff}\ddot{r} + b\dot{r} + k_{eff}r = -F_0 e^{-i\omega t}. \tag{2.29}$$

This can be rewritten in a form analogous to Equation 2.17:

$$\ddot{r} + \frac{\omega_0}{Q}\dot{r} + \omega_0^2 r = -F_0 e^{-i\omega t}, \tag{2.30}$$

where

$$\omega_0^2 = \frac{k_{eff}}{m_{eff}}, \tag{2.31}$$

$$Q = \frac{m_{eff}\omega_0}{b}. \tag{2.32}$$

So now we have an equation that describes the motion of the bubble wall that is completely analogous to the harmonic oscillator equation discussed earlier. Now we shall develop expressions for the effective mass and stiffness of the bubble.

Consider a bubble of equilibrium radius, R_0, exposed to a hydrostatic pressure, P_0. Ignoring gas diffusion and surface tension, the equilibrium force balance across the bubble wall is

$$f_s = -k_{eff} R_0. \tag{2.33}$$

Now let us perturb the external force so that the new force outside the bubble wall is

$$f' = f_s + \Delta f = -k_{eff}(R_0 + \Delta R). \tag{2.34}$$

This perturbation is caused by the pressure change imposed by acoustic forcing

$$\Delta f = (4\pi R_0^2)\Delta p, \tag{2.35}$$

where p is the acoustic pressure. Thus

$$f' = f_s + 4\pi R_0^2 \Delta p = -k_{eff}(R_0 + \Delta R), \tag{2.36}$$

combining with Equation 2.33:

$$4\pi R_0^2 \Delta p = -k_{eff} \Delta R. \tag{2.37}$$

Now, how does p relate to P_0, R_0, and ΔR? Assuming small amplitude oscillations, the equation of state for the gas in the bubble can be written as

$$\Delta p = c_g^2 \Delta \rho_g = c_g^2 \Delta \left(\frac{m_g}{V}\right) = c_g^2 \frac{-m_g \Delta V}{V^2} = -\rho_g c_g^2 \frac{\Delta V}{V}, \tag{2.38}$$

where m_g, ρ_g, and c_g are the mass, density, and sound speed of the gas, and V is the volume of the bubble. It can be shown that for a sphere

$$\frac{\Delta V}{V} = \frac{3r}{R_0}, \tag{2.39}$$

and therefore,

$$p = -\rho_g c_g^2 \left(\frac{3r}{R_0}\right). \tag{2.40}$$

For an ideal gas undergoing an adiabatic process

$$\rho_g c_g^2 = \gamma P_0, \tag{2.41}$$

where γ is the ratio of specific heats. Combining Equations 2.37, 2.40, and 2.41, and solving for k_{eff} yields

$$k_{eff} = 12\pi R_0 \gamma P_0. \tag{2.42}$$

The effective mass loading on bubble oscillations can be determined directly by consideration of its acoustic radiation impedance. For an acoustically compact pulsating sphere, the radiation impedance has two terms, a real, resistive term that determines radiation damping and an imaginary, reactive term that determines radiation mass loading

$$Z_r = R_r + iX_r = \rho_l c_l S (kR_0)^2 + i\rho_l c_l S k R_0, \tag{2.43}$$

where $S = 4\pi R_0^2$, c_l is the liquid sound speed, and $k = \omega / c_l$. Now recall that our bubble can be modelled as a lumped element. The impedance of a lumped system has the following form

$$Z_{lumped} = \text{Resistance} + i\left(\omega m_{eff} - \frac{k_{eff}}{\omega}\right). \tag{2.44}$$

Comparison of Equations 2.43 and 2.44 shows that the effective radiation mass is:

$$\omega m_{eff} = \rho_l (4\pi R_0^2) \omega R_0. \tag{2.45}$$

Note that the radiation reactance is purely inertial here. Finally, we have:

$$m_{eff} = (4\pi R_0^3)\rho_l = 3V\rho_l. \tag{2.46}$$

It is interesting to note that the radiation mass loading is a mass of the surrounding liquid equal to three times the volume displaced by the bubble.

So, in summary, we have a simple harmonic oscillator equation for the linear, adiabatic, radial pulsations of a bubble under harmonic acoustic forcing:

$$\ddot{r} + \frac{\omega_0}{Q}\dot{r} + \omega_0^2 r = \frac{f_0}{m_{eff}} e^{-i\omega t}, \tag{2.47}$$

where

$$\omega_0^2 = \frac{k_{eff}}{m_{eff}} = \frac{3\gamma P_0}{\rho_l R_0^2}, \tag{2.48}$$

$$Q = \frac{m_{eff}\omega_0}{b} = \frac{1}{b} 4\pi R_0^2 \sqrt{3\gamma P_0 \rho_l}. \tag{2.49}$$

The solution to this equation is given by Equations 2.19–2.23. Note that the expression for the resonance frequency, ω_0, is identical to the Minnaert frequency given in Equation 1.5.

The equivalent mass and stiffness of a bubble have been derived above to show the motivation for using a damped linear oscillator. However, the damping term is more complicated and will be described presently.

2.4 Damping

Near a bubble's resonance frequency, damping of the motion of the bubble wall is at a maximum, and it consists of contributions from three primary mechanisms: thermal, radiation, and viscous losses. Losses from thermal conduction of heat from the gas in the bubble to the surrounding fluid dominates at all but the smallest bubbles and highest frequencies. Reradiation of incident acoustic energy through bubble pulsation dominates at frequencies above the bubble's resonance. Viscous dissipation becomes important at small bubble sizes on the order of 1 μm radius.

Prosperetti derived expressions for each of the three damping contributions for linear bubble oscillations in an unbounded liquid [35], which in contrast to Devin [10] are valid off-resonance as well as at resonance. We now follow Prosperetti's notation, so a redefinition of the damping coefficient becomes necessary. Some texts [10, 25] use δ to denote the *dimensionless* damping coefficient at resonance, but for uniformity in a comparison of our resulting data to a model, we shall follow the notation as it was presented. As such, our resulting data will be put into a form equivalent to the theory of Prosperetti. Prosperetti defines the *dimensional* total damping coefficient as β. The equivalence to the previous section's notation is written as $\beta = b/2m_{eff}$. With the use of Equation 2.18 we can rewrite this in terms of the two parameters, ω_0 and Q, as

$$\beta = \frac{\omega_0}{2Q}. \tag{2.50}$$

This equation gives the form of the damping coefficient we will use for data analysis.

As mentioned above, the three contributions to β are thermal, acoustic, and viscous losses, where

$$\beta = \beta_{th} + \beta_{ac} + \beta_{vis}, \tag{2.51}$$

and can be written as

$$\beta_{th} = \frac{2\mu_{th}}{\rho_l R_0^2} \tag{2.52}$$

$$\beta_{ac} = \frac{\frac{1}{2}\omega\left(\frac{\omega R_0}{c_l}\right)}{\left[1 + \left(\frac{\omega R_0}{c_l}\right)^2\right]} \tag{2.53}$$

$$\beta_{vis} = \frac{2\mu}{\rho_l R_0^2}, \tag{2.54}$$

where μ the viscosity of the liquid, R_0 is the equilibrium bubble radius, ω is the acoustical driving frequency, c_l the liquid sound speed, and μ_{th} is an effective viscosity term due to thermal damping. The "thermal" viscosity term is derived from the linearization of the conservation equations of mass and momentum in the gas in the bubble interior, and from the conservation of energy in the gas and surrounding liquid.

The expression for μ_{th} is given as

$$\mu_{th} = \frac{1}{4}\omega\rho_g R_0^2 Im\phi, \tag{2.55}$$

where ρ_g is the density of the gas, and ϕ is given as

$$\phi = \frac{kf(\Gamma_2 - \Gamma_1) + \lambda_2\Gamma_2 - \lambda_1\Gamma_1}{kf(\lambda_2\Gamma_1 - \lambda_1\Gamma_2) - \lambda_1\lambda_2(\Gamma_2 - \Gamma_1)}, \tag{2.56}$$

where

$$\begin{aligned}
\Gamma_{1,2} &= i + G_1 \pm \left[(i - G_1)^2 + 4iG_1/\gamma\right]^{\frac{1}{2}} && (2.57)\\
\lambda_i &= \beta_i \coth \beta_i - 1, \quad i = 1, 2 && (2.58)\\
\beta_{1,2} &= \left(\frac{1}{2}\gamma G_2 \left\{ i - G_1 \pm \left[(i - G_1)^2 + 4iG_1/\gamma\right]^{\frac{1}{2}} \right\}\right)^{\frac{1}{2}} && (2.59)\\
f &= 1 + (1 + i)\left(\frac{1}{2}G_3\right)^{\frac{1}{2}} && (2.60)\\
k &= \frac{k_l}{k_g}. && (2.61)
\end{aligned}$$

The subscripts 1 and 2 in the expressions for $\Gamma_{1,2}$ and $\beta_{1,2}$ denote the use of the plus and minus, respectively, where a ± symbol appears in those expressions. The dimensionless quantities are given by

$$\begin{aligned}
G_1 &= \frac{D_g \omega}{c_g^2} && (2.62)\\
G_2 &= \frac{\omega R_0^2}{D_g} && (2.63)\\
G_3 &= \frac{\omega R_0^2}{D_l}. && (2.64)
\end{aligned}$$

The gas sound speed in the dimensionless parameter G_1 is given by

$$c_g^2 = \frac{\gamma R_g T_\infty}{M} \qquad (2.65)$$

All the thermodynamic properties used in this development are given in Table 2.1. The significance of the dimensionless parameters are as follows: G_1 is the square of the ratio of the depth of significant thermal conduction below the bubble's surface to the wavelength of sound. G_2 and G_3 are squares of the ratio of bubble radius to thermal penetration depth in the gas and liquid, respectively.

A plot of the contribution of each damping mechanism to bubbles of size 200–500 μm radius *in water* is shown in Figure 2.4. The damping coefficient was evaluated at the corresponding resonance frequency for each bubble radius. For our sizes of interest, thermal damping is clearly the dominant mechanism of dissipation.

Table 2.1: **Thermal Parameters**

Symbol	Definition	Value Used	Units
μ	Viscosity of Water	0.001	$\text{Pa} \cdot \text{s}$
D_g	Thermal Diffusivity of Air $= \frac{k_g}{\rho_g c_{v,g}}$	1.992E-5	$\frac{\text{m}^2}{\text{s}}$
D_l	Thermal Diffusivity of Water $= \frac{k_l}{\rho_l c_{v,l}}$	1.448E-7	$\frac{\text{m}^2}{\text{s}}$
$c_{v,g}$	Heat Capacity at Constant Volume of Air	1007[1]	$\frac{\text{J}}{\text{kg}\cdot\text{K}}$
$c_{v,l}$	Heat Capacity at Constant Volume of Water	4185.2[1]	$\frac{\text{J}}{\text{kg}\cdot\text{K}}$
k_g	Thermal Conductivity of Air	0.0259[2]	$\frac{\text{W}}{\text{m}\cdot\text{K}}$
k_l	Thermal Conductivity of Water	0.6043[1]	$\frac{\text{W}}{\text{m}\cdot\text{K}}$
γ	Ratio of Specific Heats of Air $= \frac{c_{p,g}}{c_{v,g}}$	1.4	—
R_g	Universal Gas Constant	8314.47	$\frac{\text{g}\cdot\text{m}^2}{\text{s}^2\cdot\text{K}\cdot\text{mol}}$
M	Molecular Weight of Air	28.94	$\frac{\text{g}}{\text{mol}}$
T_∞	Water Temperature	296.65	K

As previously mentioned, Xanthan gel is a non-Newtonian fluid, so we should expect a decrease in viscosity for increasing shear strain rate in the gel. Measurement of the gel viscosity was made by a concentric cylinder viscometer, but was inconclusive, although the viscosity was inversely proportional to shear strain rate as expected. The exact viscosity of Xanthan gel requires measurement by a rheometer because the gel possesses a viscosity *and* an elasticity. Even had such an instrument been available to us, conventional rheometer measurements are generally made under linear velocity gradient conditions, not with the type of flow associated with a bubble oscillating radially. Estimation of the shear strain rate around a radially oscillating bubble is difficult at best. However, we can determine an "effective" viscosity experienced by the oscillating bubble by comparison of the measured data to theory of a bubble oscillating in a viscous *Newtonian* fluid.

---

[1] CRC Handbook of Chemistry and Physics, 3rd electronic Ed. (www.hbcpnetbase.com)

[2] SFPE Handbook of Fire Protection Engineering, 2nd Ed., Table B-2

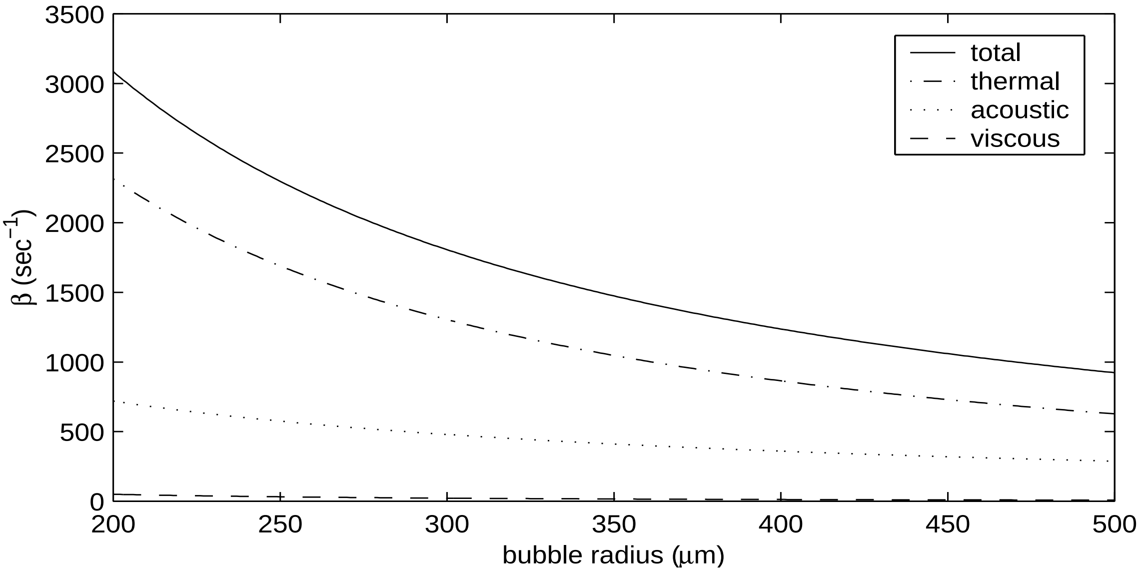

Figure 2.4: Thermal, acoustic, and viscous contributions to the total damping for a bubble in water. At each value for the bubble radius, the damping coefficient was evaluated at that bubble's resonance frequency.

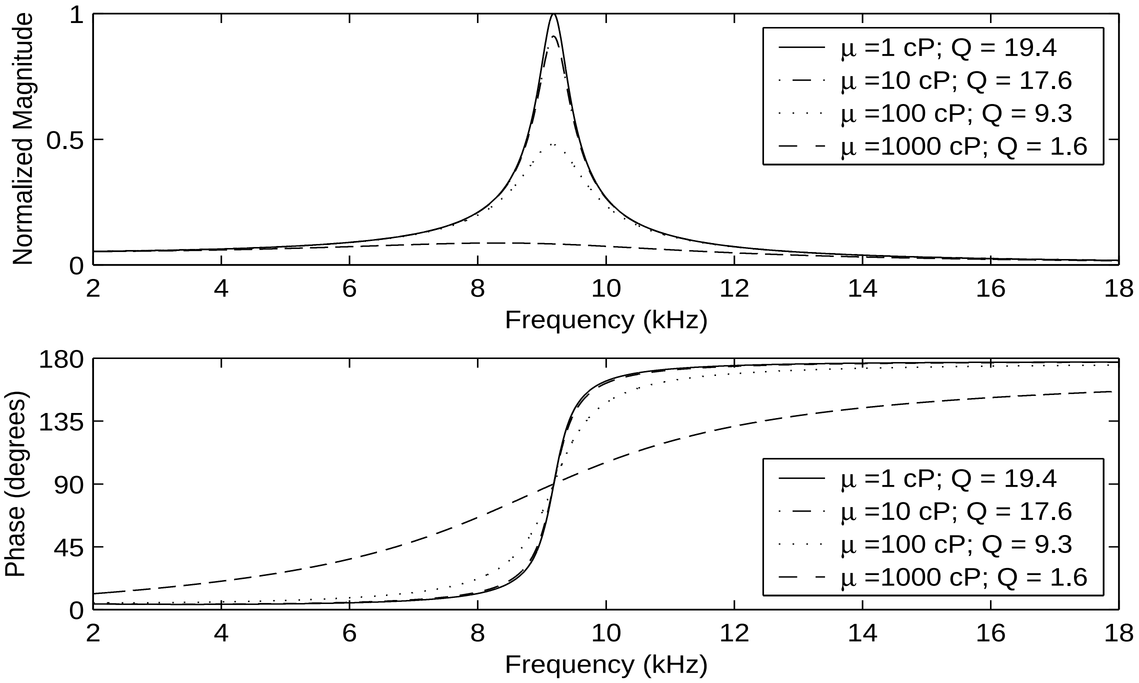

Figure 2.5: Calculated magnitude and phase of the frequency response of a 350-μm radius bubble with varying values for viscosity.

Figure 2.5 shows a simulation using Prosperetti's damping model of how different values of viscosity affect the Q of the response of a bubble in a viscous Newtonian fluid. To orient the reader, water and glycerin at 23°C have viscosities of 1 cP and 1000 cP, respectively. For a change in viscosity of three orders of magnitude, the resonant peak is completely flattened to a low Q response. As expected, for large values of Q, or light damping, the resonance frequency is approximately given by that of an undamped oscillator. It is apparent, then, that comparison of the measured response of a bubble *in gel* to the predicted response in a viscous Newtonian fluid, such as water, will determine how closely the Xanthan gel appears to the bubble to act like that fluid.

So, now we can predict the response of the PMT to scattered light, and the bubble's small-amplitude response to acoustically-forced oscillations in a viscous Newtonian medium. We expect that the time-varying PMT output will be proportional to the instantaneous bubble radius for the small oscillations induced by the acoustic pressures generated. We also expect the bubble to act as a damped linear oscillator with a measurable resonance frequency and Quality factor. A total damping coefficient can furthermore be deduced from the two measured parameters. For a given bubble size and frequency, we can separate the total damping coefficient into three loss mechanisms to estimate the importance of each for a bubble in water. Comparison to a water bubble is made to confirm or deny the hypothesis that a bubble oscillating in the Xanthan gel mimics a bubble oscillating in water at the sizes and frequencies measured. Next, we shall describe the experimental apparatus built and the methods developed to obtain data for such a comparison.

Chapter 3

Experimental Apparatus

3.1 Objectives of the Experiment

The objective of the experiment was to determine the frequency-dependent, acoustically driven, linear response of a bubble suspended in Xanthan gum polymer gel by collecting scattered laser light from the radially oscillating bubble. As such, a laser light scattering system was developed along with an optical imaging apparatus to measure the equilibrium radius, and an acoustic test cell to hold and acoustically excite the bubble in the gel.

With this information, we sought to determine the bubble response through the resonance region, isolating both the resonance frequency and the damping coefficient (the latter derived from a measurement of the Q of the resonance peak). Comparison was made between the measured response and theoretical predictions to ascertain the utility of this method for measuring bubble dynamics and the suitability of using Xanthan gum as a holding medium.

3.2 Motivations for the Design

As described in the last chapter, Mie scattering theory incorporates both the diffraction effects of Rayleigh scattering and the reflection and refraction effects of specular scattering. If θ represents the polar, or “scattering”, angle and ϕ the azimuthal angle of a sphere, there is an azimuthal symmetry associated with the ϕ direction for plane light waves incident in the θ plane. However, there is a complex pattern associated with the plane of the polar angle. So one must choose from within the complex structure inherent in that plane, a position at which to collect data that will maximize signal and stability while minimizing strong angular sensitivities. For these experiments, the polarization of the laser was aligned with the horizontal so that the optical scattering measurement consisted of the component of the scattered intensity parallel to the scattering plane.

In this experiment the direction in which the light travels is defined as $\theta = 0^\circ$, or forward scattering. For the light wavelength used for this experiment (HeNe, $\lambda = 632.8$ nm in air), there is a location around $\theta = 80^\circ$ where the intensity is an order of magnitude lower than forward scattering, but the fine structure is minimal allowing small changes in angle to have little effect on the scattered intensity. This was the angle at which we chose to work.

Because the gel suspends the bubble and keeps it from rising, no acoustic standing wave is required for spatial bubble stabilization. A curved cell, such as a sphere or cylinder, would be ideal to collect the spherical waves radiating from an effective point source. However, the cell would contain strong resonances near the center where a bubble would have to be placed to avoid light collection distortion. Moreover, such strict positioning constraints would hamper accurate light collection. In order to compare the measured bubble response to theory, we must measure the equilibrium size of the bubble at rest, *a priori*. This was done using a stereomicroscope coupled to a CCD array. Photographic imaging demands at least one flat face in the cell to minimize optical aberration of the image. As a result of all these considerations, we decided to employ a “modified” cube designed to minimize acoustic standing waves while offering optimal optical access for both imaging and scattering measurements. This cell is described below.

3.3 General Functional Description of the Experimental System

In general, the entire system was designed to work as follows. A bubble is injected by hand pipette into the gel in the cell. Using white light illumination behind the bubble, an optical image is taken using a stereomicroscope to focus the image to a CCD camera. The white light is then turned off. The bubble is then insonified by a piezoelectric (PZT) transducer attached to the cell floor and driven by either a function generator or frequency-swept chirp from a digital signal analyzer (DSA). Laser light is scattered from its surface and focused by the same stereomicroscope onto the photocathode of a photomultiplier tube (PMT). The light is transduced to a current at the anode of the PMT, and is measured as a voltage across a 100 kΩ resistor in the voltage divider of the PMT base. The output voltage is fed through a 0.5–150 kHz filter to the DSA where conversion to the complex frequency domain is accomplished by computation of the Fast Fourier Transform of the data. What results is the frequency response of the bubble when driven by a frequency-dependent acoustic pressure field.

As the bubble dissolves, the experiment is repeated until the signal-to-noise (S/N) level is too low, or the bubble has dissolved. If the bubble has not dissolved at this time, it is removed and replaced by a miniature hydrophone at the same spatial location. The method of insonification used to excite the bubble is reprised to measure the frequency-dependent pressure field of the cell, which is filtered, processed, and stored identically to the optical scattering measurement. This is then used to “equalize” the measured light scattering spectra, thus isolating the frequency response of the bubble itself.

3.4 The Acoustic Test Cell and Electronics

The acoustic test cell is a modified cube with an open top and one non-parallel wall for light collection at $\theta = 80°$, as shown in Figure 3.1. The base is a 11.43(L) x 11.43(W) x 5.08 cm(H) piece of delrin with a 2.4" diameter hole cut through the center for the hollow cylindrical piezoelectric (PZT) transducer, which is held in place by two Buna-N O-rings between the outer wall of the transducer and the inner wall of the hole in the delrin. A frosted piece of glass was sealed flush with the containing volume floor of the cell with room temperature vulcanized rubber (RTV). The PZT transducer itself was then sealed to the glass with the same substance; the intention was that the glass could be used for diffusive bottom illumination if required, which it eventually was not.

The containing volume of the cell consists of 4 glass windows (3.3 mm thick) held in place by four alloy 6013 aluminum corner columns. The windows are float glass with index of refraction, $m_{window} = 1.51$, that are coated with an anti-reflection coating which allows 96-99% transmittance of light within the range of wavelengths 400–700 nm. Two windows stand parallel to one another, while the opposing pair are askew by 10° from one another. Care was taken to assemble the windows in the precision-machined grooves to insure correct and accurate angles (±2° vertically) that can be used for alignment later. Alloy 6013 aluminum was chosen for the corner posts because of its good machinability and its high corrosion resistance from the 3.5% salt content in the gel. RTV was also used to seal the glass to the groove in the delrin and to the grooves in the aluminum corner posts.

An HP 33120A function generator and a HP 3562A DSA both acted as waveform sources for the PZT. The function generator had a frequency range of 15 MHz, and an amplitude range up to 20 volts peak-to-peak (Vpkpk). However, it was used only for diagnostic purposes in setting up experiments. The data for this thesis was all taken using a sinusoidal frequency-swept chirp sourced by the DSA. The chirp was amplified through a Krohn-Hite 7602M wideband (DC to 1 MHz) power amplifier to 15 Vpkpk and terminated at the PZT,

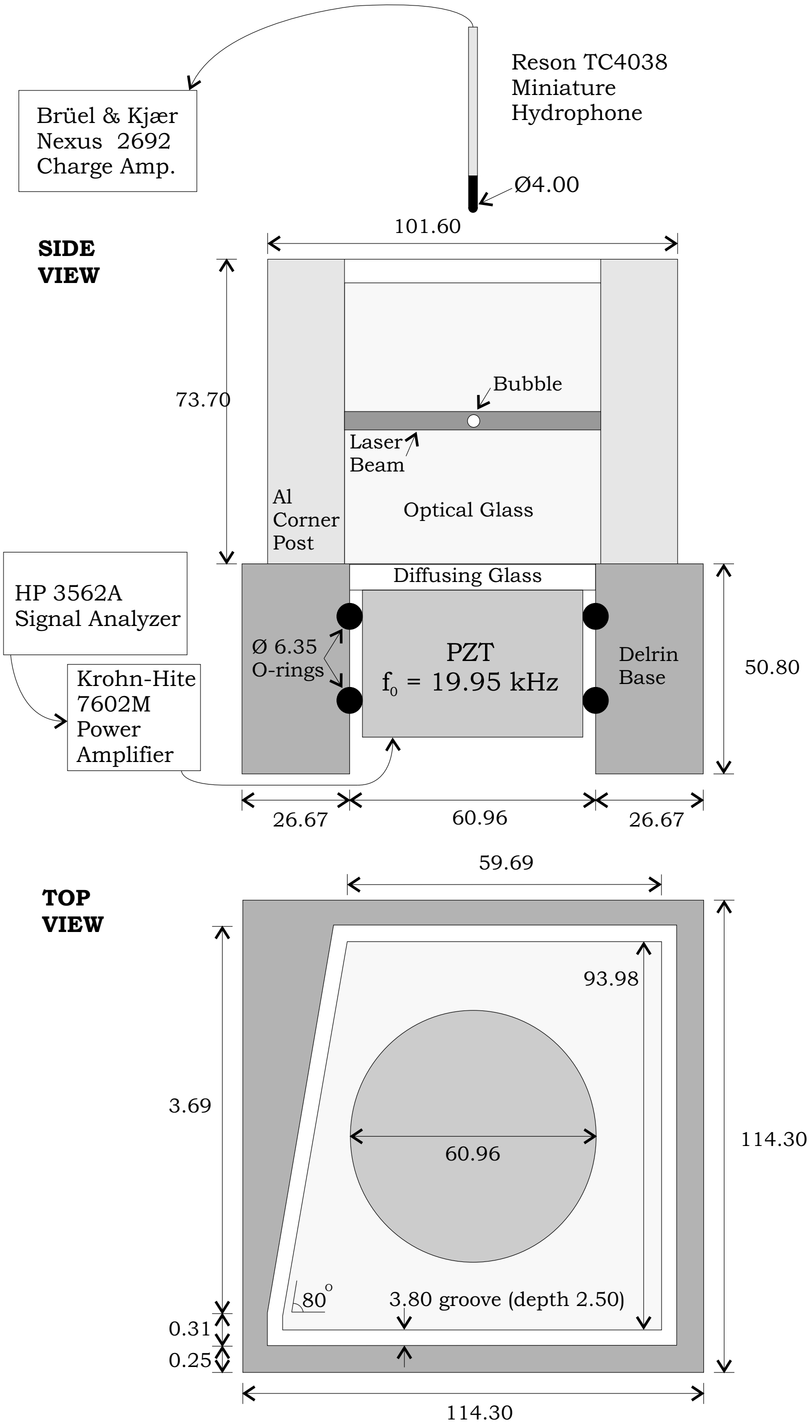

Figure 3.1: Side and top views of the acoustic test cell and related electronics. All dimensions are in millimeters. Laser beam and bubble dimensions are exaggerated in scale.

which has $f_0 = 19.95$ kHz.

To determine the frequency-dependent pressure field in the cell, a Reson TC4038 miniature hydrophone replaced the bubble at the same spatial position in the cell. The 4-mm-diameter cylindrical hydrophone has a sensitivity of -228 ± 2 dB re 1 V/μPa over the range 5–800 kHz. Amplification of the hydrophone is carried out by a Brüel and Kjær 2962 charge preamplifier. The range of amplification varied with the S/N level of the experiment, but was of the order of 1 mV/Pa with a hydrophone charge sensitivity of 2.249 fC/Pa. After amplification, the hydrophone signal was terminated into 1 MΩ at the second input to the DSA for processing as described in Section 3.7.2.

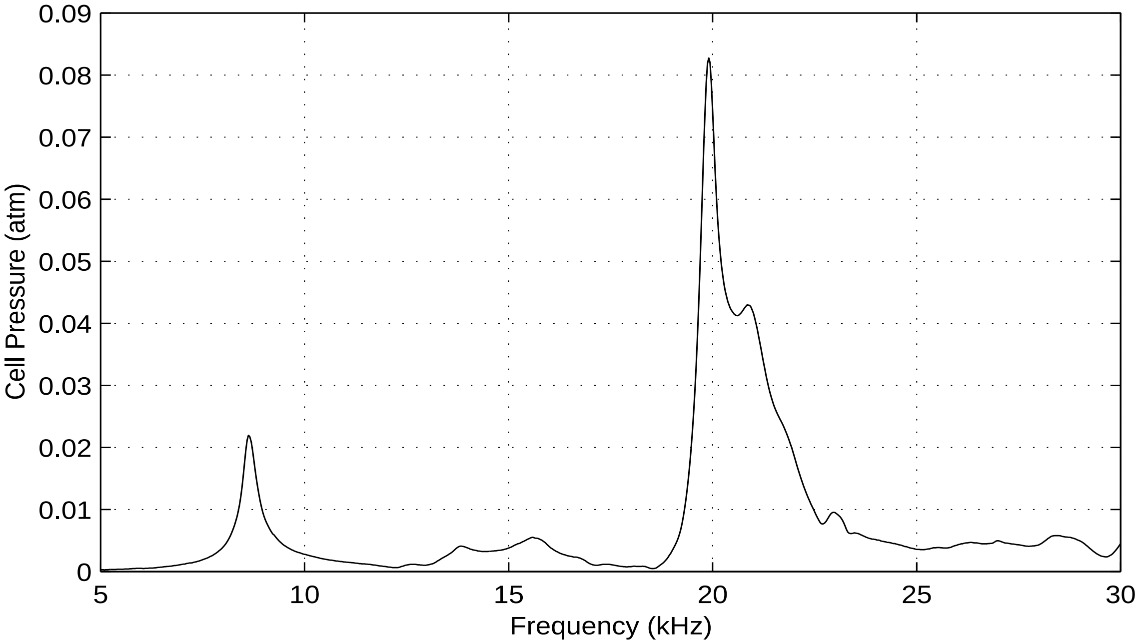

Figure 3.2: Typical acoustic pressure amplitude frequency response of acoustic cell taken with Reson TC4038 miniature hydrophone.

Although, the cell is a low Q resonator, it did nonetheless possess resonances. In the small volume that the bubble occupied, there were frequency peaks attributable to cell resonances as shown in Figure 3.2. The gel has a sound speed, c_gel, measured at 1 MHz of

1539 m/s. The two parallel walls of the cell are 3.7 inches (93.98 mm) apart. Assuming zero particle velocity (sound hard) boundary conditions at the walls, a half wavelength standing wave develops between the walls with frequency

$$f = \frac{c_g}{\lambda} = \frac{1539\ \mathrm{m/s}}{2 \times (0.09398\,\mathrm{m})} = 8188\ \mathrm{Hz}, \tag{3.1}$$

which is comparable to the measured resonance at 8630 Hz since the sound speed is unknown at the frequencies used for the measurement. Moreover, the characteristic impedance, ρc, of glass ($\sim 12.0 \times 10^6$ Pa · s/m) is only 7–8 times greater than the gel ($\sim 1.6 \times 10^6$ Pa · s/m) [22]. This makes the sound hard boundary condition at the windows less than ideal.

The strong geometric resonance at 8630 Hz has a measured Q in the range 26–29. The PZT resonates at 19.95 kHz and contributes the strongest resonance to the cell with a measured Q of 60 when the cell is full of gel. There are also geometric resonances near 13.9 and 15.5 kHz, but they are of much lower Q. Nevertheless, when a measurements was taken away from resonances to avoid coupling the response of the bubble to a higher Q response of the cell, the bubble's frequency response was more easily extracted from the raw PMT data. As will be shown in Chapter 4, the data resulting from measurements near cell-related resonances proved difficult from which to extract the bubble's response.

3.5 Optics

3.5.1 Mie Scattering Apparatus

The optical scattering measurement is made with an apparatus that includes these components: a laser, the oblique cell, the stereomicroscope, and the PMT and associated electronics as shown in Figure 3.3. The light is sourced by a 10 milliwatt Helium-Neon (HeNe) JDS Uniphase 1135P laser at wavelength $\lambda = 632.8$ nm. It has a Gaussian-shaped beam of diameter 0.68 mm at the 1/e power points, and is polarized in the TEM_{00} mode. Before performing an experiment, the laser must be powered on for 15 minutes to allow it to reach 95% power.

The cell's oblique wall allows collection at 80° from forward scattering. Focusing of the scattered light onto the PMT's photocathode is done by a Leica MZ6 stereomicroscope. The stereomicroscope is fitted with a 1.0x achromatic objective lens, and has discrete magnification steps of 0.63, 0.8, 1.0, 1.25, 1.6, 2.0, 2.5, 3.2, and 4.0x. The collection angle, or aperture, of the stereomicroscope at a working distance of 100 mm from bubble to lens is 25.4°, encompassing the range 67.3–92.7° from forward scattering. The stereomicroscope was attached to a rack-and-pinion axial positioner which moved it closer or farther from the cell's oblique face. This, in turn, sat on a wooden base that pivoted around the bubble center, and was locked down upon alignment by laser.

The photomultiplier tube utilized was a Hamamatsu 7696 PMT with a 51 mm circular plano-plano borosilicate glass window. It is a head-on box-and-grid style tube with a Sb-Cs cathode that has a "minimum useful area" of 40 mm diameter [15]. The spectral response is in the range 300–650 nm that peaks at 440 nm. Quantum efficiency at the laser wavelength of 632.8 nm is $\sim$1.5%. At the experiment temperature of 23–24°C, the PMT had a typical dark current of 0.6–1.0 nA. The PMT was used with its existing voltage divider base. The bias voltage was evenly divided amongst the 10 dynodes, the focusing electrode and the anode. The voltage between the cathode and the focusing electrode was twice that of all other stages.

The PMT was attached to the stereomicroscope by a phototube intended for CCD cameras. A delrin adapter was fabricated to attach a C-mount phototube insertion piece to the PMT face so that the photocathode was positioned at the focus of the phototube. The light incident on the PMT was bandpass filtered at 632.8 ± 10 nm by a Thermo-Corion optical filter. This filter significantly decreased incoherent noise caused by ambient light leakage.

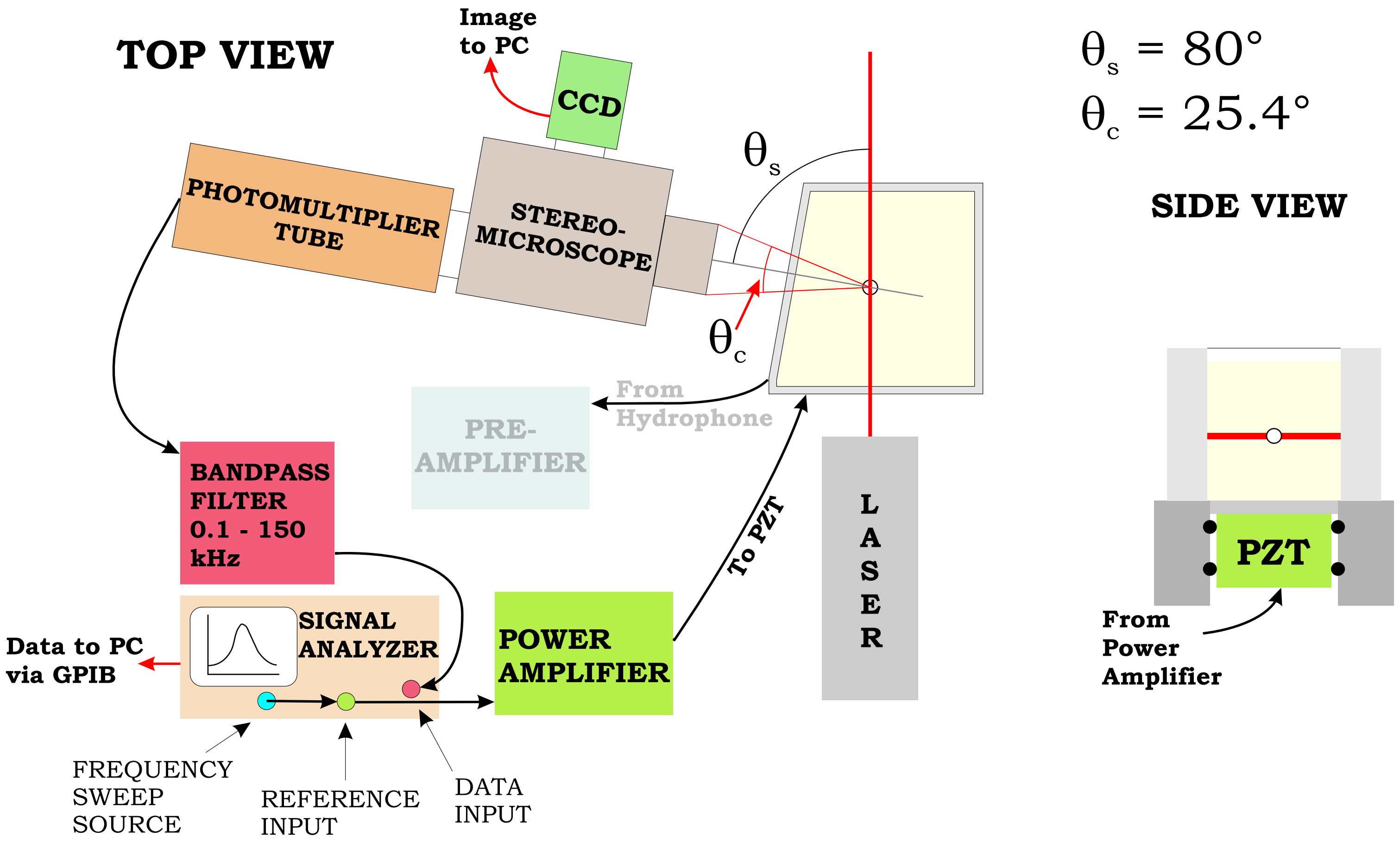

Figure 3.3: Apparatus for optical measurement of the bubble response to acoustic forcing. While the bubble is driven into oscillation by the PZT transducer, scattered laser light is simultaneously focused by a stereomicroscope onto the PMT. The optical signal is transduced to an AC electrical signal, which is filtered and collected by the signal analyzer.

The voltage measured across the anode of the PMT during a typical optical scattering experiment was of the order of -90 volts DC with a 10–100 mV AC component, depending on bubble alignment and size. To extract such a small AC component, the signal was AC coupled at 1 MΩ input impedance to a Krohn-Hite 3944 filter. The signal was bandpass filtered at 0.5–150 kHz through a 4-pole Butterworth filter that had 24 dB/octave roll-off. The PMT signal was then terminated either at a 200 MHz LeCroy LT224 digital oscilloscope to monitor the DC response for alignment purposes described below in Section 3.6, or the second channel of the DSA to be described in Section 3.7.2 for data-taking purposes.

3.5.2 Optical Imaging Apparatus

The system developed to image a bubble is shown in Figure 3.4. The CCD camera used

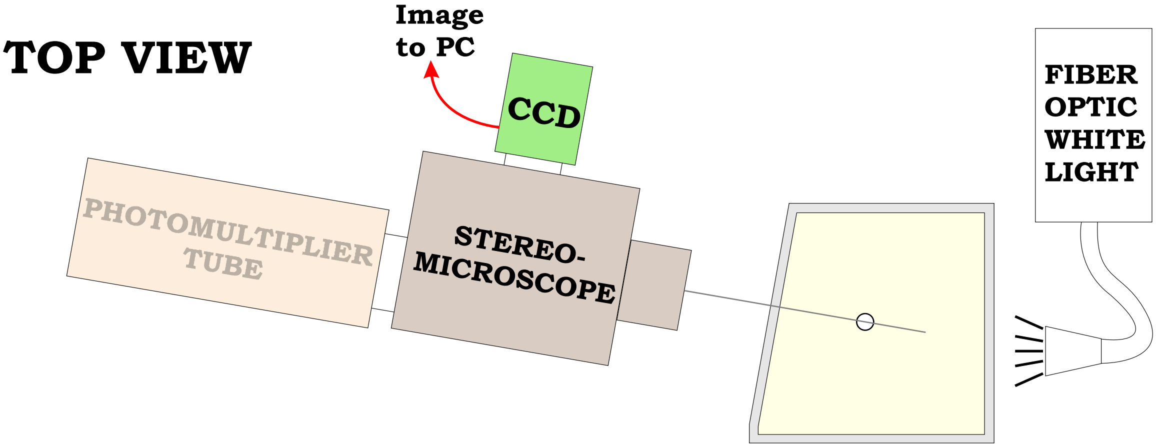

Figure 3.4: Optical imaging apparatus.

to image the bubble had its own attachment to the stereomicroscope separate from that used for the PMT. The field of view (FOV) of the camera, shown as the left image of Figure 3.5, was twice as large as that of the PMT, which is shown as the right image in the same figure. The PMT was replaced by a second CCD camera in order to make this image comparison. It is important to note that both the imaging camera and the scattered-light-sensing PMT saw the same image simultaneously during the measurement. Although the

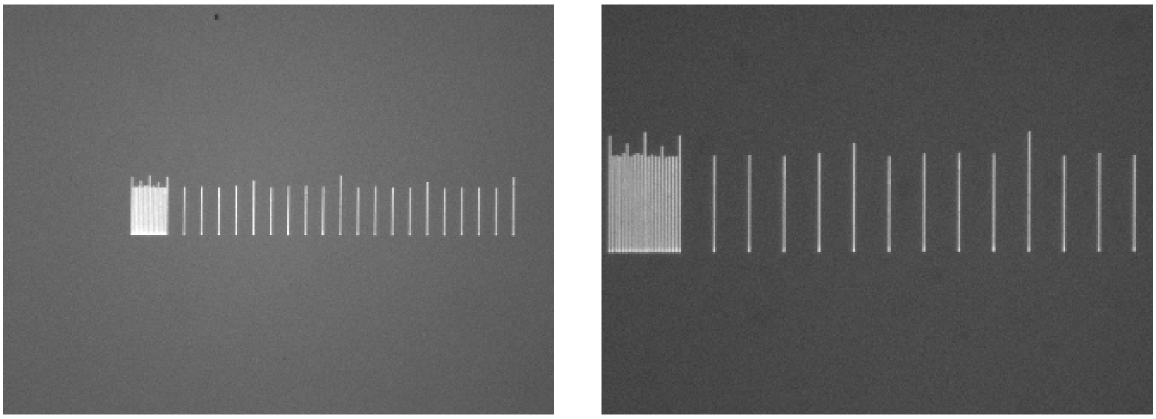

Figure 3.5: The left image shows the field of view seen by the CCD camera. The right image is the field of view seen by the PMT through the phototube. The coarse scale is 100 μm, the fine scale is 10 μm and the magnification represents that used while measuring a bubble's frequency response—4.0x with a 1.0x achromatic lens.

bubble was illuminated by laser light during experiments, it was still possible to monitor gross translational motion of the bubble using the imaging camera. This was done to ensure that the bubble did not rise out of alignment in the course of an experiment. Refer to Figure 3.6 to see a single bubble illuminated in the left frame, by diffuse white light, and in the right frame, by laser light.

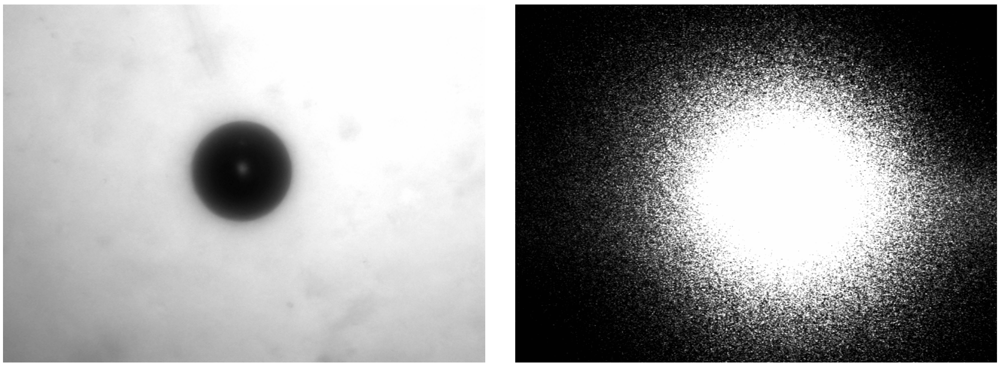

Figure 3.6: This is an example of the results of the optical imaging system. The left image shows a 318-μm radius bubble illuminated by diffuse white light. The right image is the same bubble illuminated by laser light.

The CCD camera is a monochromatic Sony XC-75CE with a 0.5" interline transfer hyper

HAD charge-coupled device chip. The active element consisted of 752(H) x 582(V) picture elements. Electronic shuttering was possible to 1/10000 second but was not used since all images captured were of the static bubble.

The adapter used to attach the camera to the stereomicroscope is made by Leica and contains a 0.5x lens. The lens is responsible for the doubled FOV, and is useful for initially finding and focusing on the bubble. The smaller FOV of the PMT is advantageous in focusing on the light scattered only by the bubble to the exclusion of gel-scattered or stray background light.

3.6 Calibration and Alignment

It is important that we demonstrate the linearity of the PMT response to both changing light intensity and the frequency of light fluctuations. With the stereomicroscope phototube insert connected to the PMT via the delrin adapter, a Kingbright 52 mm diameter 50-LED array, with center wavelength $\lambda = 660 \pm 20$ nm, was placed in front of the PMT, and the light output was varied by adjusting the current to the array to determine different regimes of PMT response to the DC photon flux, and how those regions varied with changing PMT bias voltage. It was determined that there are two major regimes: a nonlinear photon-counting regime and a mostly-linear photon saturation region as shown in Figure 3.7. All experiments described below were performed in the linear saturation region, where the bias voltage was used to assure response linearity for a given flux of light scattered by the stationary bubble. Moreover, linearity was further enhanced by the fact that the dynamic bubble excursions were very small, and thus the global deviations from linearity observed in the “saturation” region of Figure 3.7 will have little or no effect on the measurements from a given bubble.

In order to determine the frequency response of the PMT, a rise time measurement was performed on the PMT with the LED array driven by a 130 ns current pulse. The bandwidth of the LED array was given as 8 MHz, but the slower of the LED array or the PMT was the limiting bandwidth measured. It was determined that the slower of LED and PMT rise times was 230 nanoseconds, giving a maximum bandwidth of 4.3 megahertz – well above the maximum frequency of bubble oscillation measured. The frequency response of the photodetector is therefore assumed to be flat over the frequency range of interest.

Alignment was initially done with the cell full of water and with the procedure as follows. The key to alignment is location of the bubble in the cell. The intention was to find a position with the least number of resonances, but high enough pressure amplitude to induce a measurable bubble oscillation. After a small region was chosen, the cell was bolted to an immovable plastic plate that was itself fixed to x- and y-axis linear translation stages and a z-axis lab jack. This ensured that the cell would always start within the range of the translators when a bubble was inserted at the desired location. The translators were set at the middle of their ranges and the laser was positioned to illuminate the desired area.

The parallel windows were the primary alignment reference for the laser. Since each window has a finite thickness, the laser beam striking it at an oblique angle results in two primary reflections: one at the air/glass interface upon entering the window and one at the glass/water interface as the beam exits the window. If the beam is perpendicular to the glass, there will be no reflections deviating from the axis of the beam. Of course, this assumes optically flat glass surfaces and window installation perpendicular to the horizontal plane defined by the floor of the cell.

The microscope was aligned by a second laser shining through the window perpendicular to the two parallel windows, then through the oblique window as shown in Figure 3.8. The second laser crossed the path of the first at the desired bubble position, and terminated through the oblique window at the stereomicroscope. When there were no visible beams reflected from the oblique window, the laser was considered to be at 80° to the forward. The microscope was then positioned so that the beam hit as close as possible to the center

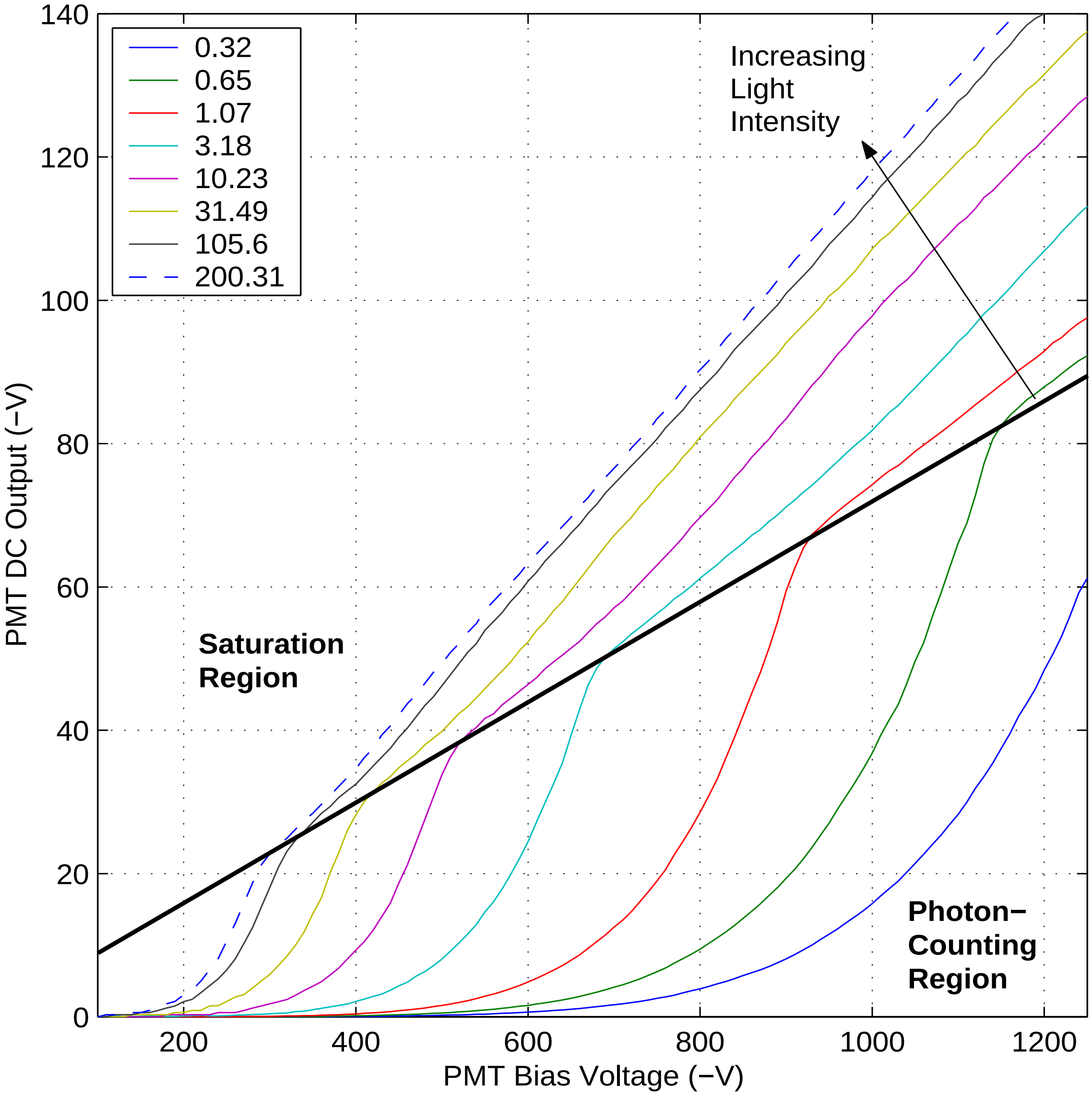

Figure 3.7: DC output of PMT versus PMT bias voltage for varying light outputs of the LED array. The legend lists the current supplied to the LED array in mA.

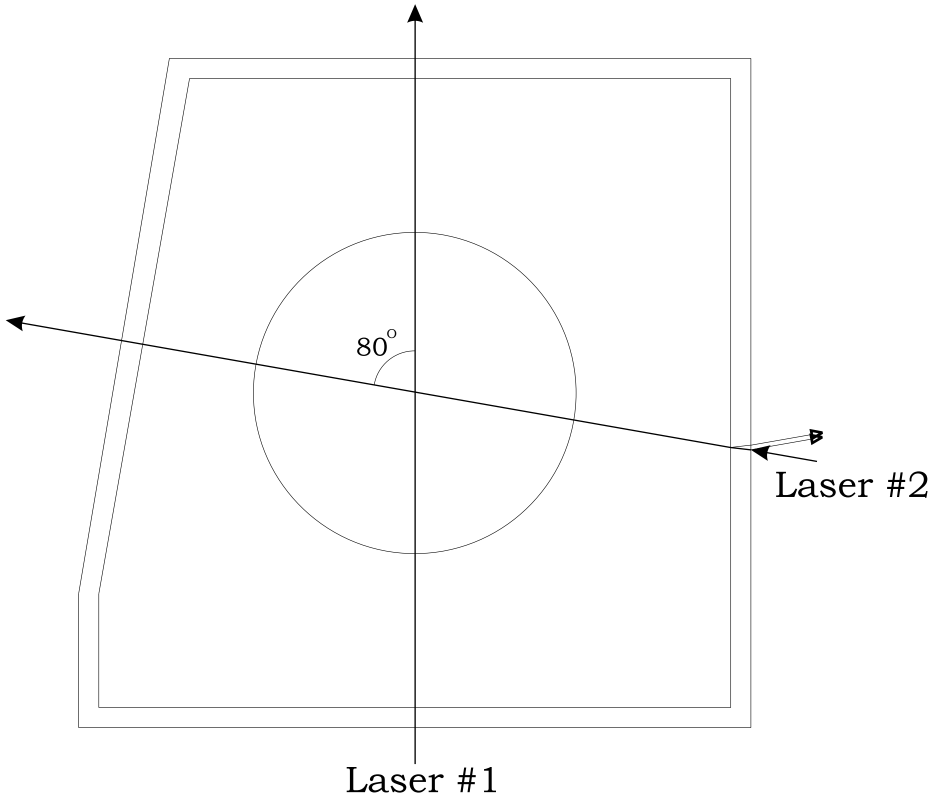

Figure 3.8: Optical alignment: Looking from the top, the two lasers are coplanar. Each is positioned so that there are no reflections from the glass deviating from the axis of the incident beam as shown on the right window. The second laser is not used for experiments, but for aligning the microscope and PMT to the correct angle of 80° from forward.

of its collection lens, which was verified by a CCD image.

3.7 Data Acquisition

There were a total of three different measurements made in this experiment, two optical measurements and one acoustical measurement. A CCD imaging camera was used with white backlighting of the bubble to take photographic images of the static bubble. The second optical measurement acquired was the collection of laser light scattered from the driven bubble. Finally, characterization of the frequency-dependent pressure field of the cell at the bubble position was the third measurement.

3.7.1 Frame Grabber

To photograph the bubble, a National Instruments PCI-1411 frame grabber was used in conjunction with the IMAQ package in National Instruments LabView 5.1. A resulting image has 640×480 pixels in 8-bit resolution greyscale. The frame grabber is capable of 30 frames-per-second video and was used in continuous capture mode to line up and bring into focus the bubble onto the PMT photocathode. Static images of the bubble were also taken for sizing purposes.

Upon capturing an image to hard disk with the IMAQ program, Scion Image [40], a PC adaptation of the National Institute of Health's image processing program NIH Image, was used to determine the size of the bubble. To accomplish this, the scale shown in the left frame of Figure 3.5 first sets the pixel-to-micrometer conversion. Images were captured at a resolution of 0.201 pixels per μm, or just under 5 μm per pixel. Four measurements of the bubble diameter were taken at different diameters to minimize the effect of any optical aberration in the image. These diameter values were then averaged and halved to give a mean bubble radius. Assuming that the measurements are within 2 pixels on each edge, the correct radius will be within 14 μm of the measured value. The corresponding error is 5.8% at the smallest measured radius of 240 μm and 3.0% at the largest of 470 μm (see Section 4.4 for full development).

3.7.2 Signal Analyzer

To measure frequency response curves an HP 3562A digital signal analyzer (DSA) was employed as signal source and receiver. It has 13-bit, 80 dB dynamic range, a 100-kHz bandwidth, and a 1 M$\Omega \pm 5\%$ shunted by < 100 pF input impedance. A frequency-swept chirp sourced by the DSA, which becomes the source, or reference, input, also drives the

PZT after power amplification. The data signal is received, after bandpass filtering 0.5–150 kHz, at the second input to the DSA.

The process by which the analyzer makes a measurement is as follows. The analog-to-digital converter samples the incoming voltage data at a fixed rate of 256 kHz, or one data point every 3.91 μs. One time record is defined as 2048 points, or one full record every 8 ms at the maximum bandwidth of the DSA. A digital filter then resamples the data to fit the time record required for the chosen frequency band. All frequency domain data has 800 points per record. So, for example, a 5 kHz band requires 800 pts/5000 Hz = 160 ms time record. To fill a time record of 2048 points requires 0.16 s/2048 pts = 78.1 μs/pt, or every 20th data point the analyzer samples in the time domain.

Next the time record is multiplied by the desired windowing function, which, for this thesis, was a Hann, or raised cosine, window to ensure periodicity. The Hann window function is given in the time range $0 \leq t \leq T$ by

$$w(t) = \frac{1}{2}\left(1 - \cos\left(\frac{2\pi t}{T}\right)\right), \tag{3.2}$$

where T is the period of the complete time record. There was no overlap of the window between consecutive time records so there was some attenuation of the highest and lowest frequencies in a given band. However, because the optical scattering and acoustical pressure measurements were processed by the same method with the DSA, the response in a given frequency band of the optical scattering measurement was given the same attenuation as the corresponding data in the acoustical pressure measurement.

The frequency response is calculated as follows: both time traces are fast-fourier transformed (FFT) into the frequency domain. We shall define the one-sided (valid only for positive frequency, $f > 0$) cross-spectral density function, as follows [1]

$$G_{sp} = F_s^* F_p, \tag{3.3}$$

where F_s^* is the complex conjugate of the FFT of the source frequency chirp as represented in the time domain, and F_p is the FFT of the time-domain PMT output. We also define the one-sided autospectral, or power, density function as the FFT of the source multiplied by its complex conjugate:

$$G_{ss} = F_s^* F_s. \tag{3.4}$$

The frequency response, $P(f)$, is then calculated by the DSA using the following formula

$$P(f) = \frac{G_{sp}}{G_{ss}}. \tag{3.5}$$

G_{sp} is complex-valued, while G_{ss} is purely real, with the result that the PMT response computed, $P(f)$, becomes complex valued. Since the amplitude of the driving frequency chirp was kept constant, G_{ss} had the effect of normalizing the frequency response to the input amplitude. Thus, the response computed represents what fraction of the source was transferred through the experimental system.

3.7.3 Computer Control

All of the synthesized data is retrieved from the DSA with the general purpose interface bus (GPIB) using the IEEE 488 standard with National Instruments Labview version 5.1 and a Dell Precision Workstation 410 PC computer running Windows 2000 with a 600 MHz Pentium 3 processor and 256 megabytes of RAM.

For a frequency response curve, the data is downloaded from the DSA buffer to the computer in 801 points regardless of bandwidth of the measurement. This is a constraint imposed by the DSA, with the consequence that the frequency resolution is dependent on the bandwidth of the measurement. For example, the least resolved frequency plots had bandwidths of 25 kHz, giving a frequency resolution of 25000 Hz/800 points (or data divisions) = 31.25 Hz/point.

3.8 Signal Processing

3.8.1 Signal Averaging to Minimize Noise

Uncorrelated broadband noise was minimized using 50 frequency-domain averages during the frequency response measurements. According to Fourier theory, a narrow bandwidth measurement requires a longer time record than a wide bandwidth measurement. So, the bandwidth determines the time it takes to acquire one data set. The narrowest bandwidth measurement made was 5 kHz, corresponding to a frequency resolution of 6.25 Hz with 801 points, and the longest time record of 160 milliseconds per sweep. For 50 averages, that is 8 seconds for a complete recorded measurement. All acoustic background measurements were averaged 10 times in the frequency domain on the DSA before downloading to computer. At the longest time record utilized, the complete measurement took 1.6 seconds.

3.8.2 Data Equalization

We assumed in Section 2.2 that the PMT response is linearly proportional to radius. Upon measurement of the radial pulsations of a bubble via optical scattering, the response recorded is a time convolution of the responses of the bubble, the cell, the PZT transducer and all electronics. Because a convolution in the time domain corresponds to a multiplication in the frequency domain, and all responses are linear, we can divide out the responses of the cell, PZT transducer, and electronics as measured with the hydrophone. For our purposes, we will term this procedure "equalization".

To do this, we used a linear, time-invariant filter that minimizes noise uncorrelated to the input signal. This technique is sometimes called Wiener filtering and is attributed to Norbert Wiener who first derived it in the 1940s [46]. Figure 3.9 shows the effect of the PZT transducer, the cell, and electronics on the bubble's frequency response. The known system response, a(t), is the acoustical measurement made after the bubble is removed from

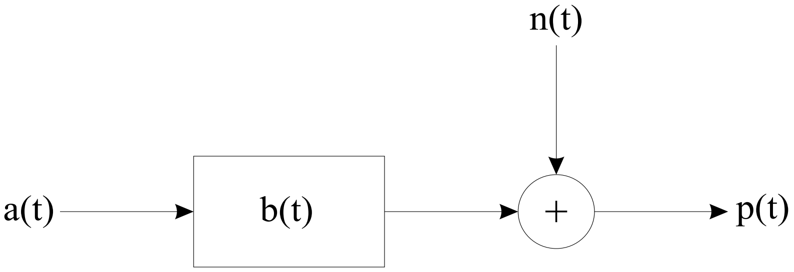

Figure 3.9: Effect of bubble on the known system response.

the cell, and is affected in the optical scattering measurement by the unknown response of the bubble, b(t). Noise, n(t), attributed to all electrical components of the system sums with the bubble/system response to become the quantity $p(t)$, measured at the output of the PMT. This can be written in the time domains as

$$p(t) = b(t) \otimes a(t) + n(t), \tag{3.6}$$

where $\otimes$ denotes the time-domain convolution. Use of the Fourier transform allows us to express the equation in the frequency domain as

$$P(f) = B(f)A(f) + N(f), \tag{3.7}$$

where a capital letter denotes the Fourier transform of the time-domain quantity represented by the same lower-case letter.

We will assume that the noise denoted by $n(t)$ is random and ergodic (also called wide-sense stationary), so that the statistical expected value can be approximated by the average measured value. Then, it is shown in Section 5.1.1 of [1] that minimization of the autospectral density of the noise, G_{nn}, leads to the optimum form of the bubble response as

$$B(f) = \frac{G_{ap}}{G_{aa}}, \tag{3.8}$$

where G_{ap} is the cross spectral density of the known system response and the measured output of the PMT, and G_{aa} is the power spectrum of the system response. Therefore, $B(f)$ is the desired complex frequency-dependent bubble response.

Using the definitions for cross- and auto-spectral density functions (Equations 3.3 and 3.4) with Equation 3.8 gives the form we will use to extract the bubble's response from the total response:

$$B(f) = \frac{G_{ap}}{G_{aa}} = \frac{A^*(f)P(f)}{|A(f)|^2}. \tag{3.9}$$

However, since the cell response is frequency dependent, there are going to be frequencies at which the acoustical response of the cell, and consequently the bubble, will be very low amplitude. Division of the small bubble amplitude measured by the PMT by the small pressure amplitude detected by the hydrophone would occasionally give rise to false peaks in the resulting equalized bubble frequency response. So, to avoid singularities, we used a form of the filter with a pre-whitening factor, ϵ, in the denominator [34]:

$$B(f) = \frac{A^*(f)P(f)}{|A(f)|^2 + \epsilon}. \tag{3.10}$$

The effect of the pre-whitening factor is to add a small level of white noise to the acoustical response to keep the denominator of Equation 3.10 from going to zero. The value used for ϵ was the average value of the optical noise background of the PMT with laser and acoustics on, but no bubble in the test cell. The noise value was determined to be in the range -80 to -100 dB re 1 Vrms, depending on the clarity of a given batch of gel. So, ϵ took a value between 10^{-4} and 10^{-5}.

In essence, the gain of the filter is unity for a high signal-to-noise (S/N) ratio, and the filter itself acts like an inversion filter. But for a low S/N ratio like the situation described above, the ϵ term becomes comparable to the magnitude of the acoustic response squared. The strong false peaks are therefore mitigated. This filter was implemented through scripts written in The Math Works' technical computing software Matlab release 11, version 5.3.

3.9 Xanthan Gel Preparation

The gel used for all experiments outlined here undergoes the following method of fabrication. Distilled water, filtered through a 0.2-μm particle filter, is poured into an Erlenmeyer filter flask and a 1" stir bar is inserted. The flask is sealed at the neck opening with a rubber stopper. The filter nozzle is hooked up to $\geq$ 29" Hg vacuum, using either a Venturi pump or an aspirator pump for 30 minutes or more.

After the water is sufficiently degassed, 800 ml is poured into a "French press" coffee carafe container with a magnetic stir bar. Enough sodium chloride reagent is added to give the gel a 3.5% salinity, identical to seawater (3.5% = 28 g in this instance). It is measured by digital scale and added to the water until dissolution occurs, while the water is magnetically stirred at approximately 550 revolutions per minute (rpm).

Next the saltwater is put aside to mix the final three components. On the digital scale, 24 grams of propylene glycol, which acts as a dispersant for the polymer, is measured in a mixing boat. Added to it are 4 grams of Neodol 91-6, an alcohol derivative made by Shell Chemical that acts as a surfactant, and 5.2 grams of Xanthan gum powder to make the gel 0.65% Xanthan gum by weight. This is all mixed together manually with a rod until relatively homogeneous, then the mixture is added to the saltwater while the magnetic stirrer is once again set at 550 rpm. This mixing occurs for 15 seconds on average to ensure all components are mixed thoroughly, yet allows minimal air to become entrained that would cause microbubbles to form.

Immediately after mixing ceases, the French press plunger is inserted obliquely into the gel so as not to entrap air beneath its face. The plunger is pressed slowly through the gel to preclude cavitation and minimize any air trapped in the mesh from breaking apart into smaller bubbles, which are harder to extract from the resulting mixture.

The gel is poured into the acoustic cell soon after it is pressed as it becomes more difficult to achieve a homogeneous result the longer the polymer chains have been linked.

A section of L-shaped aluminum bar, acting as chute, is laid across the body diagonal of the cell so the gel can be slowly poured into the cell without entraining air bubbles. The pouring is stopped any time bubbles appear in the mixture so they can be removed by syringe or pipette. Pouring is ceased once the gel is within 1 cm of the top to allow room for the gel to rise when the bubble injection pipette or the hydrophone is inserted.

A note must be made about the qualitative optical features of the gel over time. For approximately one day after the gel is prepared, the optical quality vis a vis the CCD image taken through the Leica stereomicroscope of a single bubble of radius typical to this experiment was observed to be less clearly resolvable than after that first day. However, once the gel has sat in the cell in room temperature ($\sim 23°$C) for 3 or more days, its optical quality is degraded by organic growth. The data presented in the next chapter was all taken within 1–2 days after the day the gel was initially mixed.

As for the quantitative parameters of the gel, few were able to be measured. A sound speed measurement was performed in a small fish tank using time-of-flight methods. Measurement at low frequencies was not possible as the apparatus was designed to work at megahertz frequencies. Nevertheless, the bubble-free gel was determined to have a sound speed at 1 MHz and 21.4°C of 1539 ± 1 m/s.

A density measurement was made using two methods. The first method involved weighing a known volume of gel in air and water, and comparing it to similar measurements of a known volume of distilled water. As a check, the gel was also measured using a handheld AP Paar densimeter that worked by oscillating a known volume of gel and measuring the resulting frequency. In this way, a density of 1034 ± 2 kg/m^3 was determined.

Finally, a Cannon LV2000 concentric cylinder viscometer was employed to measure the viscosity of the gel. The test with the viscometer was inconclusive. Repeated measurements yielded different results. Now, Xanthan gel is visco*elastic*, so for a proper measurement, a rheometer must be used to measure the viscosity and the elasticity components. However, a rheometer was not available. Nevertheless, the flow between two concentric cylinders and the radial oscillations of a bubble cannot be considered similar flow regimes, but the measurement is documented in this thesis for completeness.

3.10 Experimental Methods

What follows is a description of how a frequency response measurement of a bubble was carried out. For this experiment, the frequency response through resonance of bubble radii in the range 240–470 μm, covering a frequency range of 6–14 kHz, were measured. This range of radii corresponds to an optical range for ka of $ka = 2383$–4667. The small bubble radii were hampered by low S/N ratios, while the larger bubbles tended to rise quickly enough that the purpose of the gel in holding the bubbles was counteracted. Throughout the course of the measurements, temperature of the gel in the cell was monitored and was always within the range $23 \pm 0.5°$C.

3.10.1 Bubble Insertion

The cell is filled by carefully pouring gel down a chute fashioned from a metal bar with "L" cross-section laid across the body diagonal of the cell. The cell is filled to 66 ± 0.1 cm height. After the gel-full cell is bolted to the translation stages, a bubble must be inserted. The remainder of the newly made gel is poured into a beaker to save throughout the rest of the experiments with that batch. A beaker separate from that is used to contain a small sample of that remaining gel and has been deliberately poured from a height to entrain air bubbles. Using a manual pipette pump with a 1 ml pipette, less than 0.1 ml bubble-free gel is drawn up, then a bubble with radius larger than required for the experiment is drawn up followed by ~0.1 ml bubble-free gel. The larger bubble is needed to give setup time for the experiment because dissolution begins immediately after insertion into the cell. Figure 3.10 shows a typical dissolution curve. The trend is calculated with two experimentally

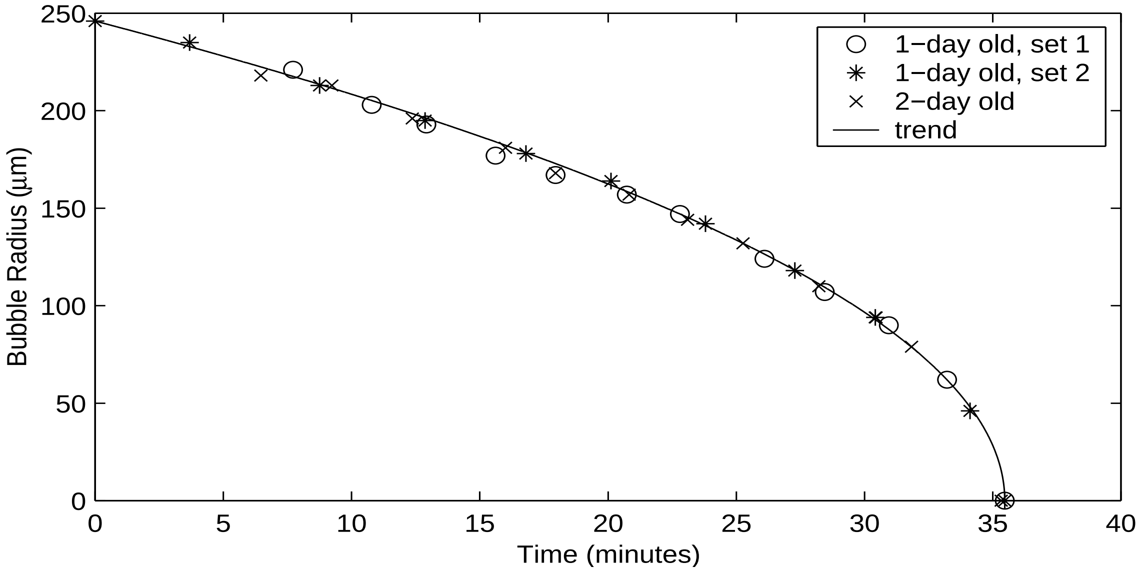

Figure 3.10: Undisturbed bubble radius versus time measured with 2 bubbles in 1-day old gel and 1 bubble in 2-day old gel. Most measurements were taken in 1–2 day old gel, the time period in which it was most transparent. This is discussed in Section 3.9.

determined values, the starting equilibrium radius, R_0, and the time the bubble finally extinguishes, t_{ex}. The form of the trend fit to the data is shown here:

$$R = R_0\sqrt{1 - \frac{t}{t_{ex}}}. \tag{3.11}$$

Dissolution time is proportional to radius squared, or the bubble's surface area, as expected, as that is the barrier across which the gas diffusion takes place. This knowledge was used as a guideline to correct the measured bubble radius for the passage of time between an optical image taken of a bubble and the actual optical scattering measurement, or vice versa.

Two translation stages are positioned above the cell, allowing translation of the bubble-insertion pipette both along the laser beam axis, and in the vertical direction. Attached to the stages is a clamp used as a guide for the pipette. Below that, fit by grooves directly onto the top of the cell, is a plastic piece as shown in the right frame of Figure 3.11 designed to allow repeatable position measurements. Guiding the pipette through these three contact points allows bubble placement repeatability to within 1 mm.

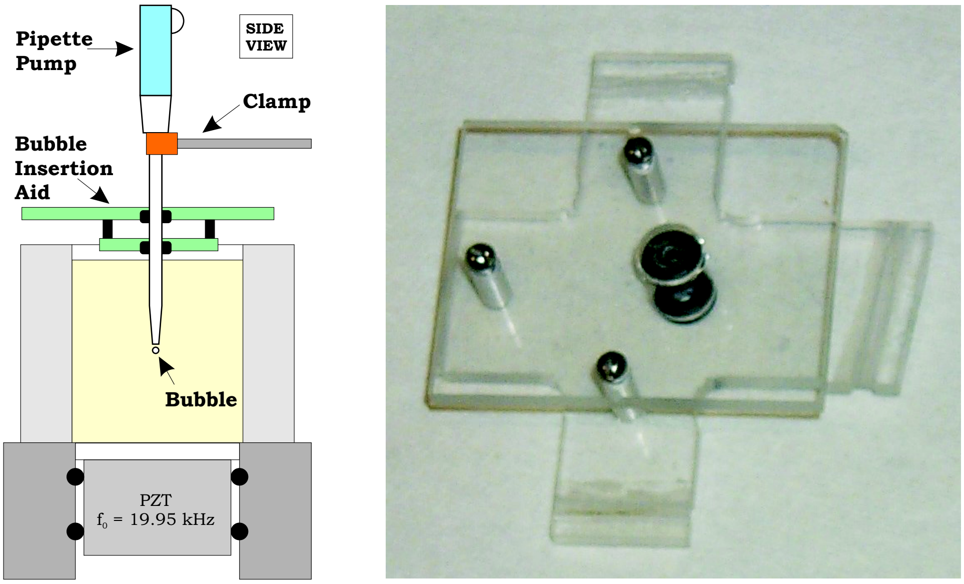

Figure 3.11: The bubble insertion aid is shown in use in the left image. A photo of the aid is shown in the right image. The grooves fit securely onto window edges of cell. The pipette is inserted through spaced grommets to allow repeatable bubble deposition into the cell.

Any air in the pipette tip is discharged before the gel in the cell is entered — the extra bubble-free gel in the pipette should allow for mishaps so the bubble is not accidentally ejected early. Once the bubble is in the cell, it will either stay directly below the exit point or it will flow around the pipette tip edge until parallel to, or above, the plane of the pipette tip bottom, all depending on how much extra gel is pushed out after the bubble. The largest margin of error comes from pulling out the pipette from the gel because the bubble tends to follow the broken-polymer-link trail left by the pipette upon removal. However, the bubble rises 1–8 mm depending on the speed of pipette removal.

3.10.2 Bubble Alignment

Upon successful insertion of a bubble into the bubble-free gel in the cell, aligning the bubble in the laser, as well as with the sensing elements of the CCD camera and PMT, can commence. First of all, the CCD camera, the frame grabber, and the background lighting are turned on. Lighting of the bubble is done as shown in Figure 3.12 so that the background is light and the bubble is dark. Processing of the resulting snapshots of the bubble is done without digital thresholding as it is done manually before the shot is taken by the setting of the background white light source. Next, the cell is moved and magnifications of the stereomicroscope are adjusted back and forth with an overall zoom-in trend until the bubble is found in the center of the 4.0x magnification. Then the laser's shutter is opened and the cell is moved, keeping an eye on the frame grabber image so the bubble does not wander out of the field of view, until the bubble is within the beam as seen by the eye. The laser shutter is closed again and the bubble is focused on the CCD with background lighting only. The bubble is now coarsely focused for the experiment.

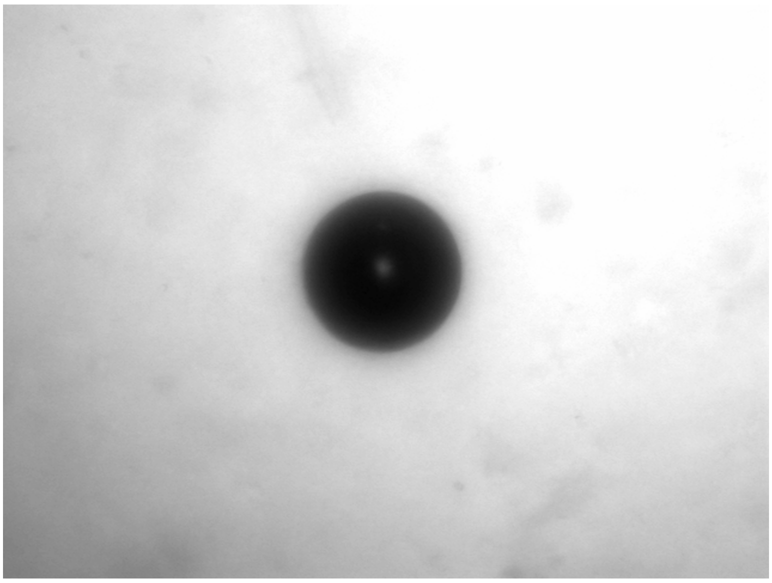

Figure 3.12: Example of optical imaging of a bubble at greatest possible magnification of 4.0x. The bubble radius is 333 μm.

A CCD snapshot is taken of the bubble with only background lighting for later processing. The room and background lights are shut off and the laser shutter is opened. Aside from the equipment in the room, the laser should be the only light source on. The negative bias voltage to the PMT is turned on and the DC output is monitored. The PMT is directly connected to the oscilloscope when positioning a bubble to establish that the DC output is consistent with the tube operating in its “saturation” (or non-photon-counting) regime. Typically the PMT was biased with -1250 volts, the maximum output the high voltage supply used, to allow the light scattered from smaller bubbles to fall in the linear response regime. Once saturation is verified by ensuring the DC output to be greater (more negative) than -90 volts, the DC response is maximized by fine adjustment of the cell, and hence bubble, position.

3.10.3 Experiment

The frequency chirp is then enabled by closing the circuit between the power amplifier and the PZT attached to the cell. The DSA takes data from the PMT in free-run mode until the S/N ratio is deemed satisfactory to acquire a 50-average-spectrum. This is more of a qualitative qualification and depends on how many stable peaks can be seen in the realtime data. The resolution of the cell resonances at 8.6 and 20 kHz as well as at the bubble resonance frequency were generally the minimum requirements to start the 50 averages leading to the recording of the data. Simultaneously, the realtime image from the CCD camera of the bubble illuminated by the laser light is monitored on the computer screen to ensure minimal translating motion from the bubble. In this way, it is usually obvious when and why the PMT signal is lost because the bubble will move.

If this is the case, the measurement is stopped and the bubble is realigned by again maximizing the DC signal from the PMT. Then the PMT high voltage is shut off while the back light is turned on to ensure the bubble is in focus with the CCD camera. The PMT high voltage is turned back on and very fine adjustment is made in position only if the bubble is not in the saturation region of the PMT according to the cutoff value of -90 VDC mentioned before.

After successful acquisition of a data set, the sound field is turned off, the PMT high

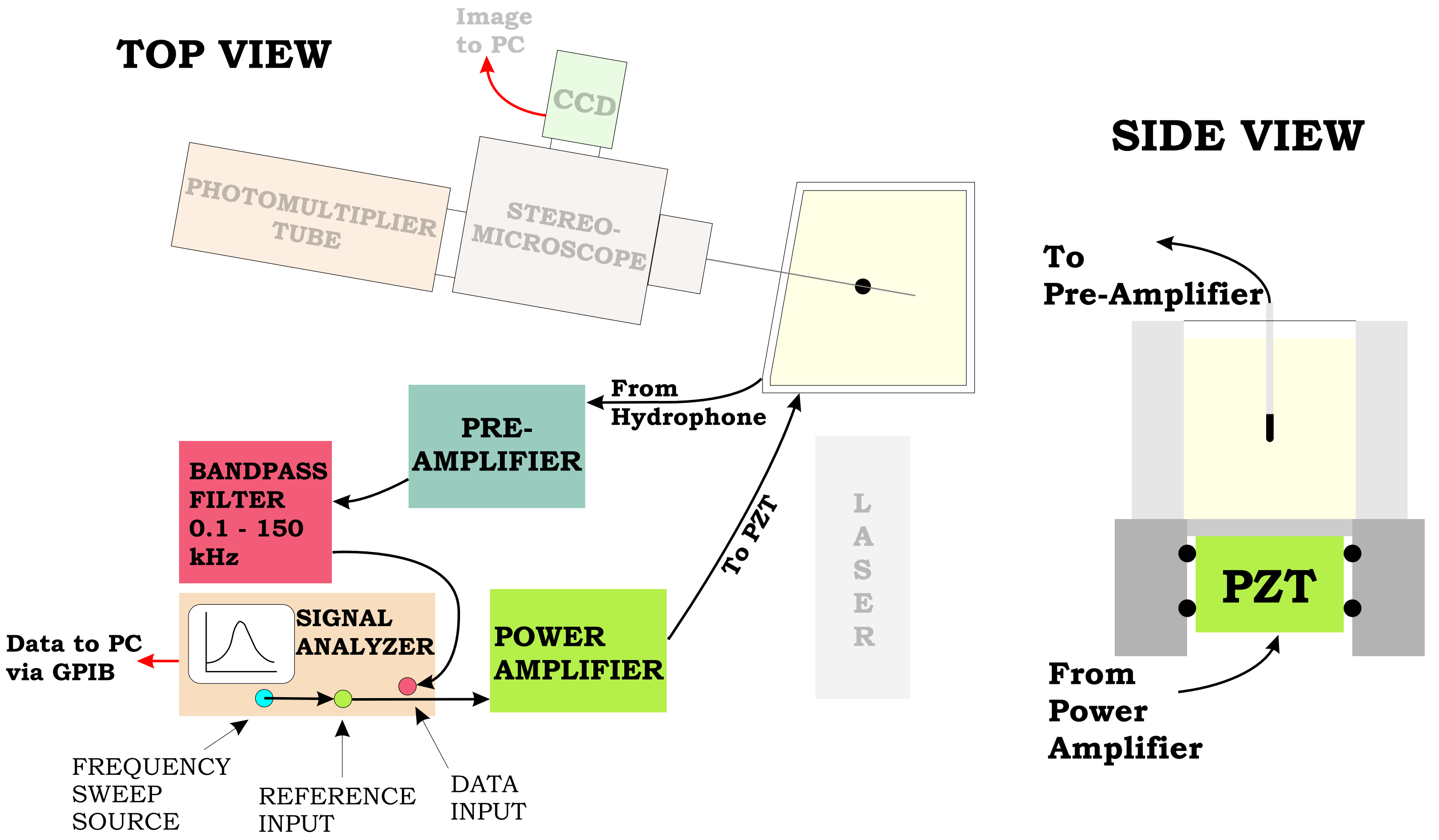

Figure 3.13: Apparatus for the acoustical measurement of pressure field in the cell. The hydrophone's acoustical center is positioned by laser and CCD image to the same spatial location previously occupied by the bubble. Acoustical excitation of the cell is then enabled, and the frequency-dependent pressure field of the cell is calculated by the signal analyzer.

voltage is shut off and the back light is turned on again. A CCD image is taken as soon as possible after the data acquisition to ensure accurate measurement of the equilibrium bubble radius. As long as there are not any translating adjustments of the bubble greater than 1 mm, the bubble is then allowed to dissolve to a smaller radius and another measurement is made. This process is repeated until the S/N ratio is too low or the bubble moves appreciably. If the latter has occurred, the bubble is removed and the acoustic measurement is performed. The result is a series of frequency response curves for bubbles of varying equilibrium radii. These curves include the influence of both the acoustical resonances of the cell and the electrical resonances of the PZT transducer. As described earlier, these corrupting effects are equalized out using the measured acoustical response of the cell itself.

To measure the frequency-dependent acoustic pressure background experienced by the bubble, none of the translators are changed after the removal of the bubble. In fact, less then 0.1 ml gel is removed from the cell, so there is no movement of the gel level in the cell as well. A Reson 4038 hydrophone, encased in a thin-walled stainless steel sheath filled with gel, is carefully lowered to the location of the bubble as shown in the acoustical apparatus of Figure 3.13. A tiny line of white-out marks the acoustic center of the hydrophone and easily contrasts with the black rubber enclosing the active element of the hydrophone. Simultaneously, a reflection of the laser on the white-out is sought, along with alignment of the hydrophone using the realtime CCD image. After both are satisfied, 10 frequency-domain averages of the hydrophone response to the optical measurement frequency chirp are recorded with the DSA.

The bubble response must then be extracted from the raw data by the method outlined in Section 3.8.2, but that is the subject of the next chapter.

Chapter 4

Experimental Results and Analysis

Now we have an experimental apparatus and a method to measure the frequency response through resonance of a bubble suspended in Xanthan gel. We will present in this chapter the analyzed data and its comparison to expected results.

4.1 Response Versus Frequency for a Fixed Bubble Size

When the optical scattering measurement is performed, the resulting frequency response curve includes more than the bubble response alone. The total response is the time convolution of the response of the electronics, the cell, the piezoelectric (PZT) transducer, and the photomultiplier tube (PMT). However, utilizing the output of the acoustical measurement, which includes the responses of the cell, the PZT transducer and the electronics, and assuming a flat response from the PMT, the bubble response can be extracted from the raw PMT output. Figure 4.2 shows an example of the raw PMT output from the digital signal analyzer (DSA). The spectrum of the pressure field experienced by this bubble is shown in Figure 4.3. As you can see, the PMT curve contains an extra peak near 10.8 kHz that is attributable to the bubble's resonance.

Assuming the linear response of the PMT described in Section 2.2, we can use the

Wiener filter described in Section 3.8.2 to equalize out the responses of the cell and related electronics. For the current example, equalization results in the magnitude and phase responses shown in Figures 4.4 and 4.5. The corresponding image of the stationary bubble taken with the CCD camera is shown in Figure 4.1 immediately before the sound field was turned on and the dynamic bubble response measured. The size of this bubble as measured using the Scion Image program is 304 ± 14 μm, which corresponds to a Minnaert resonance frequency range of 10380–11382 Hz. The magnitude response shown in Figure 4.4 has a peak at 10847 Hz, comparable to the expected resonance frequency when we account for experimental error. As you can see, the signal-to-noise (S/N) level of this data is high, so the ϵ term in the denominator of Equation 3.10 has a negligible effect on the outcome of the equalization process.

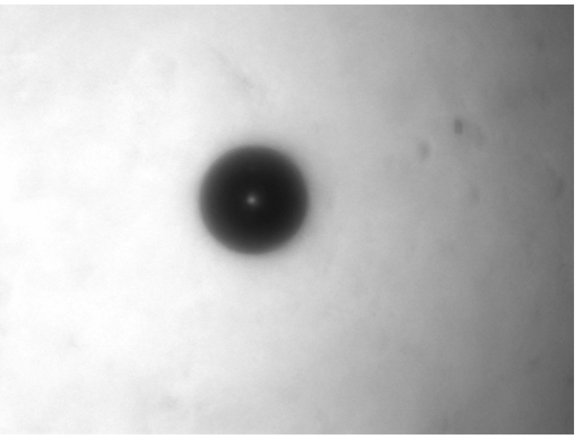

Figure 4.1: Image of a 304 μm bubble taken with the CCD camera.

4.2 Least-Squares-Error Parameter Fit

Now that we have data attributed to the bubble response only, we will compare it to the damped harmonic oscillator theory, outlined in Section 2.3, used to model the bubble's behavior. To accomplish this, a least-squares-error method was employed to determine the

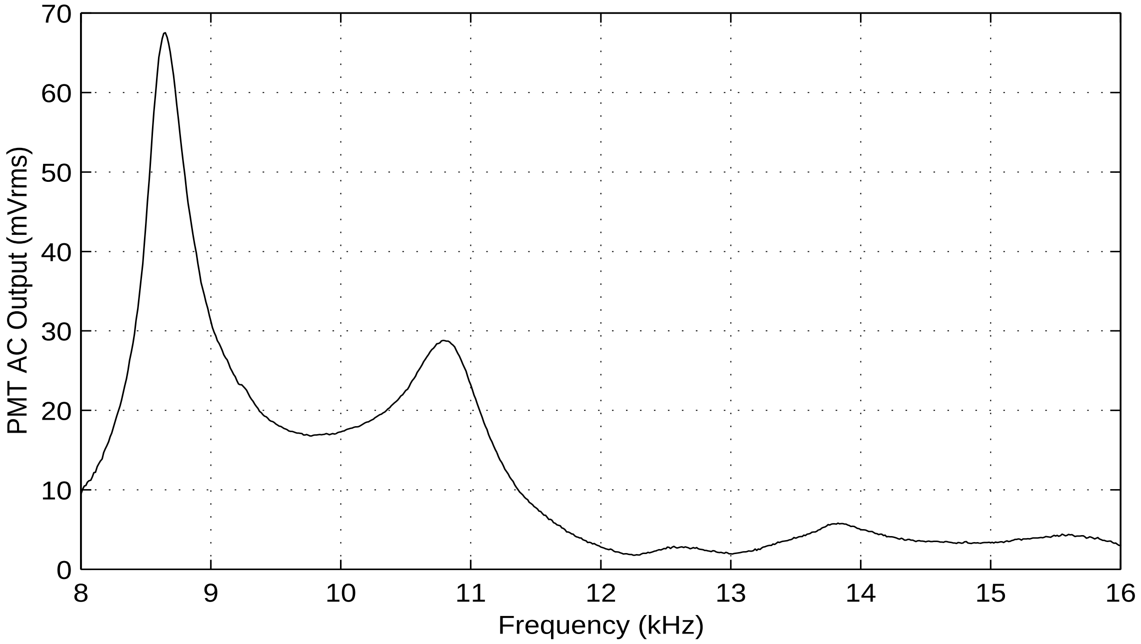

Figure 4.2: Unprocessed PMT output: peaks at 8.7, 12.6, 13.9, and 15.6 kHz are cell-related resonances; the bubble resonance is the peak at 10.8 kHz.

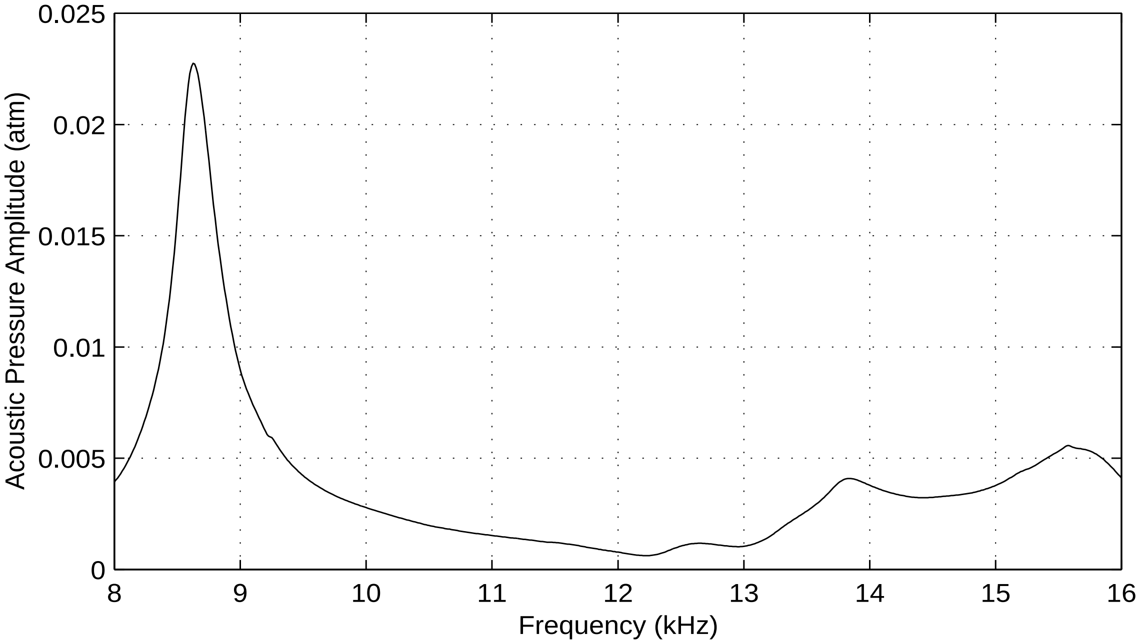

Figure 4.3: Frequency-dependent peak acoustic pressure measured with a hydrophone in same spatial location as bubble in Figure 4.2.

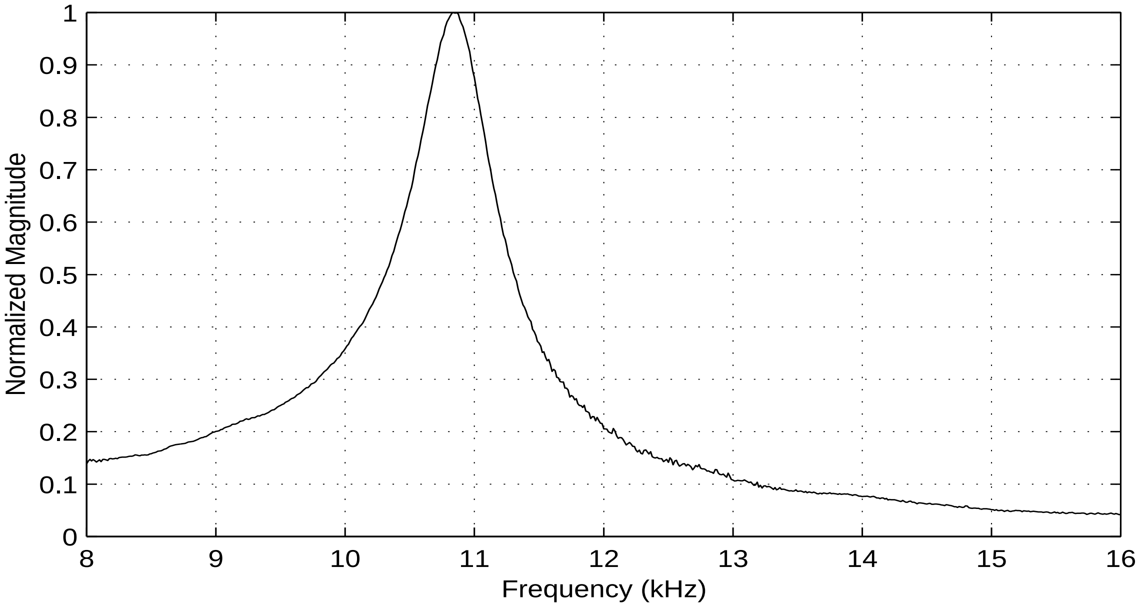

Figure 4.4: Normalized magnitude of the bubble response using Wiener filtering to equalize out the background pressure spectrum shown in Fig. 4.3, from total response shown in Fig. 4.2.

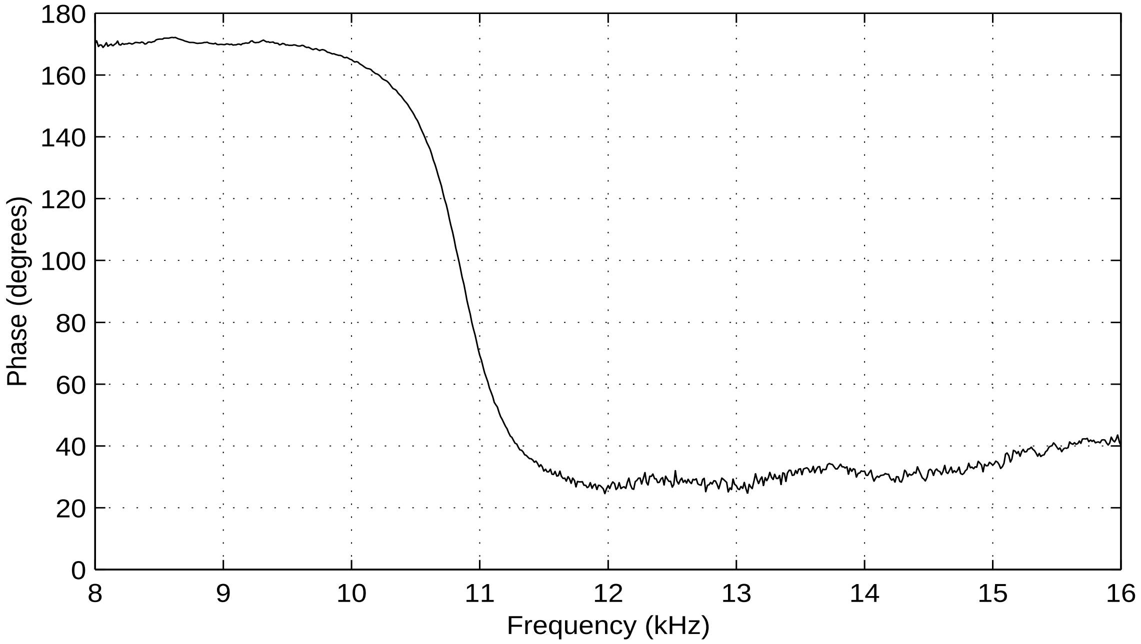

Figure 4.5: Phase of the bubble response using Wiener filtering to equalize out the background pressure spectrum shown in Fig. 4.3, from the total response shown in Fig. 4.2.

best fit of the theory to the equalized PMT output. The two fit parameters employed were the resonance frequency, ω_0, and the Quality factor, Q.

As a starting point for the parameters, first a radius was determined from measurement of the optical image of the bubble. Using Minnaert's equation (Eqn. 2.48), a resonance frequency of a given bubble was then estimated. This became the starting ω_0 parameter. Next, the expression for the quality factor, Equation 2.23, can be utilized in conjunction with the ω_0 estimate to make a guess at an initial value for Q. The two estimated parameters were then processed with the equalized PMT data through two iterations of a least squares error script. As a side note, processing of all data was done with scripts written in the technical computing software Matlab release 11, version 5.3, and the scripts are catalogued in Appendix C.

In the parameter-fit scripts, the total squared error was defined in the standard way [2]:

$$E_{total} = \sum_{f=f_-}^{f_+} (T(f) - D(f))^2, \tag{4.1}$$

where f is the frequency, $T(f)$ and $D(f)$ are the fitted values and raw data points at a given frequency, and the bandwidth of the measurement has upper and lower bounds f_- and f_+. In the first iteration, the squared error is computed within ±1000 Hz around the resonance frequency estimate using a resolution of 10 Hz, and ±5 around the Q estimate using a resolution of 0.5. Where the error is a minimum, a better estimate for the two parameters results from this iteration. Using these parameter values for the second iteration, the squared error is computed within ±30 Hz, with 1 Hz resolution, around the starting ω_0 value, and ±1, with 0.1 resolution, around the initial value of Q. The resulting values of the second iteration then were used to evaluate a damping coefficient as outlined in the next section.

The entire set of data for this thesis is shown in Appendix B, but for illustration purposes, three bubble sizes are examined more closely in this chapter, representing the the upper, middle, and lower sizes of bubble response acquired. Equalized data for bubbles 470, 342, and 271 μm in radius are shown in Figures 4.7, 4.9, and 4.11, respectively. The raw data for each bubble is displayed in the figure immediately preceding each bubble size's equalized data plot.

Notice in each of Figures 4.6, 4.8, and 4.10, after comparison is made to the subsequent acoustical pressure measurement, that the salient feature of the raw PMT data plot is the bubble resonance peak. Moreover, the responses of the 470- and 271-μm-radius bubbles are very nicely extracted since they reside at frequencies that are well separated from cell-related resonances. However, the bubble with 342-μm radius is close to the strong geometric resonance at 8.63 kHz as scrutiny of the top plot of Figure 4.8 demonstrates. Regardless, the bubble response was successfully extracted in this case.

Conversely, there were instances when the bubble was coupled heavily to a cell-related resonance, where the Wiener filter failed to extract the bubble's response. Two examples of a bubble strongly coupling into a cell resonance are shown in Appendix B, in Figures B.1 and B.15. In the case of the 240-μm-radius bubble of Figure B.1, its frequency response could not clearly enough be recovered from the raw data with the current equalization technique. However, the data does appear to have what would have been a peak near the bubble's predicted resonance frequency. As for the 345-μm-radius bubble of Figure B.15, the measurement had a frequency resolution of 12.5 Hz, so two separate peaks should easily be resolvable. Nevertheless, the bubble follows the higher-Q response of the cell. Still, a parameter fit was performed on this data, resulting in reasonable values for ω_0, Q, and β.

4.3 Bubble Damping in Xanthan Gel

After the damped linear oscillator model was fitted to the equalized data, the total damping coefficient, β, for each bubble was calculated from the fit parameters, ω_0 and Q, as follows (cf. Eqn. 2.50)

$$\beta = \frac{\omega_0}{2Q}. \tag{4.2}$$

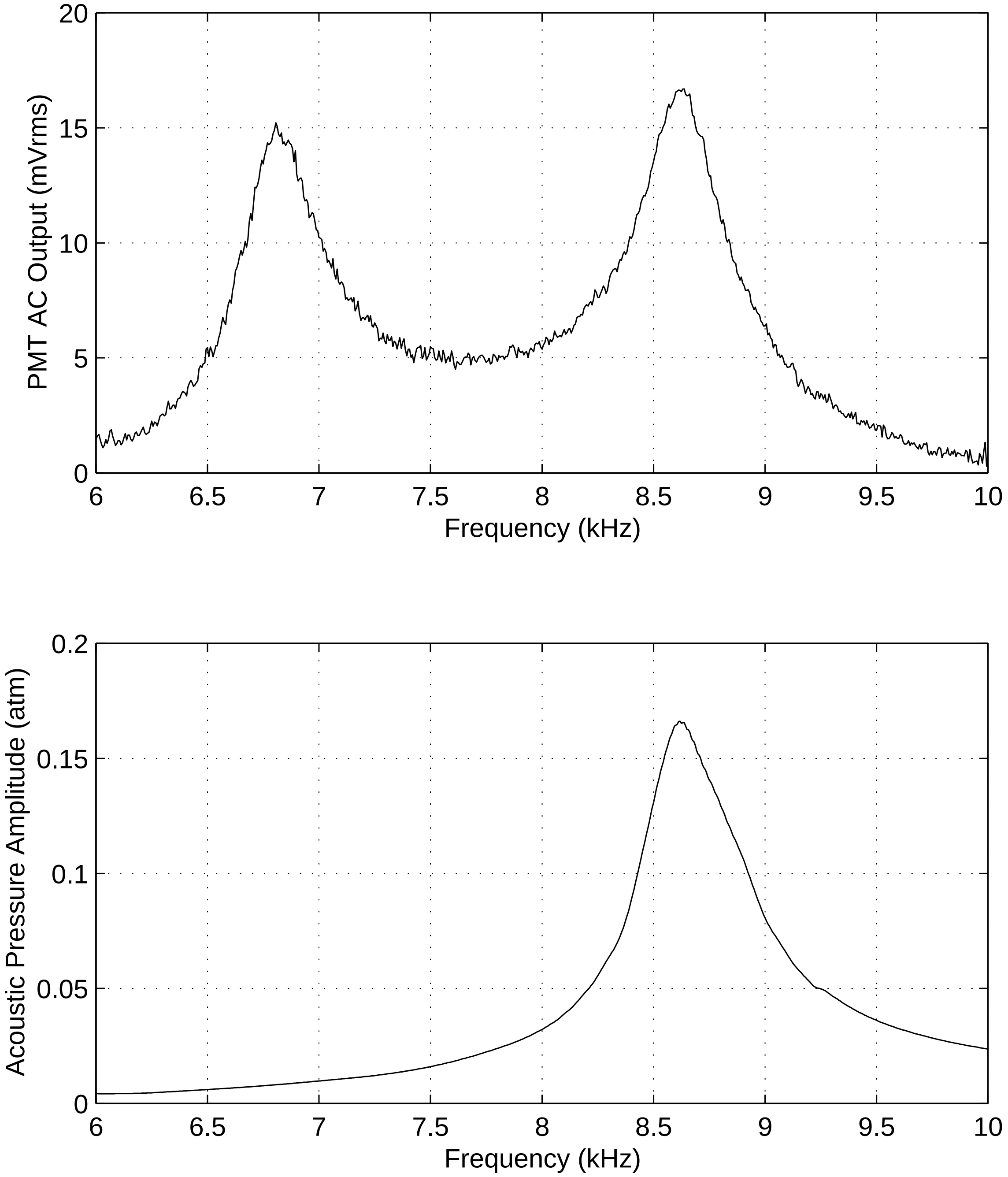

Figure 4.6: The top plot shows the raw PMT output; The bottom plot shows the peak acoustical pressure background of a 470-μm radius bubble.

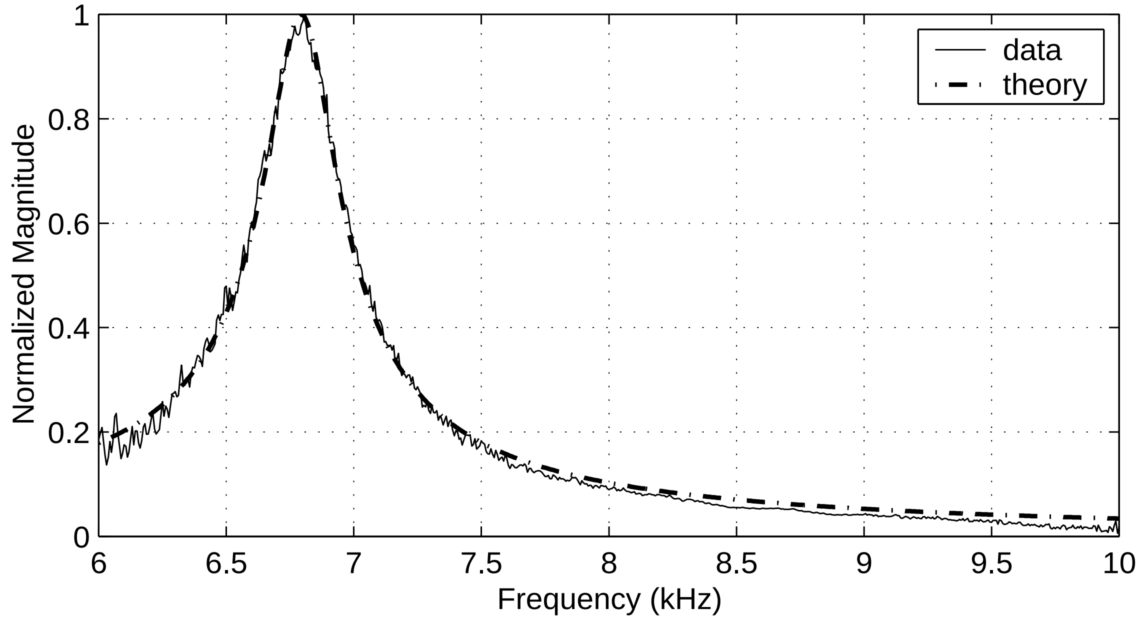

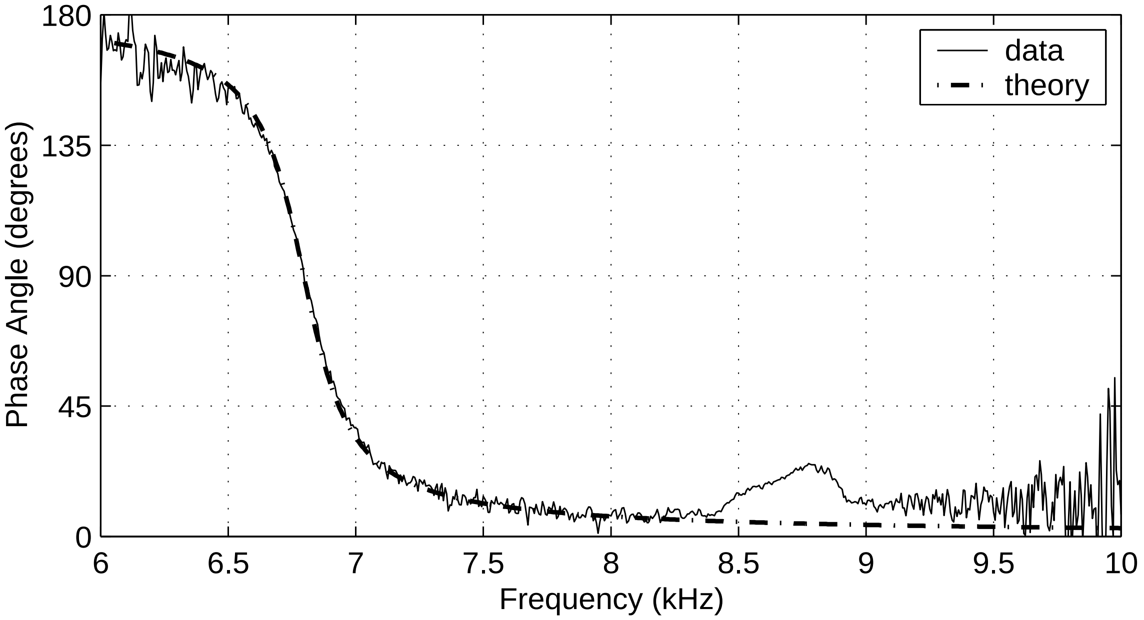

Figure 4.7: Equalized data for a 470-μm radius bubble. The top plot is the normalized magnitude of the bubble response; the bottom plot is the phase. Fit parameters are: $Q_{\text{fit}} = 25.0$; $f_{0,\text{fit}} = 6796$ Hz; $\beta = 854\,\text{sec}^{-1}$. Phase data was shifted +10°. The deviation in the phase plot near 8.6 kHz was caused by a geometric cell resonance.

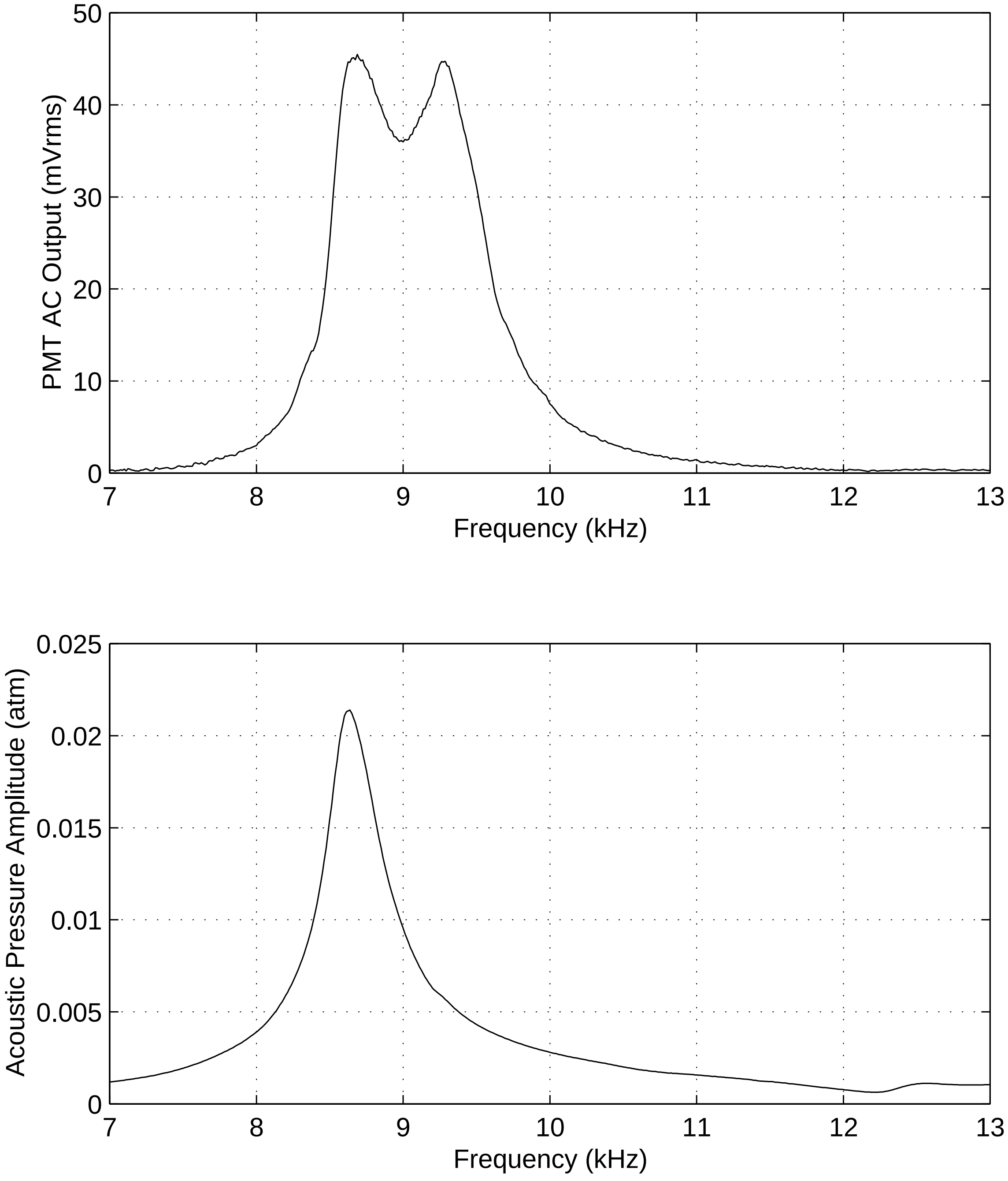

Figure 4.8: The top plot shows the raw PMT output; The bottom plot shows the peak acoustical pressure background of a 342-μm radius bubble.

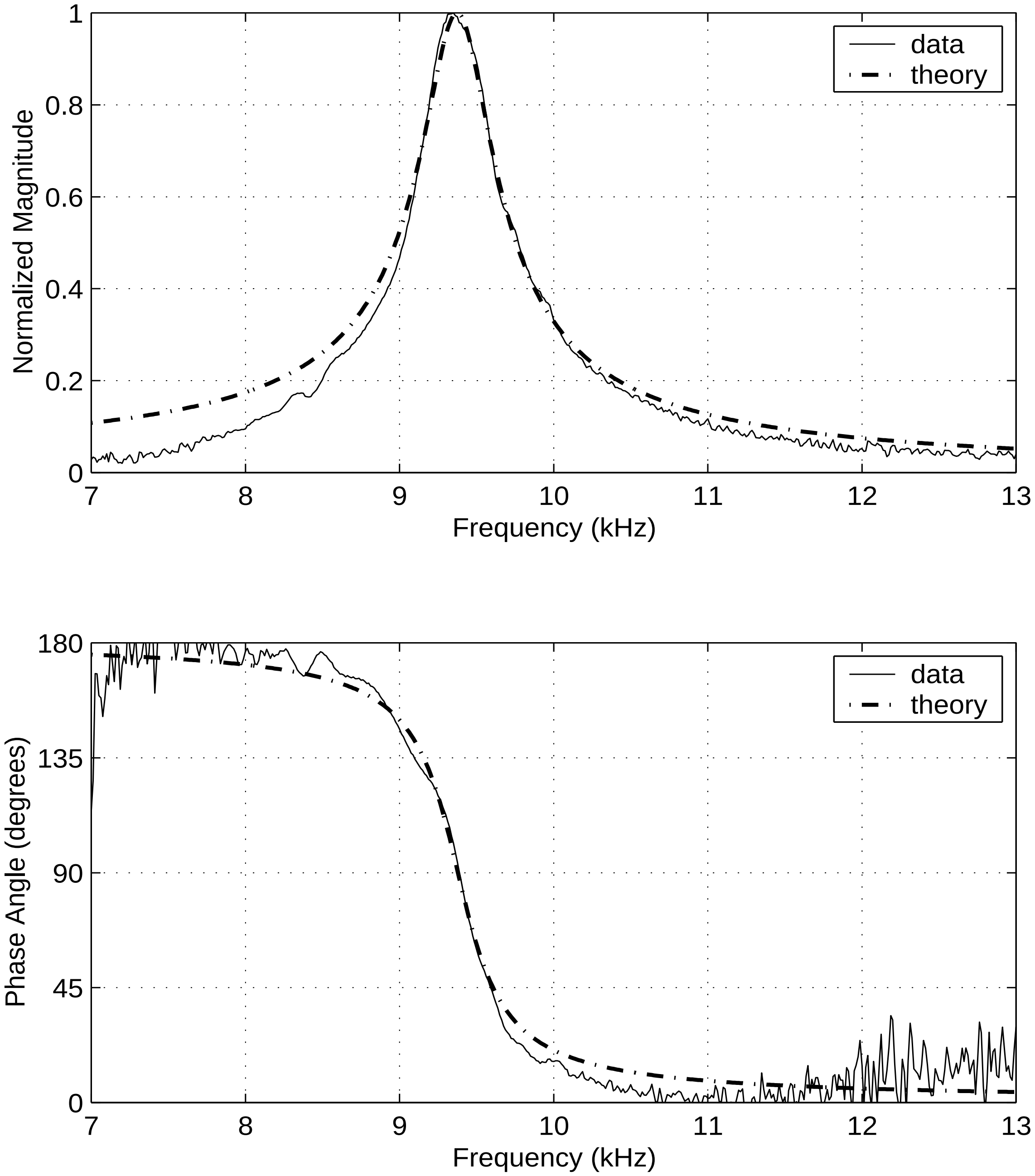

Figure 4.9: Equalized data for a 342-μm radius bubble. The top plot is the normalized magnitude of the bubble response; the bottom plot is the phase. Fit parameters are: $Q_{\mathrm{fit}} = 20.8$; $f_{0,\mathrm{fit}} = 9379$ Hz; $\beta = 1417\ \mathrm{sec}^{-1}$. Phase data was shifted -20°. This data was taken near the geometric cell resonance at 8.6 kHz, which accounts of the deviation in the magnitude plot.

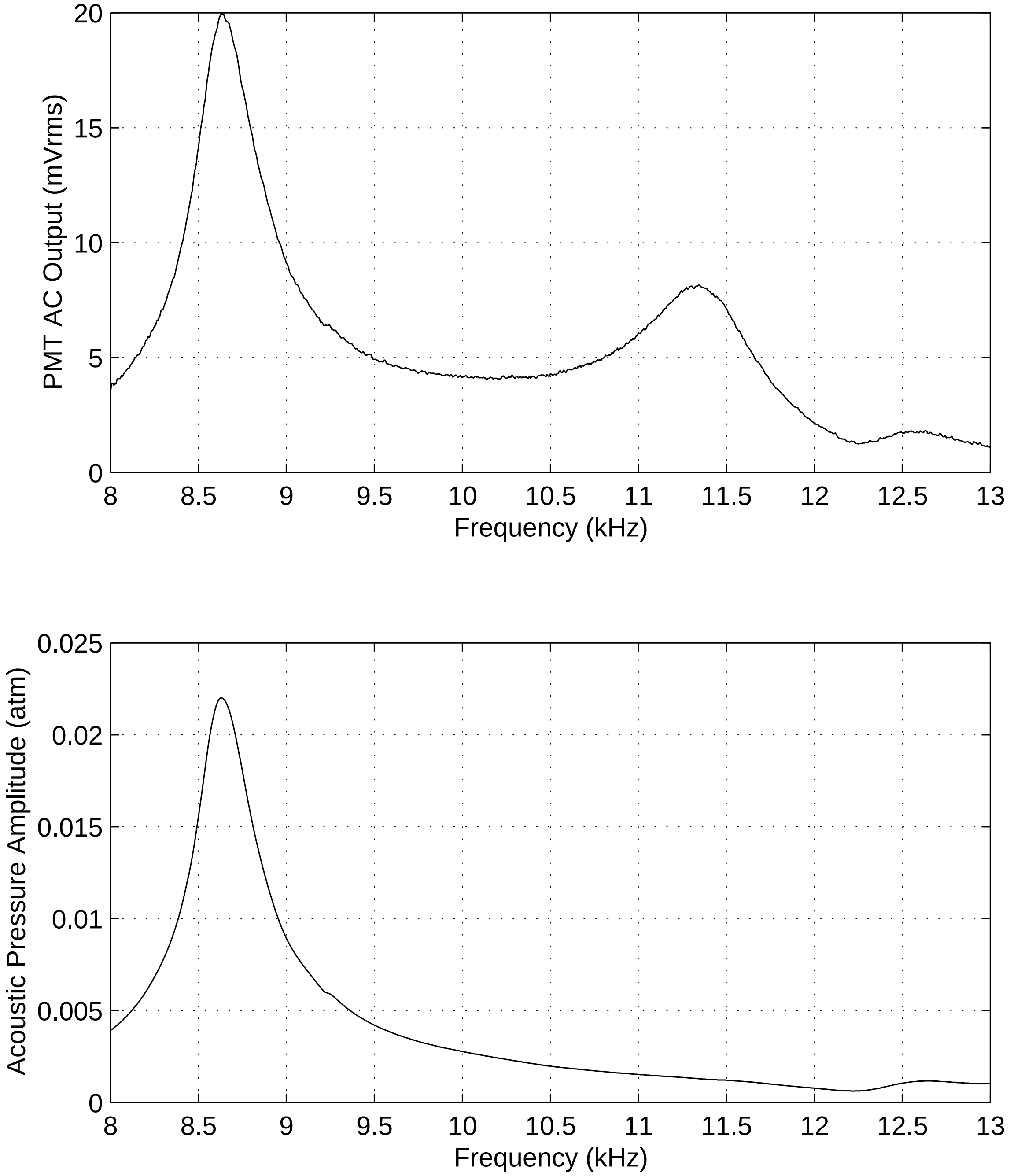

Figure 4.10: The top plot shows the raw PMT output; The bottom plot shows the peak acoustical pressure background of a 271-μm radius bubble.

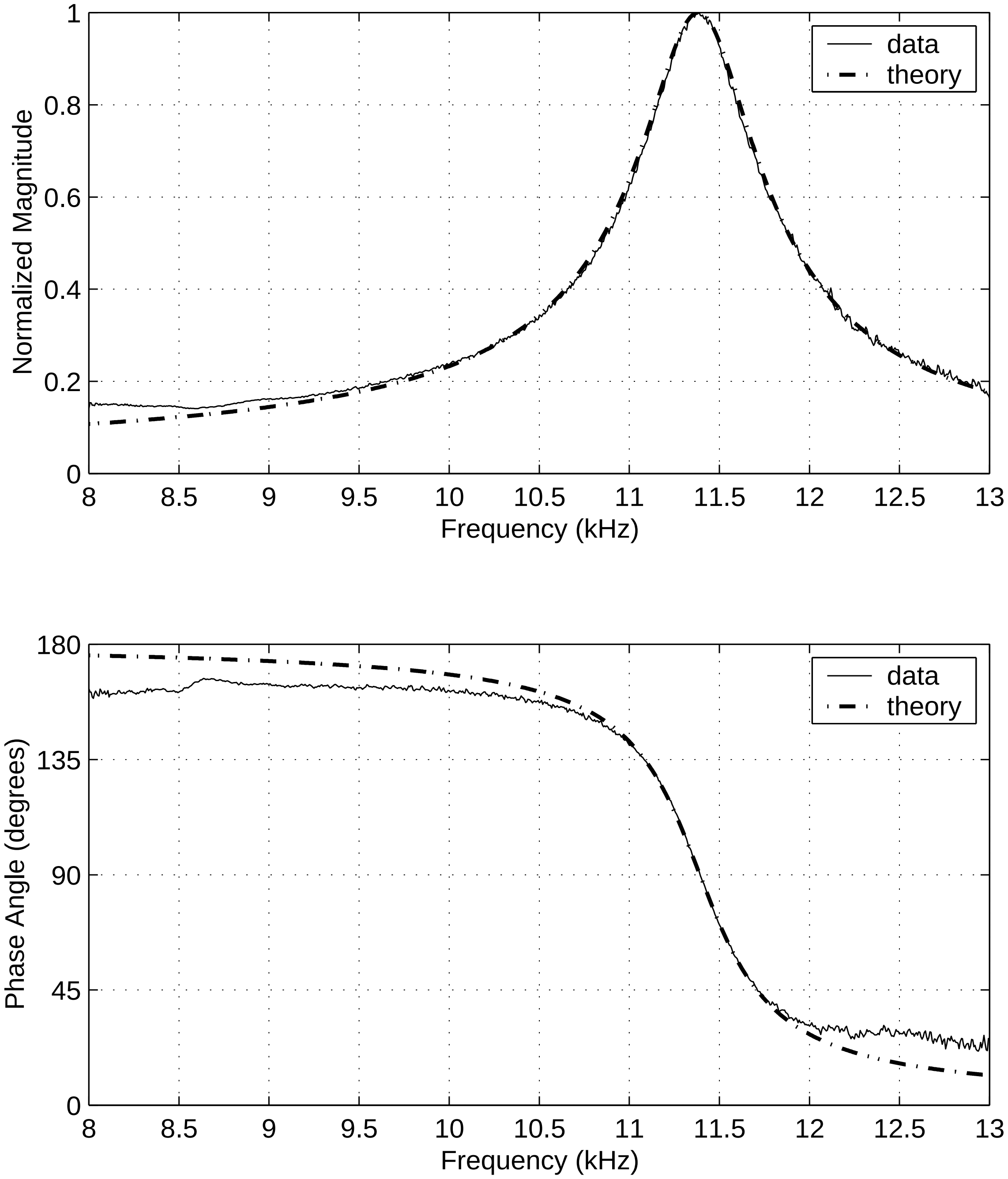

Figure 4.11: Equalized data for a 271-μm radius bubble. The top plot is the normalized magnitude of the bubble response; the bottom plot is the phase. Fit parameters are: $Q_{\text{fit}} = 18.3$; $f_{0,\text{fit}} = 11392$ Hz; $\beta = 1956\,\text{sec}^{-1}$. Phase data was shifted $-7°$.

This is the *dimensional* total damping coefficient at resonance defined in Reference [35].

Recall that one of the goals of this research was to determine whether or not bubbles suspended in Xanthan gel would act as though they were in water when acoustically driven into radial oscillation. In this way, the parameters of *water*, not Xanthan gel, were employed in the bubble damping calculations. Figure 4.12 compares the measured and computed values for the bubble resonance frequency, where the latter was calculated from the expression for the Minnaert frequency, Equation 2.48. Similarly, Figure 4.13 shows the estimated total damping coefficient, derived from the data via Equation 4.2, plotted along with theoretical predictions for the various components of the total damping coefficient of an air bubble in water at an ambient pressure and temperature of 102150 Pa and 23.5°C, respectively. The error bars in Figures 4.12 and 4.13 are based on considerations discussed below in Section 4.4.

There is reasonably good agreement between the data points and the theory in both figures, with possible exception being the damping measurements for the smallest bubbles studied. The gap between 350 and 400 μm radius bubbles is where the strong geometric cell resonance at 8.6 kHz is located. Near this frequency, measurement of a bubble was precluded because the bubble was too strongly coupled to the cell resonance to extract meaningful information about the bubble's response alone. Notwithstanding that gap, the data suggests that the much higher static viscosity of the gel is not manifested in the bubble's dynamic response. This could be true in part because thermal damping normally dominates for bubbles of this size range and in this range of driving frequency, and in part because shear-thinning will lower the gel viscosity as the rate of strain increases. Unfortunately, we are not in a position to quantify the effect of shear-thinning because the gel's rheological response is not known for flows of this type. Regardless, the qualitative consideration of the impact of shear-thinning does suggest behavior consistent with the laboratory observations.

To summarize, the driven, linear dynamical response of 240–470 μm bubbles suspended in a 0.65% concentration Xanthan gum solution is virtually indistinguishable from what one would expect from the same bubbles in water. This is likely to continue to be true for larger bubbles. However, deviations are expected for smaller bubbles owing to the increased importance of viscous damping as R_0 is reduced [35].

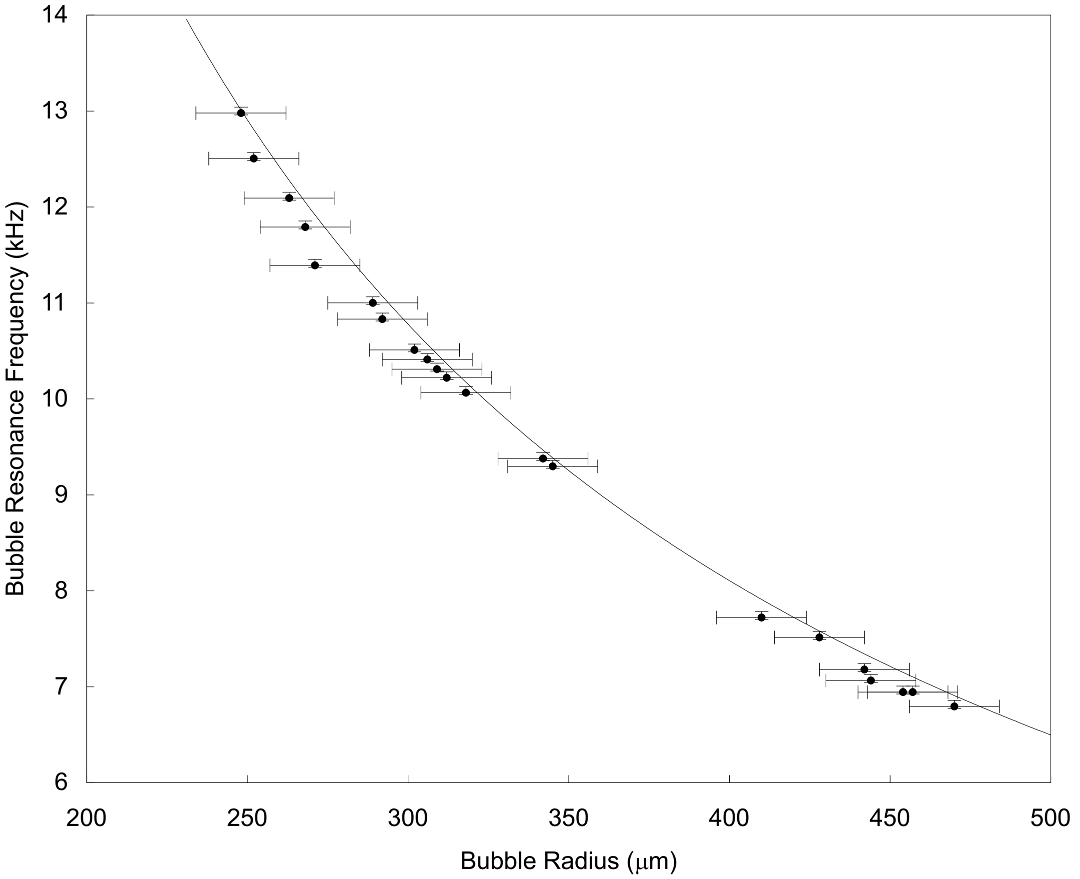

Figure 4.12: Resonance frequency fit parameter plotted over the frequencies predicted by Minnaert's equation for a bubble in water. The x-axis error bars reflect uncertainties in measurement of the bubble radius with the CCD image.

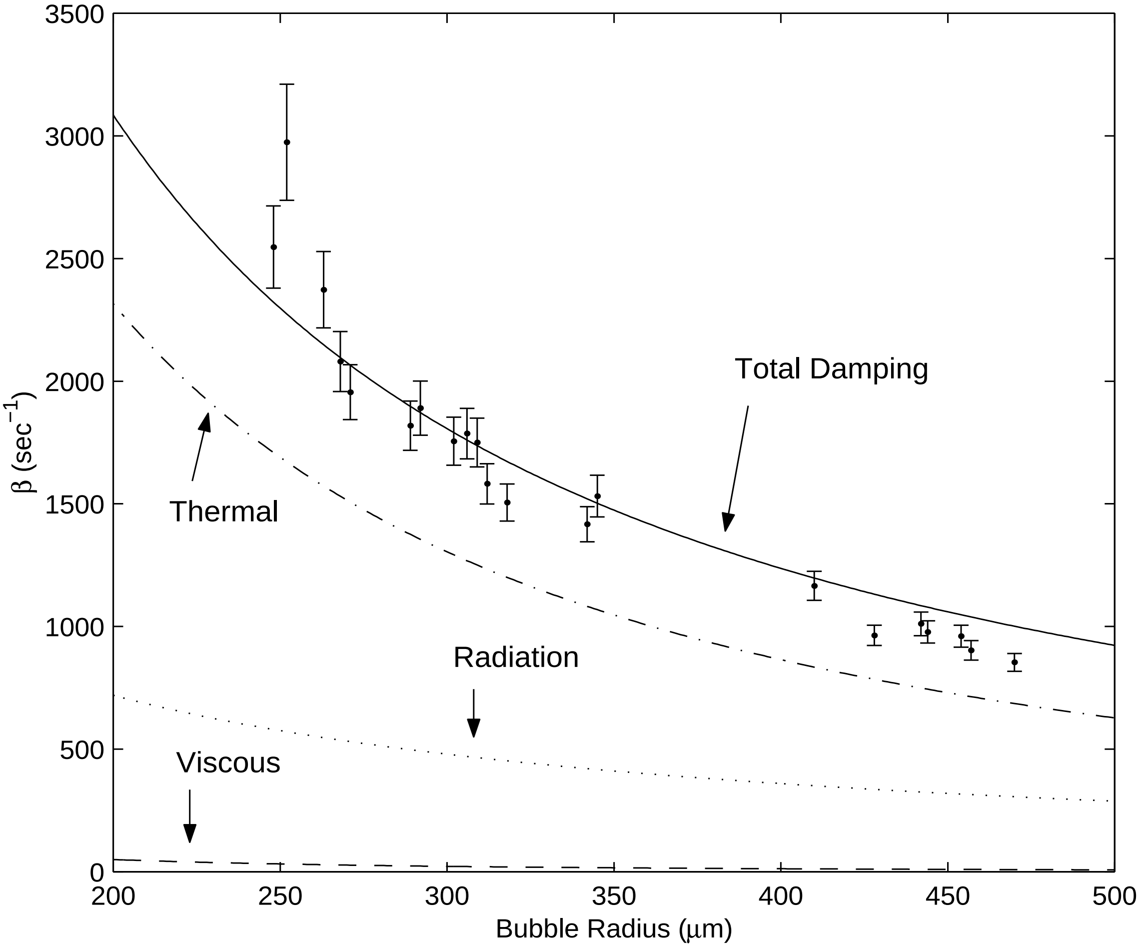

Figure 4.13: Total damping coefficient calculated from fit parameters, f_0 and Q, for a bubble oscillating in Xanthan gel. Total damping is shown divided among its three components: thermal, radiation, and viscous losses. Data is shown with error bars. The bubble damping theory is for a bubble oscillating in water, and calculations correspond to each bubble size being driven at resonance [35].

4.4 Error Analysis

What follows is an estimate of the accuracy and precision error accumulated during the measurement process. There are three descriptions: 1) a measure of the uncertainty in measuring the bubble radius by CCD camera image; 2) a measure of the error of the parameter-fitting process; 3) an estimate of the precision, or repeatability, of the measurement of a bubble's response by optical scattering.

The bubble resonance frequencies in this thesis were calculated with Minnaert's equation for a bubble in *water* [32]:

$$f_0 = \frac{1}{2\pi R_0}\sqrt{\frac{3\gamma P_0}{\rho_l}}. \tag{4.3}$$

There are uncertainties associated with the three physical quantities R_0, P_0, and ρ_l such that:

$$\Delta f_0 = \sqrt{\left(\frac{\partial f_0}{\partial R_0}\Delta R_0\right)^2 + \left(\frac{\partial f_0}{\partial P_0}\Delta P_0\right)^2 + \left(\frac{\partial f_0}{\partial \rho_l}\Delta \rho_l\right)^2}, \tag{4.4}$$

where $\Delta\langle quantity\rangle$ implies the uncertainty of that quantity. Using Equation 4.3, the explicit form of Equation 4.4 can be written as

$$\Delta f_0 = f_0\sqrt{\left(-\frac{\Delta R_0}{R_0}\right)^2 + \left(\frac{\Delta P_0}{2P_0}\right)^2 + \left(-\frac{\Delta \rho_l}{2\rho_l}\right)^2} \tag{4.5}$$

In these experiments, the radius of the bubble was measured directly from an optical image taken with a CCD camera. The bubble was lit from behind by diffuse white light to ensure as much contrast as possible near the bubble edge. So, to measure the size of the bubble with Scion Image, four measurements of the diameter of the bubble were taken manually. The view of the bubble image was zoomed in until the pixels were visible. Then a line was drawn from an arbitrary spot on the edge, across the bubble center, to the opposite edge, where the maximum value for that line length ensured passage through the bubble center. This is true since the diameter is the longest distance between two points on a circle.

The images had a resolution of approximately 5 μm/pixel. An estimate of the error of measurement of the diameter is ±2 pixels at each end of the diameter for a total error of

±20 μm for each diameter measurement, and therefore

$$\Delta R_0 = \sqrt{(\pm 10)^2 + (\pm 10)^2} = 14\ \mu m. \tag{4.6}$$

The other physical parameters were dependent on the temperature, which had a range for all experiments of T = 23.5 ± 0.5°C. This temperature uncertainty corresponds to a sound speed uncertainty in water of c = 1493 ± 1.5 m/s, and a density uncertainty of ρ_l = 997.42 ± 0.12 kg/m^3. There was some uncertainty about the hydrostatic pressure associated with error in the depth the bubble sat in the gel. The bubble moved a maximum of 8 mm in the vertical direction. Estimating that the bubble was submerged 22 ± 4 mm from the surface of the gel gives an error of

$$\rho_{gel} gh = (1034 \text{kg/m}^3)(9.81 \text{m/s})(0.022 \pm 0.004 \text{m}) = 223 \pm 41 \text{ Pa}. \tag{4.7}$$

So, the total equilibrium pressure experienced by the bubble was

$$P_0 = P_\infty + \rho_{gel} gh = 101930^1(+1350, -750) + (223 \pm 41) = 102153(+1391, -791) \text{ Pa}. \tag{4.8}$$

Finally, substituting the uncertainty values for R_0, P_0, and ρ_l into Equation 4.5 results in

$$\frac{\Delta f_0}{f_0} = \sqrt{\left(-\frac{\Delta R_0}{R_0}\right)^2 + (7 \times 10^{-3})^2 + (-6 \times 10^{-5})^2} \tag{4.9}$$

The uncertainty due to the radius falls in the range 5.8–3.0×10^{-2} (5.8–3.0%), corresponding to the range of working bubble sizes 240–470 μm. As you can see, the error is dominated by the inaccuracy of the bubble radius measurement. Figure 4.14 shows a plot of Equation 4.9. Notice there is more error at the smaller bubble radii. This makes sense because the smaller the bubble gets, the closer the fixed pixel size (5 μm/pixel) of the bubble image gets to the bubble radius size.

---

[1] The mean value and fluctuations for the atmospheric pressure, P_∞, were taken from the National Climatic Data Center for the city of Boston, Massachusetts, USA, during the month of November 2001 (www.ncdc.noaa.gov).

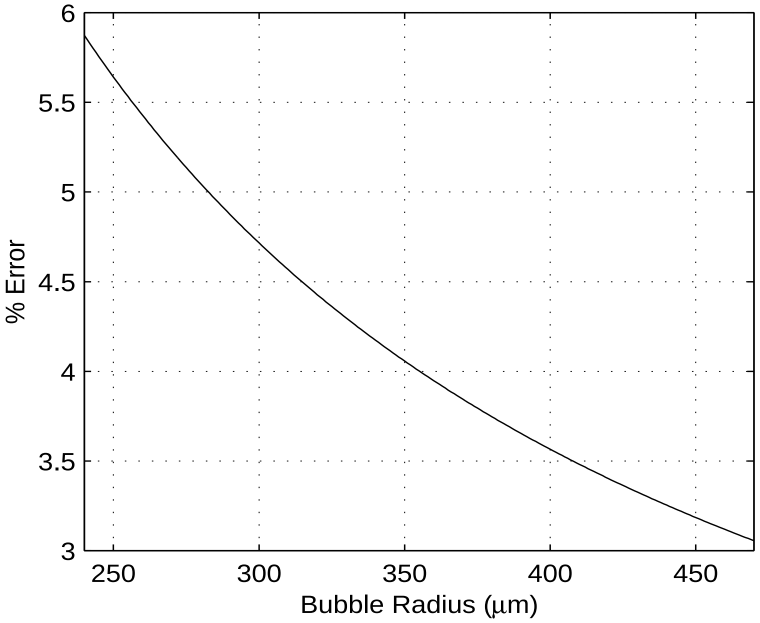

Figure 4.14: Error in the calculated resonance frequency due to inaccuracies of the bubble radius measurement.

Now, we describe the error inherent in the parameter fitting process, which entails an estimate of error of both the resonance frequency and Quality factor. The resonance frequency fit to the bubble magnitude data was compared to the frequency of the peak in the data and a maximum deviation of the parameter from the data was estimated. The resonance frequency fit parameter error ranged from a +62 Hz to a −20 Hz deviation from the resonance frequency of the actual bubble response magnitude data, corresponding to +0.9% and −0.3% at the lowest bubble resonance frequency measured.

An ad hoc approach was taken to the determination of the accuracy and precision of the Q extracted from the bubble frequency response. Only the magnitude function was used to fit the parameters f_0 and Q. As a check on the accuracy of the Q fit to the magnitude data, a measure of the accuracy of Q can be extracted from the phase data as well, using Equation 2.23:

$$Q = \frac{\omega_0}{2}\left(\frac{d\delta}{d\omega}\right)_{\omega=\omega_0}. \tag{4.10}$$

A least-square-error fit was performed on the phase data for a frequency range encompassing the magnitude-fit resonance frequency, $f_0 \pm 200$ Hz. For this calculation, the magnitude fit value of the resonance frequency was held constant, and only the fit parameter Q was varied. By comparing the values determined by the phase fit to the values calculated from the magnitude fit, a range of maximum accuracy error was determined for Q of $+2.1$ and -1.0, corresponding to $+15.9\%$ and -7.8%. This is manifested through the damping coefficient in the error bars of Figures 4.12 and 4.13.

The precision of the fit of the parameter Q is determined from Equation 4.34 in [12], but using the notation of this thesis (see Equation 4.1):

$$\sigma = \sqrt{\frac{E_{total} = \sum_{f=f_-}^{f_+} (T(f) - D(f))^2}{\nu}}, \tag{4.11}$$

where ν is the degrees of freedom of the fit, $\nu = N - (m+1)$, N is the number of points in the data set, and m is the order of polynomial being fit to the data. In our case, $N = 801$ and $m = 2$, so $\nu = 798$. For a dimensional quantity, Equation 4.11 results in an absolute precision error in that quantity. For our purposes, we are interested in the *relative* error. Because the quantities of interest, f_0, Q, and β, are all properties of the system near its resonance, we can "normalize", in an ad hoc fashion, the absolute error of the fit, given by σ, to the value at resonance. However, the quantities, $T(f)$ and $D(f)$, in Equation 4.11 are already normalized to the peak at resonance, so the calculated value for σ is already the error of the fit, relative to the value at resonance. Therefore, we plot the precision error or standard error of the fit in Figure 4.15. As you can see, the maximum value for the data points lies near 0.11%.

The precision to which the resonance frequency parameter is fit to the data depends on the resolution of the frequency response calculation. The signal analyzer computed 800 points for every frequency measurement, so the precision was set by the width of the frequency band of the measurement. The largest-bandwidth measurement had a bandwidth of

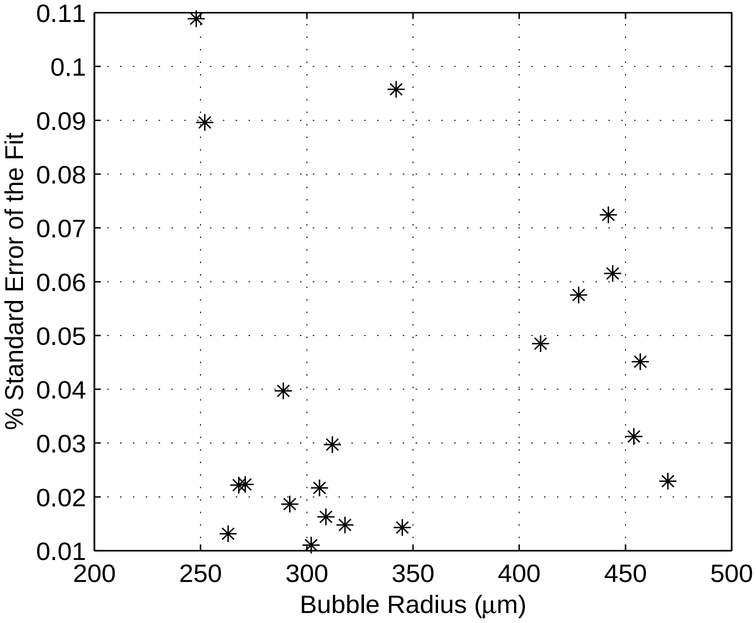

Figure 4.15: Precision error in Q due to fitting parameters to data at each bubble radius. This is a plot of Equation 4.11 for each data point plotted in Figures 4.12 and 4.13.

10 kHz, which gives a worst-case frequency resolution of $\Delta f = 10000/800 = 12.5$ Hz/point. The lowest measured resonance frequency would then have the worst-case precision error for f_0 of $12.5/6796 = 0.18\%$.

It is clear then, that the 0.11% and 0.18% precision errors in Q and f_0, respectively, are much less than the accuracy errors for each quantity. The largest accuracy error for Q was due to the inaccuracy of the damped linear oscillator model fit to the data and had a range of $+15.9, -7.8\%$. The largest accuracy error for f_0 was due to the uncertainty in the bubble radius measurement and had a worst-case value of 5.8%.

We can also estimate the accuracy of the damping coefficient calculation. Since the damping coefficient, β, is dependent only on f_0 and Q, we write

$$\Delta\beta = \sqrt{\left(\frac{\partial\beta}{\partial f_0}\Delta f_0\right)^2 + \left(\frac{\partial\beta}{\partial Q}\Delta Q\right)^2}. \tag{4.12}$$

Using the explicit form for the damping coefficient, $\beta = \omega_0/2Q$, we can write the explicit form of the error as

$$\frac{\Delta\beta}{\beta} = \sqrt{\left(\frac{\Delta f_0}{2f_0}\right)^2 + \left(-\frac{\Delta Q}{2Q}\right)^2}. \tag{4.13}$$

The largest uncertainty in Q and f_0 is $\Delta Q = 2.1$, and $\Delta f_0 = 62$ Hz, respectively. Use of the largest uncertainty value for each parameter results in the accuracy error values plotted in Figure 4.16 for each data point shown in Figures 4.12 and 4.13.

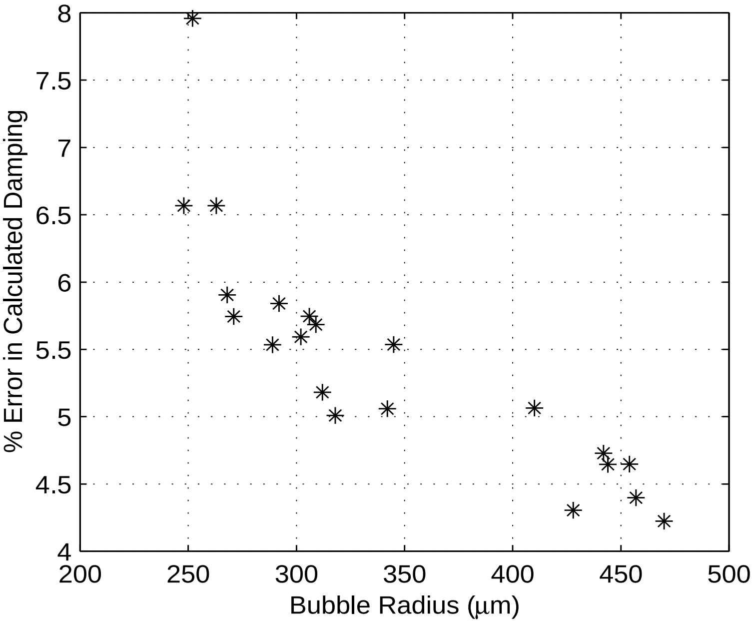

Figure 4.16: Accuracy error of total damping coefficient, β.

Because measurements were made using three different systems, two optical, one acoustical, a separate description of the precision of each of those systems follows. The optical imaging system led to an absolute precision in the CCD images of ±2 pixels (±10 μm) at the bubble edge depending on the clarity of the given batch of gel. The acoustical system measurements of the pressure field in the cell contained a 1% variation in amplitude between consecutive measurements. No physical parameters, such as temperature or the height of the gel in the cell, changed over the course of the measurement. The only aspect that did change over the course of the measurement was the bubble's motion and dissolution in the gel, which affected the optical scattering apparatus.

As soon as the bubble was injected into the gel for measurement, it began shrinking. A typical observed dissolution rate was 3 μm per minute in bubble radius. The longest optical scattering measurement took 8 seconds for 50 averages and a bandwidth of 5 kHz. So, over the course of one measurement, the bubble size did not change. Repeating the measurement at the same bubble radius was limited to observing the peak on the DSA display because saving a measurement as a data set took additional time to store on computer disk via GPIB transfer. That extra time was enough to change the bubble size so that the subsequent measurement was not a repeat of the initial measurement. As such, an estimate of the measurement precision is based on many qualitative experimental observations of 2 measurements of 50 averages. As an example, a bubble with a resonance peak at 10 kHz would not experience a shift in frequency in the peak of more than 50 Hz over 2 consecutive measurements of 50 averages. This corresponds to a precision of 0.5%. As a conservative estimate, the optical scattering measurement had a precision error of less than 1%.

Chapter 5

Summary and Conclusions

The research performed for this thesis had two main goals. One goal was to measure the linear frequency-dependent response of a bubble below, through, and above its resonance frequency using a non-invasive optical laser scattering technique. By comparing the resulting frequency traces to those for a water bubble, information about the linear dynamics of a bubble in the gel could be obtained.

The other goal of the research was to determine if a bubble suspended in a gel made from the polymer Xanthan gum would undergo acoustically forced radial oscillations such that it mimicked a bubble oscillating in water. In this way, the gel could be used for fabricating stable artificial bubble clouds that have acoustical and physical properties similar to those of bubble clouds in water.

5.1 Summary of Experimental Results and Comparison with Model

In its raw form, the optically-measured, frequency-dependent bubble response was in fact a convolution of the bubble's frequency response and the frequency-dependent driving pressure field (which includes both the modes of the cell as well as electromechanical resonances). A subsequent acoustical measurement of the test cell's frequency-dependent pressure field at the spatial location of the bubble (after its removal) allowed equalization of the cell-related effects on the bubble's linear dynamic response, provided the bubble was not closely coupled to a cell-related resonance. In those cases, meaningful information about the bubble's frequency response could not be extracted with the equalization methods employed here. Leighton has alluded to the problems such as this that arise when the assumption of a free field environment around a single bubble is not valid [26].

By comparing the bubble's frequency response to a damped linear oscillator model, values for the resonance frequency and Quality factor were educed. These parameters were used to calculate a dimensional damping coefficient, which was in turn compared to a theory for the total damping of linearly oscillating bubbles. The range of bubble sizes measured for this thesis encompassed 240–470 μm radius bubbles, corresponding to frequencies in the range 6–14 kHz, and an optical ka range of 2383–4667. Total damping coefficients computed from fit parameters of measured bubbles were in the range 854–2976 sec^{-1}.

In general, there is good quantitative agreement between the theory for a bubble in water and the data taken with a bubble suspended in Xanthan gel, both in the resonance frequency and damping plots. This suggests that the increased static viscosity of the gel is not an important contributing factor to the linear dynamics of bubbles in this range of sizes and over this range of driving frequencies.

5.2 Conclusions

Both goals of this project were achieved. The Xanthan gel successfully suspended a bubble a duration in time long enough to perform measurements through the bubble's resonance of the bubble's frequency-dependent linear radial response to acoustical excitation. Similarly, the acoustically driven gel bubble responded as though the added static viscoelasticity of the gel was unimportant and did not impede bubble oscillation any more than does water. As such, the bubble appeared as though it was oscillating in water over the range of sizes and frequencies utilized.

5.3 Recommendations for Future Work

Here are a few recommendations to be made for future work that could improve on the present experiment.

The few data points at the smaller bubble radii suggest that if measurement of even smaller sizes could be resolved, bubbles would begin to experience viscous damping effects in excess of that provided by water. Using a calibrated photomultiplier tube would serve as a check on the CCD-acquired image as to exactly what bubble size was being observed. (The CCD image is not sufficiently well resolved for very small bubbles.)

The acoustic test cell itself was not without fault. The resonances it contained proved more hindering than expected. If this experiment could be repeated in a container without any resonances stronger than the bubble itself, the frequency range of data collected could be increased. However, if the containing volume gets too large, optical imaging will become impossible as the gel is not completely transparent. The use of an optical fiber bundle to collect the image and scattered light might help.

The Xanthan gel itself diffused a lot of light throughout the cell because of the inhomogeneities caused by the polymer chains. If this could be improved by, say, a better mixing method, the background light level could be significantly reduced. Perhaps use could be made of a different, more transparent, viscoelastic material that retained physical properties close to those of water.

When these issues are sorted out, more interesting bubble experiments could also be performed, as for example, determination of the interaction of two or more acoustically driven bubbles placed near each other in the gel. Another problem of interest is the *nonlinear* response of bubbles to larger amplitude forcing. This would require a fully calibrated scattering apparatus as well as a pre-equalized pressure field, for the simple application of the filter described in Section 3.8.2 will no longer serve to extract the bubble response.

Appendix A

Mie Theory

These are the scattering-angle dependent amplitude functions mentioned in Chapter 2 as given in van de Hulst [44]. Mie's theory assumes a dielectric sphere of refractive index m_1 enveloped by a medium with refractive index m_2, where a spatially-plane, electromagnetic wave of known polarization is incident upon the sphere. The relative refractive index, which is defined as

$$m = \frac{m_1}{m_2}, \tag{A.1}$$

is the index of the sphere with respect to the surrounding medium and can be complex to account for absorption of light. The scattering angle is measured from the forward direction, which is defined as the direction of propagation of the incident light.

The scattering-angle dependent amplitude functions are given by

$$S_1(\theta) = \sum_{n=1}^{\infty} \frac{2n+1}{n(n+1)} \left\{ a_n \pi_n(\cos\theta) + b_n \tau_n(\cos\theta) \right\}, \tag{A.2}$$

$$S_2(\theta) = \sum_{n=1}^{\infty} \frac{2n+1}{n(n+1)} \left\{ b_n \pi_n(\cos\theta) + a_n \tau_n(\cos\theta) \right\}. \tag{A.3}$$

The coefficients a_n and b_n are the result of matching boundary conditions at the two media's interface and are given by

$$a_n = \frac{\psi_n'(y)\psi_n(x) - m\psi_n(y)\psi_n'(x)}{\psi_n'(y)\zeta_n(x) - m\psi_n(y)\zeta_n'(x)}, \tag{A.4}$$

$$b_n = \frac{m\psi'_n(y)\psi_n(x) - \psi_n(y)\psi'_n(x)}{m\psi'_n(y)\zeta_n(x) - \psi_n(y)\zeta'_n(x)}, \tag{A.5}$$

where primes denote differentiation with respect to its argument and $\psi_n(z)$ and $\zeta_n(z)$ are Ricatti-Bessel functions derived from spherical Bessel functions $j_n(z)$ and $h_n^{(2)}$ or cylindrical Bessel functions $J_n(z)$ and $H_n^{(2)}$as follows

$$\psi_n(z) = zj_n(z) = (\pi z/2)^{1/2} J_{n+1/2}(z), \tag{A.6}$$

$$\chi_n(z) = -zn_n(z) = -(\pi z/2)^{1/2} N_{n+1/2}(z), \tag{A.7}$$

$$\zeta_n(z) = zh_n^{(2)}(z) = -(\pi z/2)^{1/2} H_{n+1/2}^{(2)}(z), \tag{A.8}$$

having used the relationships

$$H_n^{(2)}(z) = J_n(z) - iN_n(z), \tag{A.9}$$

$$\zeta_n(z) = \psi_n(z) + i\chi_n(z). \tag{A.10}$$

The arguments are given by

$$x = ka = \frac{2\pi a}{\lambda}, \tag{A.11}$$

$$y = mka, \tag{A.12}$$

where a is bubble radius and λ is the wavelength of incident light. The angular functions are in terms of 1st order Legendre functions

$$\pi_n(\cos\theta) = \frac{P_n^1(\cos\theta)}{\sin\theta}, \tag{A.13}$$

$$\tau_n(\cos\theta) = \frac{d}{d\theta} P_n^1(\cos\theta). \tag{A.14}$$

All Mie curves in this work were calculated by Warren Wiscombe's MIEV0 program [47] in FORTRAN 77.

Appendix B

Range of Bubble Sizes

This Appendix contains data for the range of bubble sizes to which the damped linear oscillator model was compared. The values of the damping coefficient calculated from these plots were used for comparison to Prosperetti's theory outlined in Section 2.4.

The resonance frequency and quality factor were fit by a least squares error method outlined in Section 4.2. From these parameters the total damping coefficient was computed. The total dimensional damping coefficient evaluated at resonance is given by Equation 2.50:

$$\beta = \frac{\omega_0}{2Q}, \tag{B.1}$$

or in terms of the fit parameters listed below each plot

$$\beta = \frac{\pi f_{0,fit}}{Q_{fit}}. \tag{B.2}$$

Because there was some error associated with data synthesis using the signal analyzer, the magnitude and phase of each data set lay within a range of values. However, the normalized magnitude response was used, so that its absolute error is unimportant. Nevertheless, there was some uncertainty with the phase that has been corrected in the following plots. See Section 4.4 for the exact range of absolute phase encompassed in making measurements with the signal analyzer. Some plots fell outside this error bound, but were shifted anyway to more directly compare to the damped linear oscillator theory. In any case, the amount each plot was shifted is listed in the plot's caption. Table B.1 below collects all data points used in this thesis, including the bubbles featured in Chapter 4.

Table B.1: **Bubble Data Sizes and Fit Parameters**

Radius (μm)	Q_{fit}	$f_{0,\text{fit}}$ (Hz)	β (sec^{-1})
248	16.0	12979	2548
252	13.2	12505	2976
263	16.0	12092	2374
268	17.8	11792	2081
271	18.3	11392	1956
289	19.0	11001	1819
292	18.0	10832	1891
302	18.8	10510	1756
306	18.3	10411	1787
309	18.5	10310	1751
312	20.3	10220	1582
318	21.0	10065	1506
342	20.8	9379	1417
345	19.0	9297	1532
410	20.8	7722	1166
428	24.5	7515	964
442	22.3	7179	1011
444	22.7	7066	978
454	22.7	6945	961
457	24.0	6945	903
470	25.0	6796	854

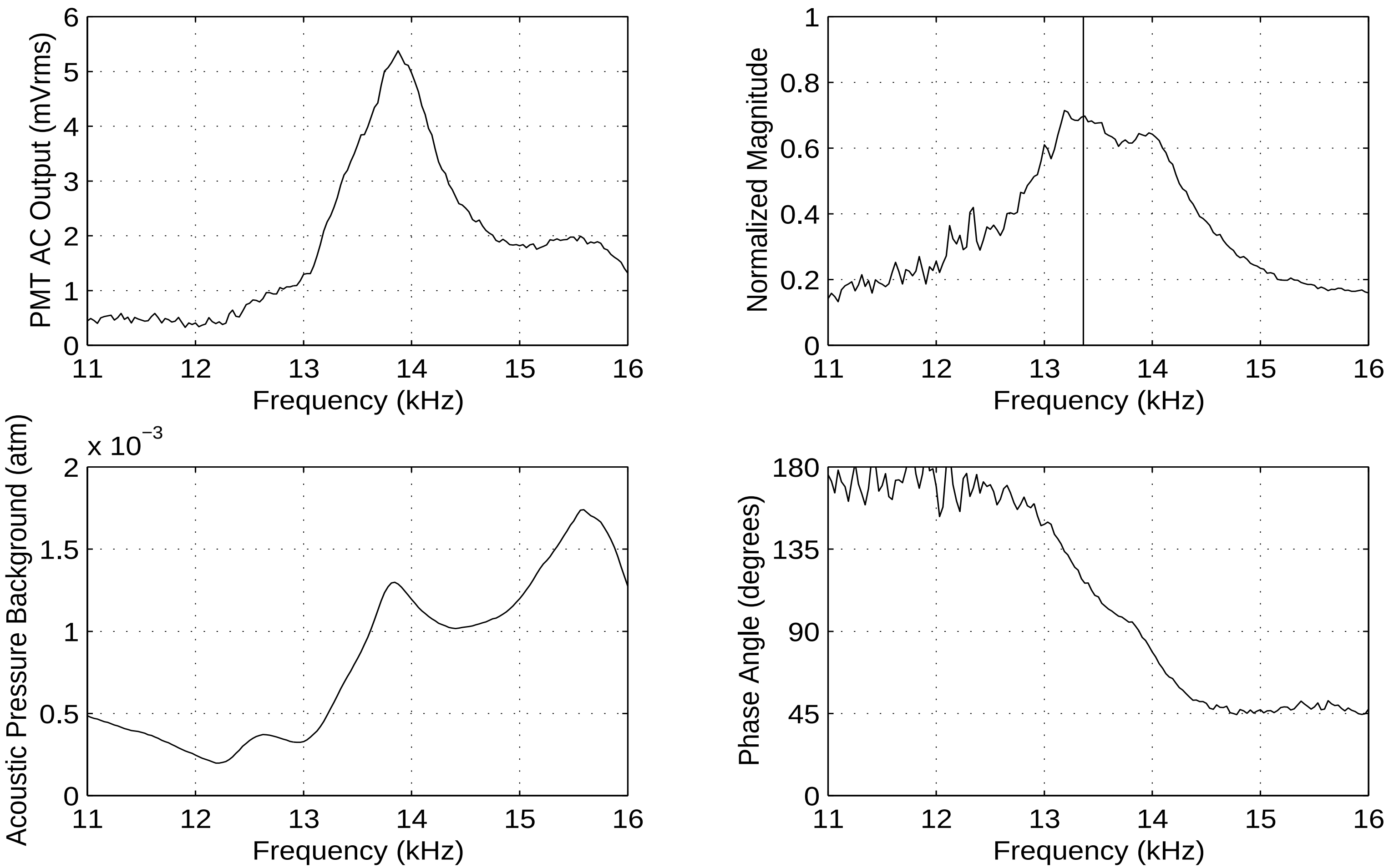

Figure B.1: A 240-μm radius bubble. Bubble coupled to geometric cell resonance. Using current equalization method, a clean bubble response was not recovered. Vertical line shows prediction of bubble resonance by Minnaert's equation.

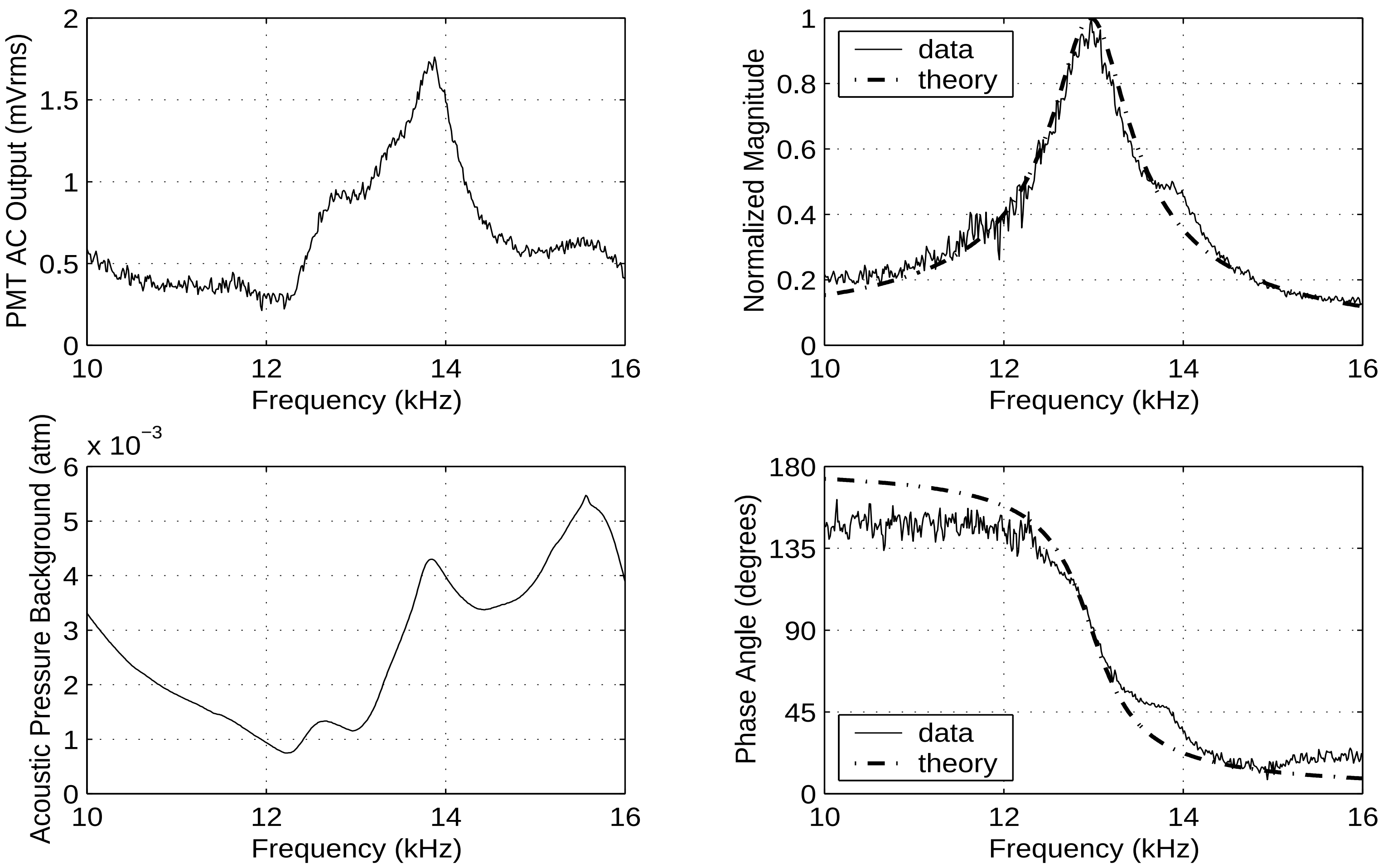

Figure B.2: A 248-μm radius bubble. Fit parameters are: $Q_{\text{fit}} = 16.0$; $f_{0,\text{fit}} = 12979$ Hz; $\beta = 2548\ \text{sec}^{-1}$. Phase data was shifted $-16°$.

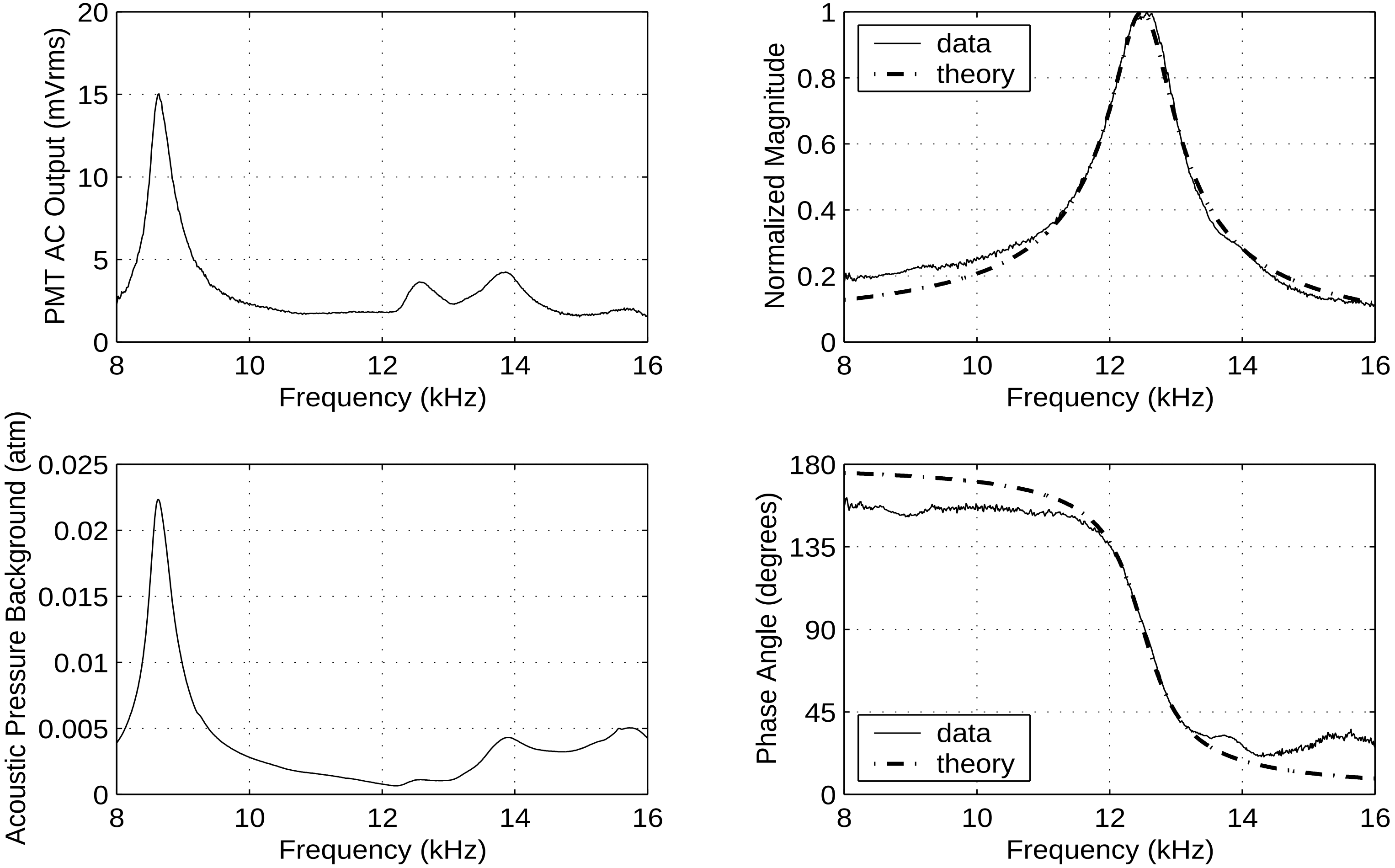

Figure B.3: A 252-μm radius bubble. Fit parameters are: $Q_{\text{fit}} = 13.2$; $f_{0,\text{fit}} = 12505$ Hz; $\beta = 2976\ \text{sec}^{-1}$. Phase data was shifted $-15°$.

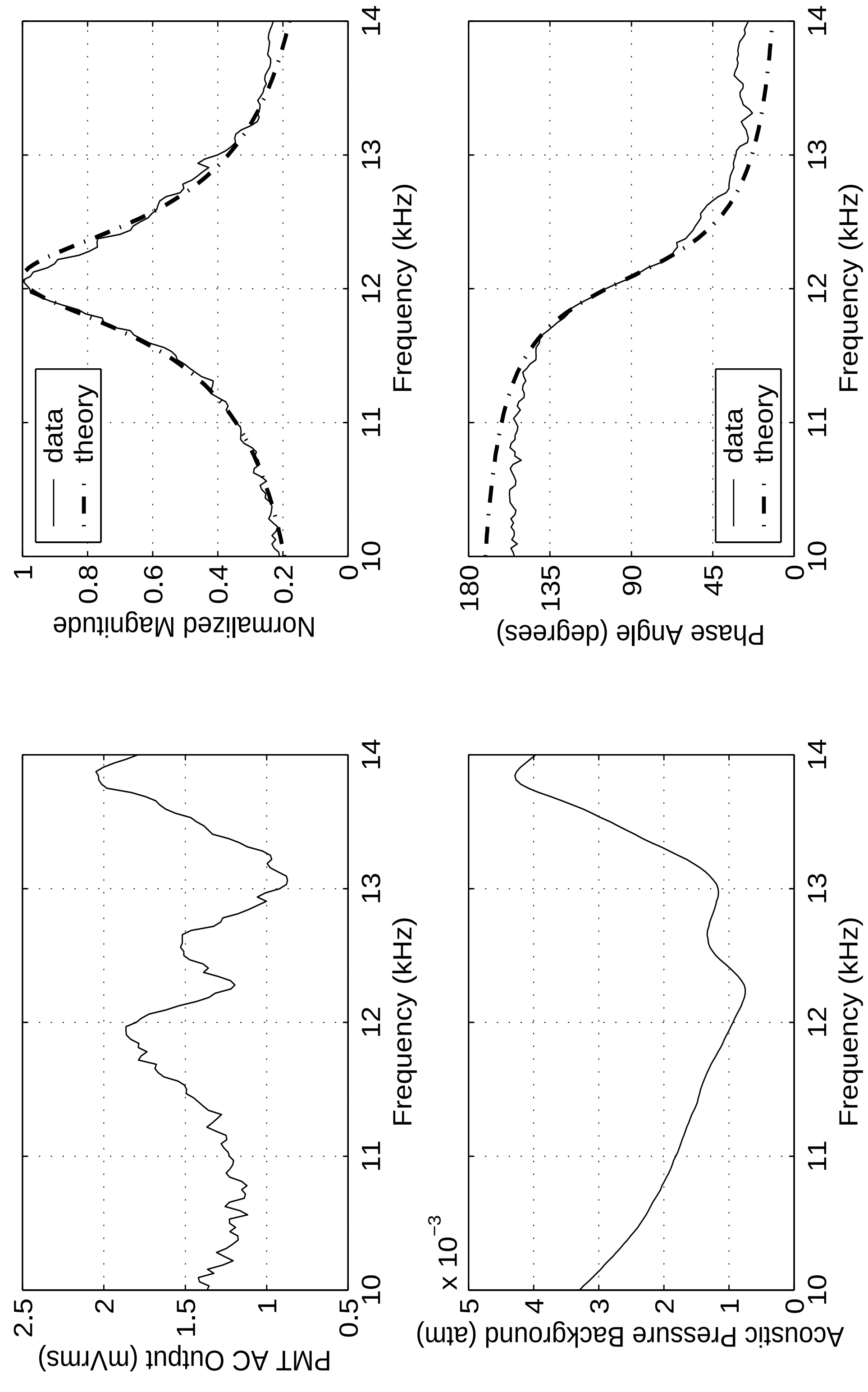

Figure B.4: A 263-μm radius bubble. Fit parameters are: $Q_{\mathrm{fit}} = 16.0$; $f_{0,\mathrm{fit}} = 12092$ Hz; $\beta = 2374\ \mathrm{sec}^{-1}$. Phase data was shifted $-9°$.

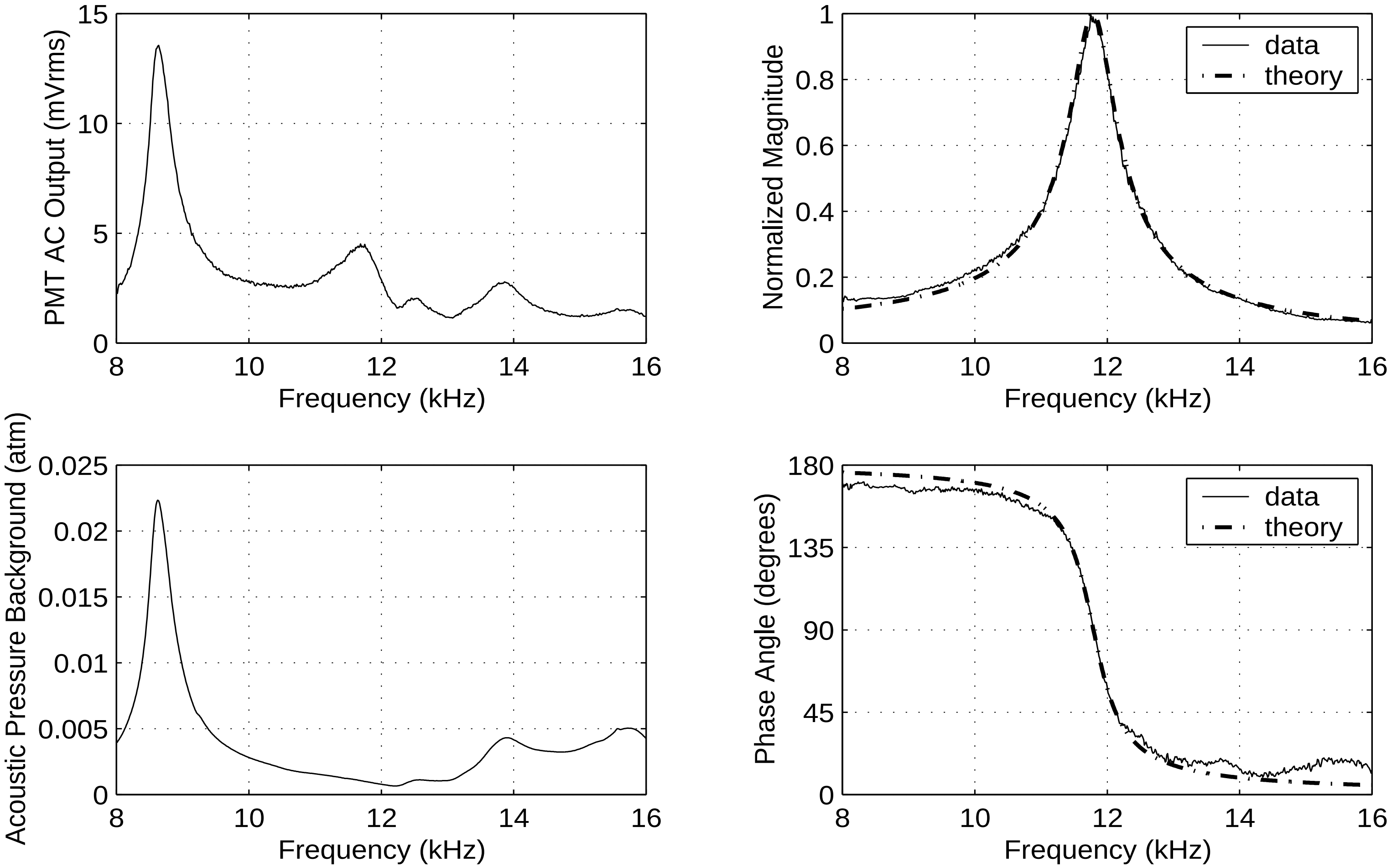

Figure B.5: A 268-μm radius bubble. Fit parameters are: $Q_{\text{fit}} = 17.8$; $f_{0,\text{fit}} = 11792$ Hz; $\beta = 2081$ sec^{-1}. Phase data was shifted $-15°$.

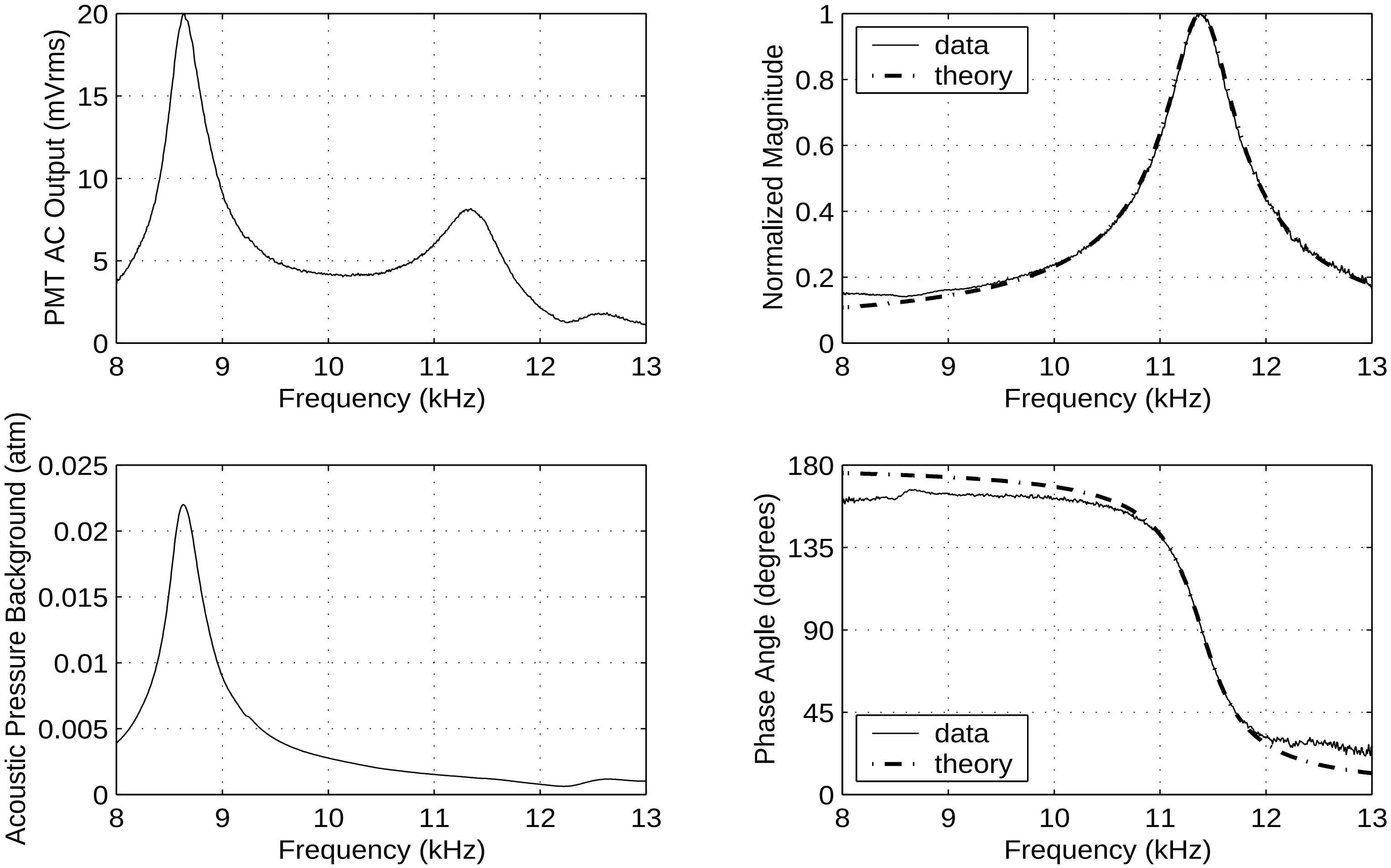

Figure B.6: A 271-μm radius bubble. Fit parameters are: $Q_{\rm fit} = 18.3$; $f_{0,\rm fit} = 11392$ Hz; $\beta = 1956\ \mathrm{sec}^{-1}$. Phase data was shifted $-7°$.

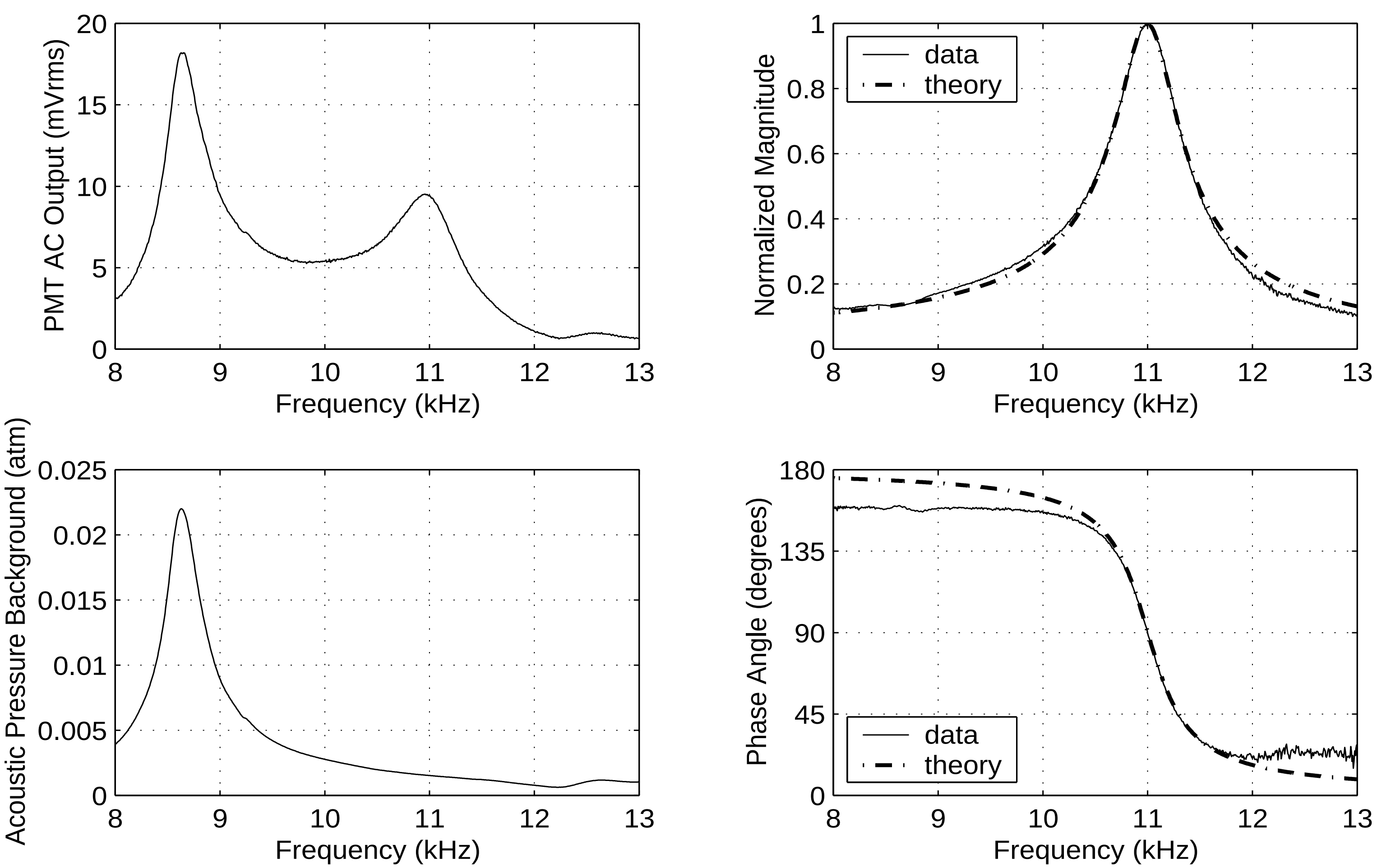

Figure B.7: A 289-μm radius bubble. Fit parameters are: $Q_{\rm fit} = 19.0$; $f_{0,\rm fit} = 11001$ Hz; $\beta = 1819\ {\rm sec}^{-1}$. Phase data was shifted $-9°$.

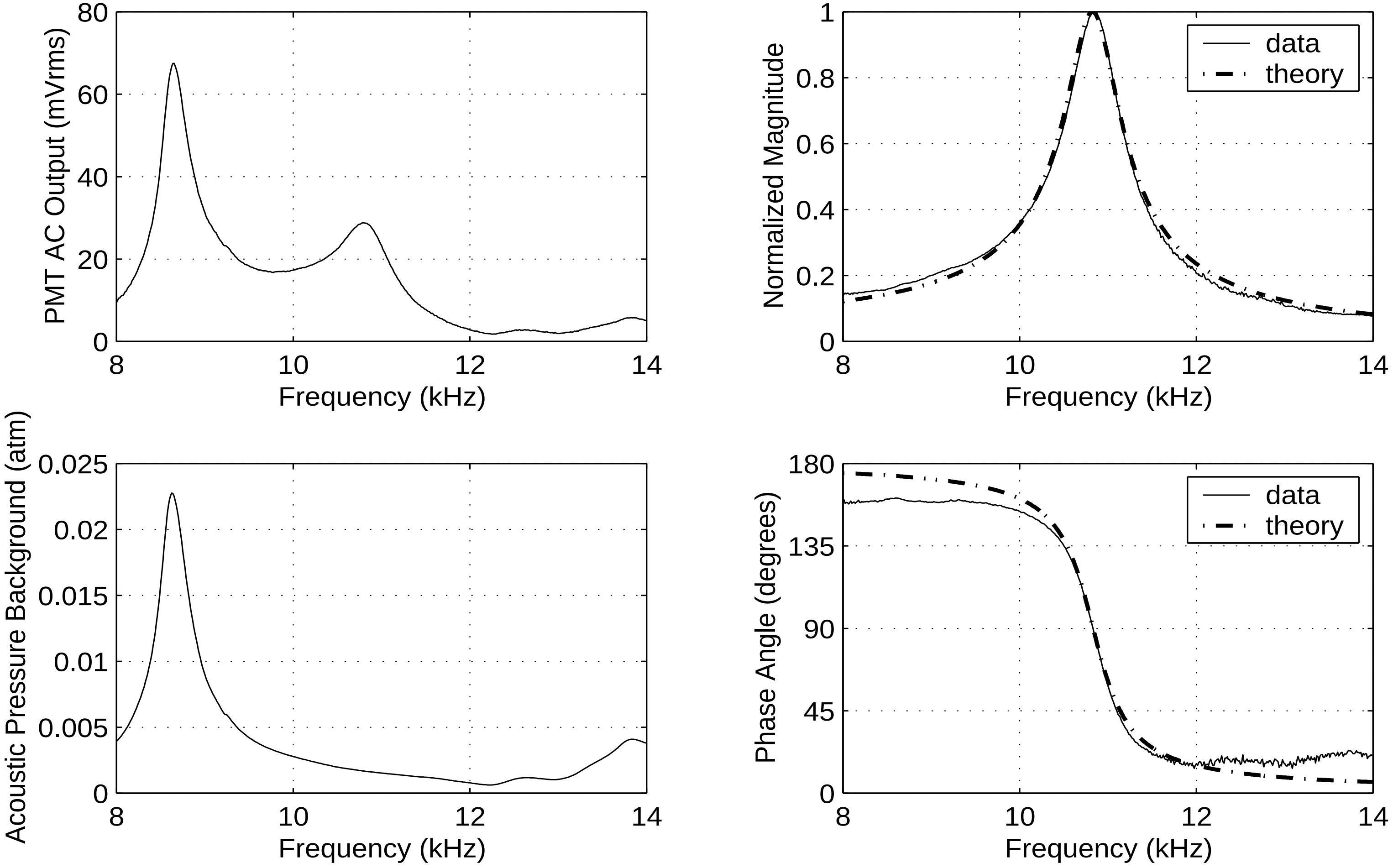

Figure B.8: A 292-μm radius bubble. Fit parameters are: $Q_{\text{fit}} = 18.0$; $f_{0,\text{fit}} = 10832$ Hz; $\beta = 1891\ \text{sec}^{-1}$. Phase data was shifted $-11°$.

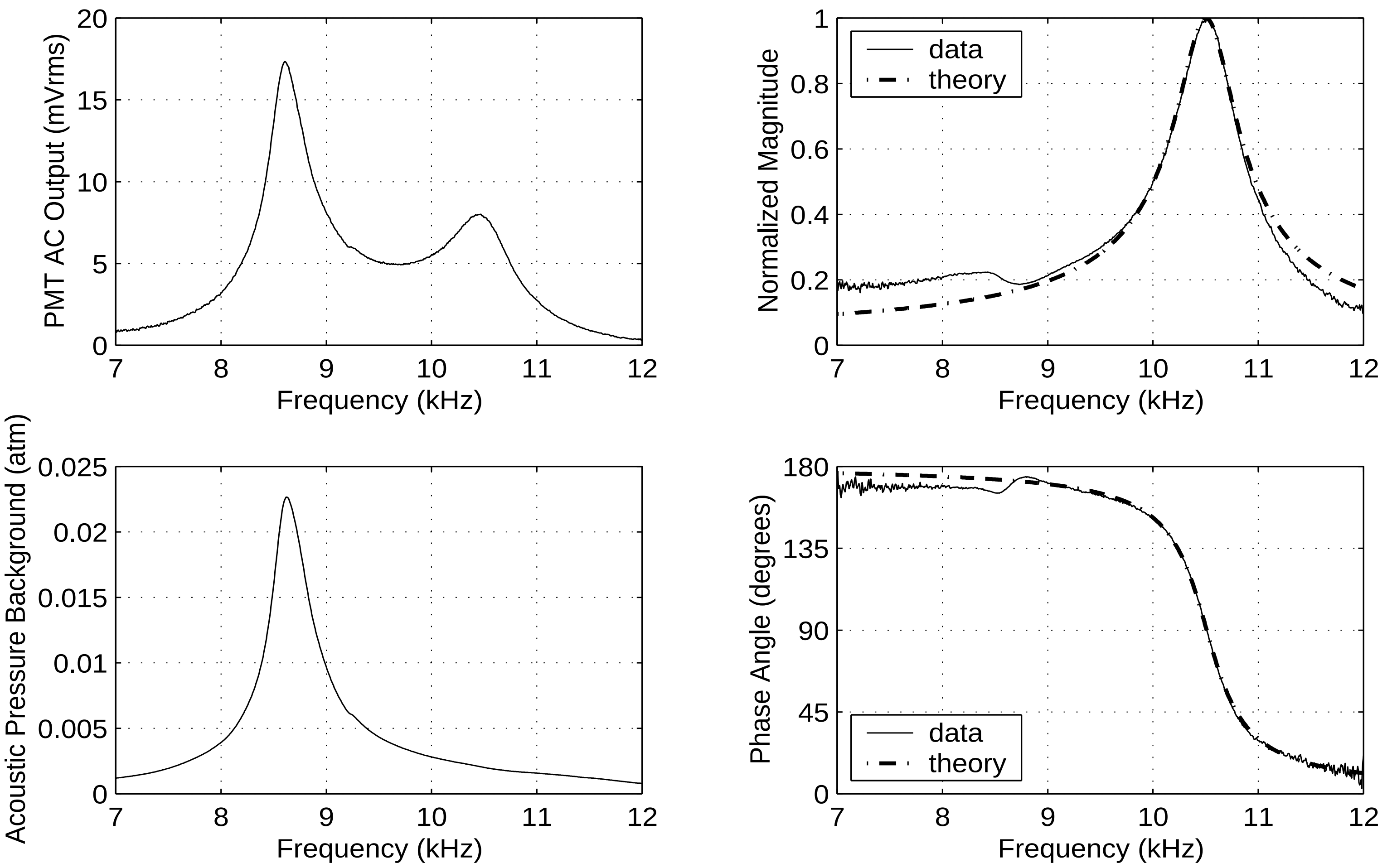

Figure B.9: A 302-μm radius bubble. Fit parameters are: $Q_{\mathrm{fit}} = 18.8$; $f_{0,\mathrm{fit}} = 10510$ Hz; $\beta = 1756\ \mathrm{sec}^{-1}$. Phase data was shifted +34°.

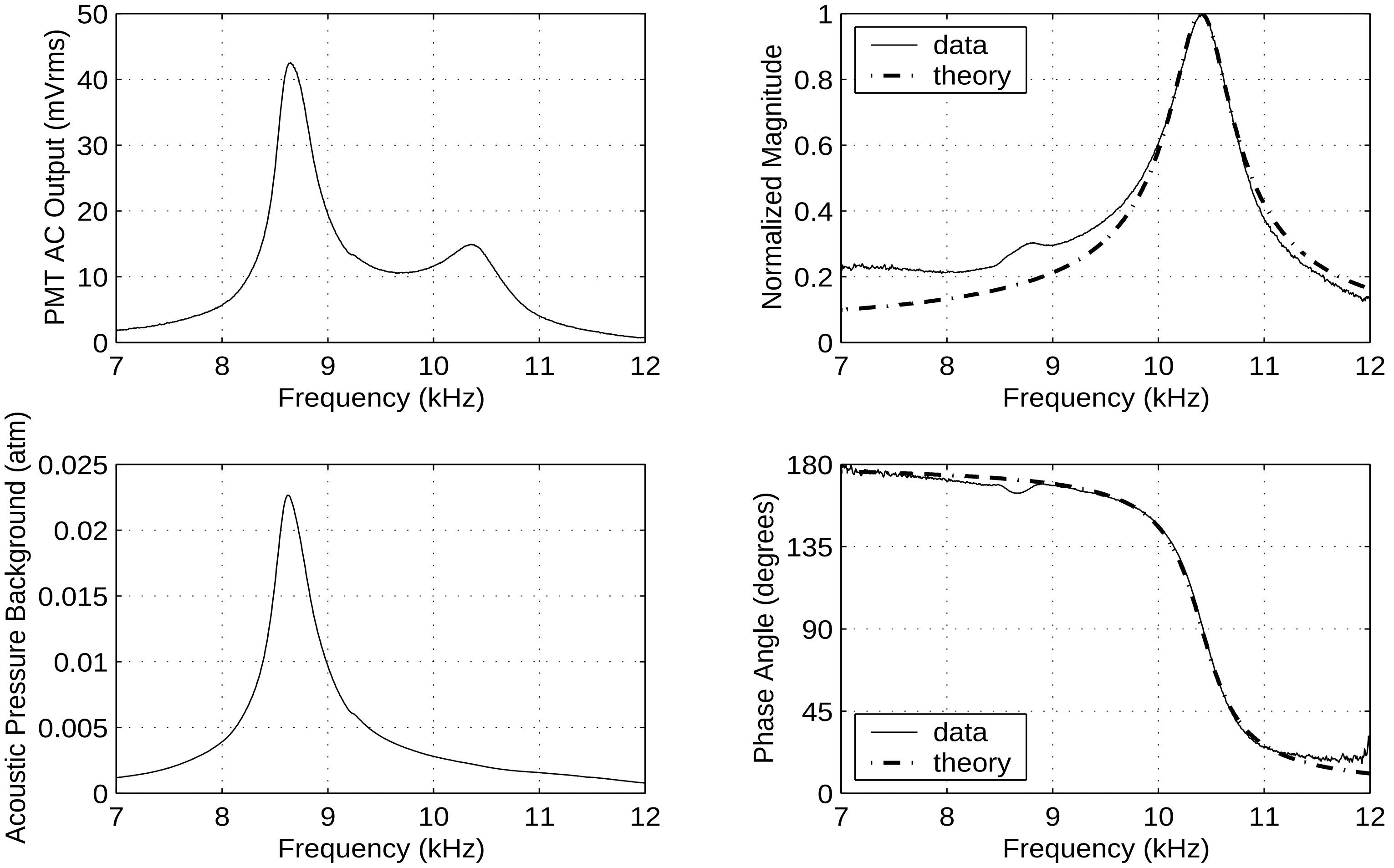

Figure B.10: A 306-μm radius bubble. Fit parameters are: $Q_{\text{fit}} = 18.3$; $f_{0,\text{fit}} = 10411$ Hz; $\beta = 1787\ \text{sec}^{-1}$. Phase data was shifted $+35°$.

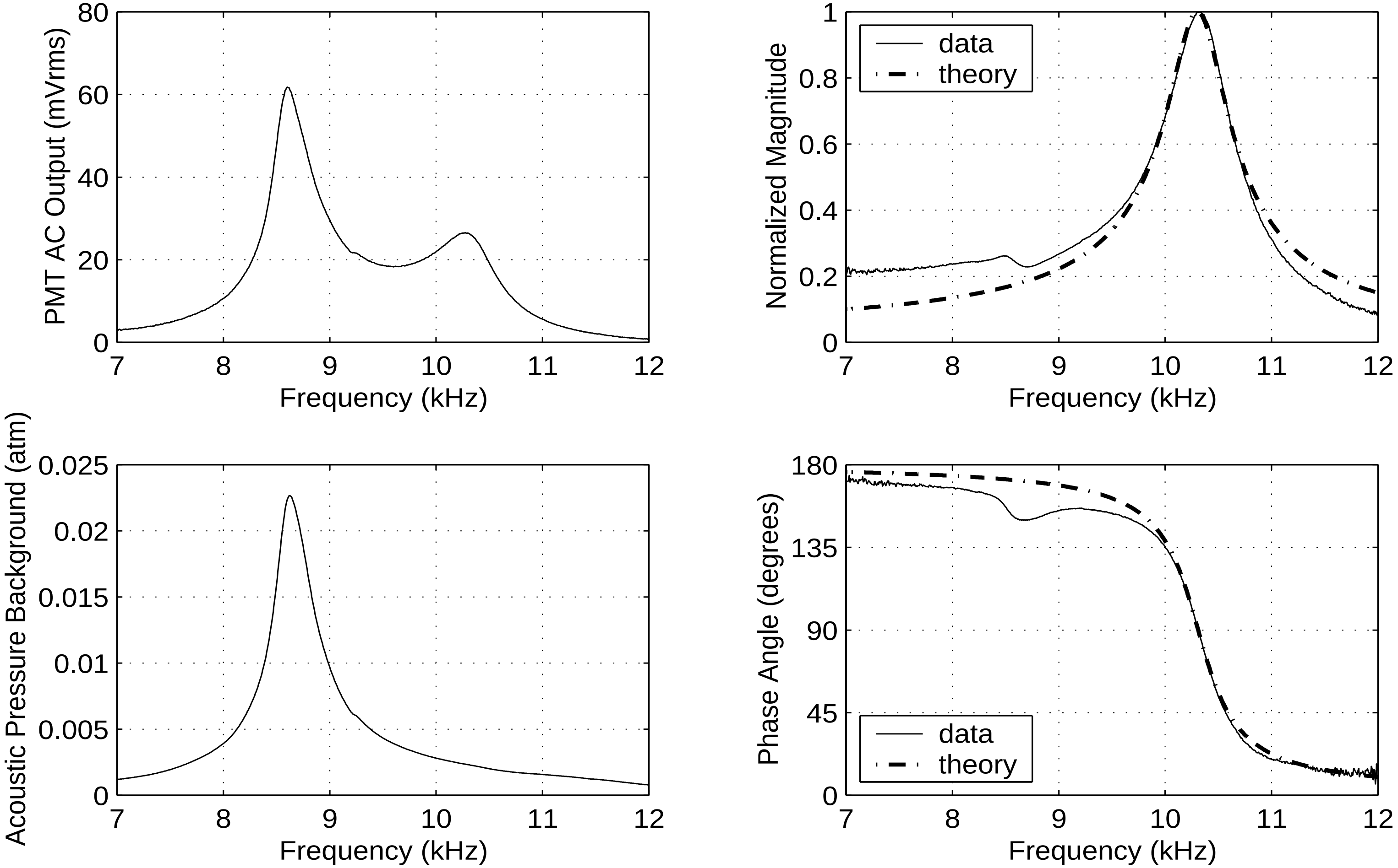

Figure B.11: A 309-μm radius bubble. Fit parameters are: $Q_{\mathrm{fit}} = 18.5$; $f_{0,\mathrm{fit}} = 10310$ Hz; $\beta = 1751\ \mathrm{sec}^{-1}$. Phase data was shifted +36°.

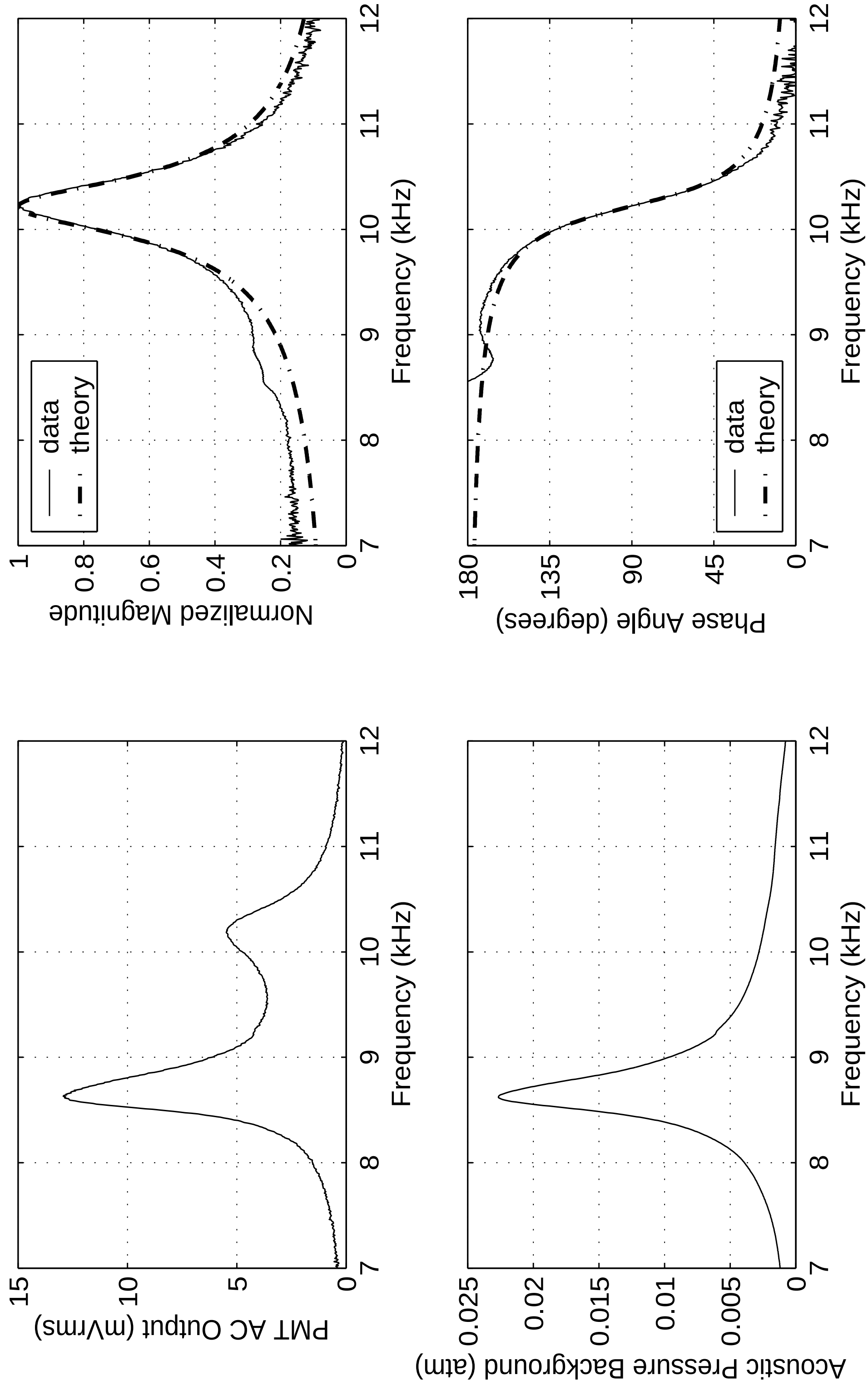

Figure B.12: A 312-μm radius bubble. Fit parameters are: $Q_{\text{fit}} = 20.3$; $f_{0,\text{fit}} = 10220$ Hz; $\beta = 1582$ sec^{-1}. Phase data was shifted $-71°$.

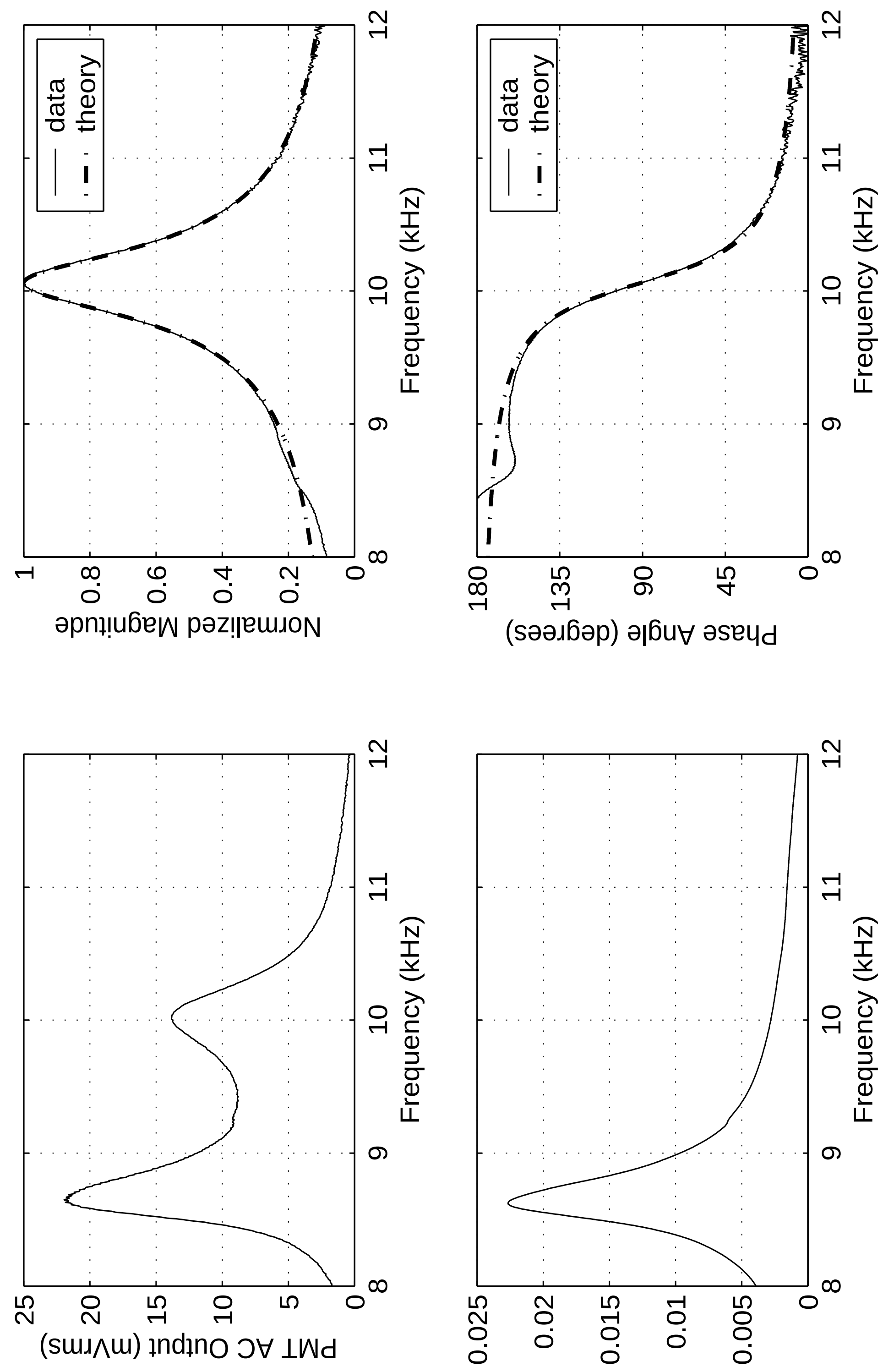

Figure B.13: A 318-μm radius bubble. Fit parameters are: $Q_{\mathrm{fit}} = 21.0$; $f_{0,\mathrm{fit}} = 10065$ Hz; $\beta = 1506$ sec^{-1}. Phase data was shifted $-40°$.

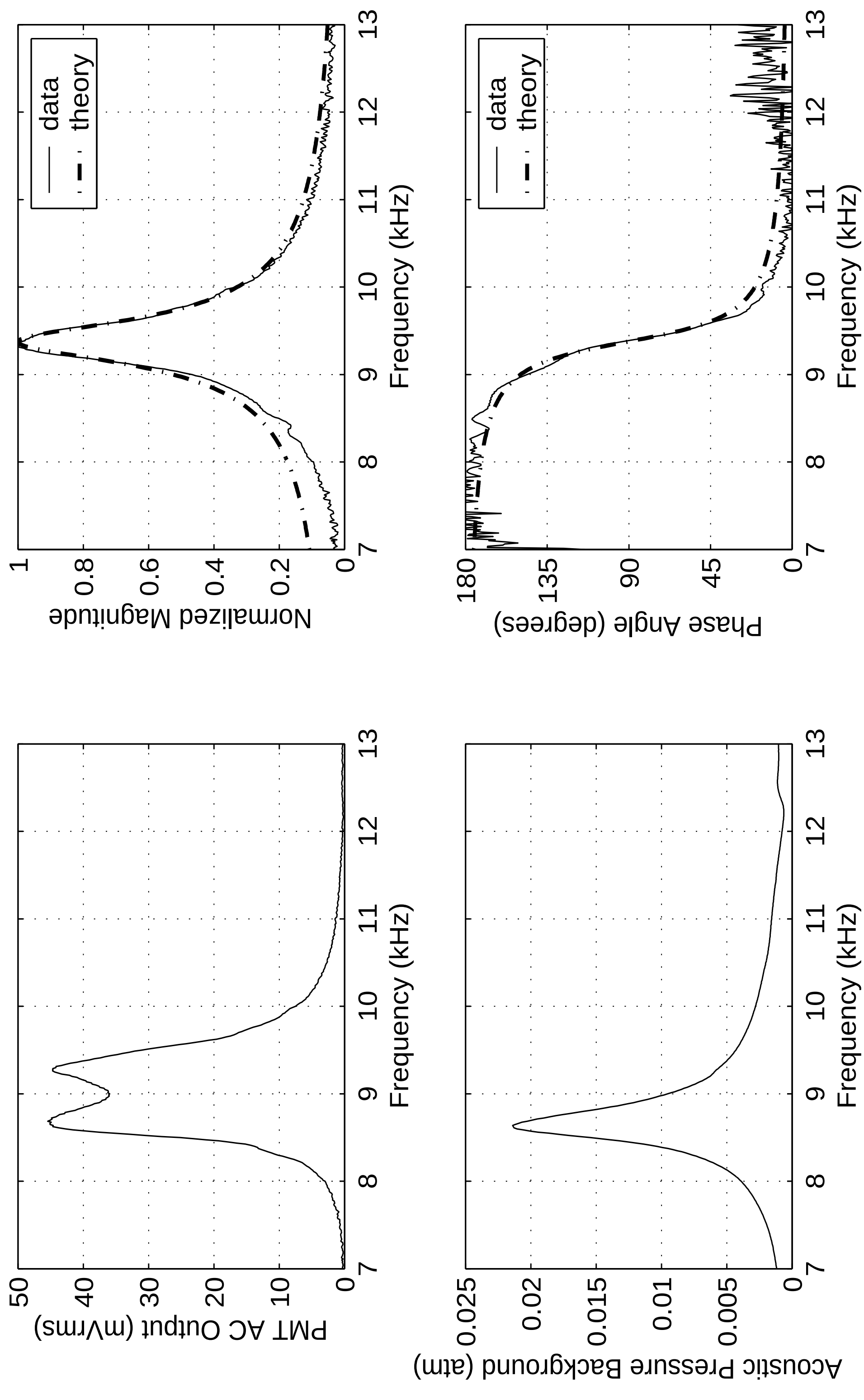

Figure B.14: A 342-μm radius bubble. Fit parameters are: $Q_{\text{fit}} = 20.8$; $f_{0,\text{fit}} = 9379$ Hz; $\beta = 1417$ sec^{-1}. Phase data was shifted $-20°$.

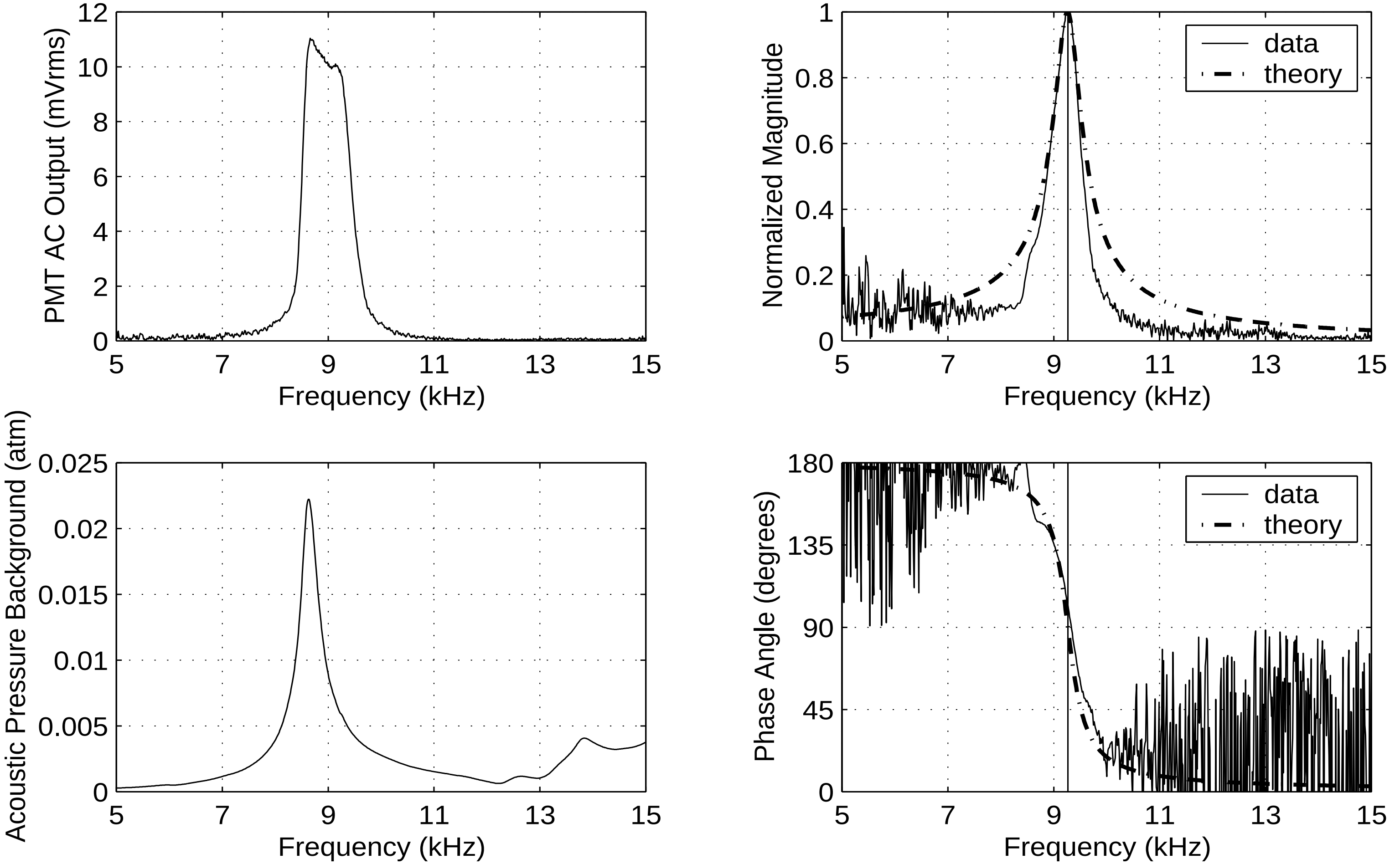

Figure B.15: A 345-μm radius bubble. Bubble coupled to geometric cell resonance. Vertical line shows prediction of bubble resonance by Minnaert's equation. Fit parameters are: $Q_{\text{fit}} = 19.0$; $f_{0,\text{fit}} = 9297$ Hz; $\beta = 1532\ \text{sec}^{-1}$. Phase data was not altered.

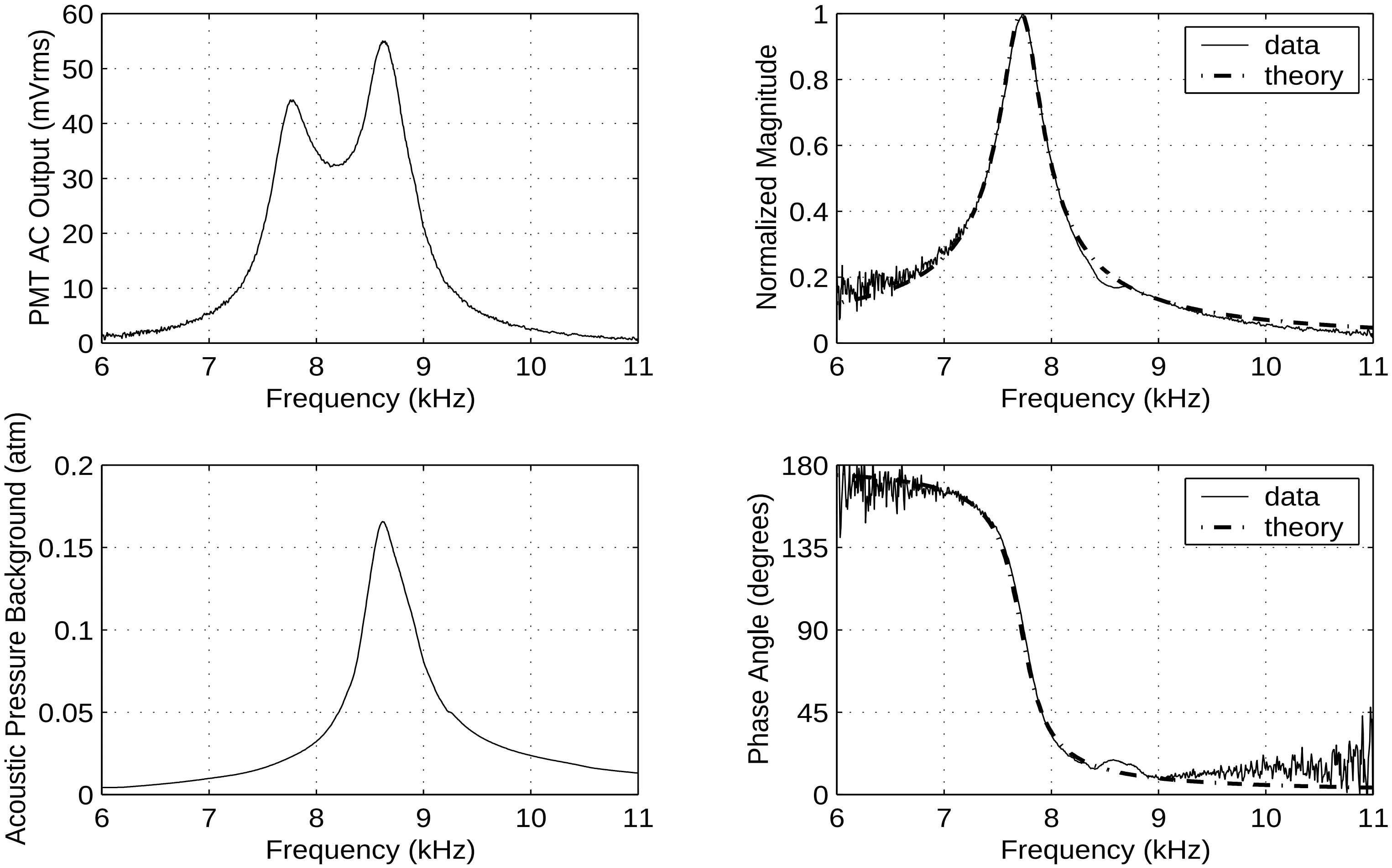

Figure B.16: A 410-μm radius bubble. Fit parameters are: $Q_{\text{fit}} = 20.8$; $f_{0,\text{fit}} = 7722$ Hz; $\beta = 1166\ \text{sec}^{-1}$. Phase data was shifted $+15°$.

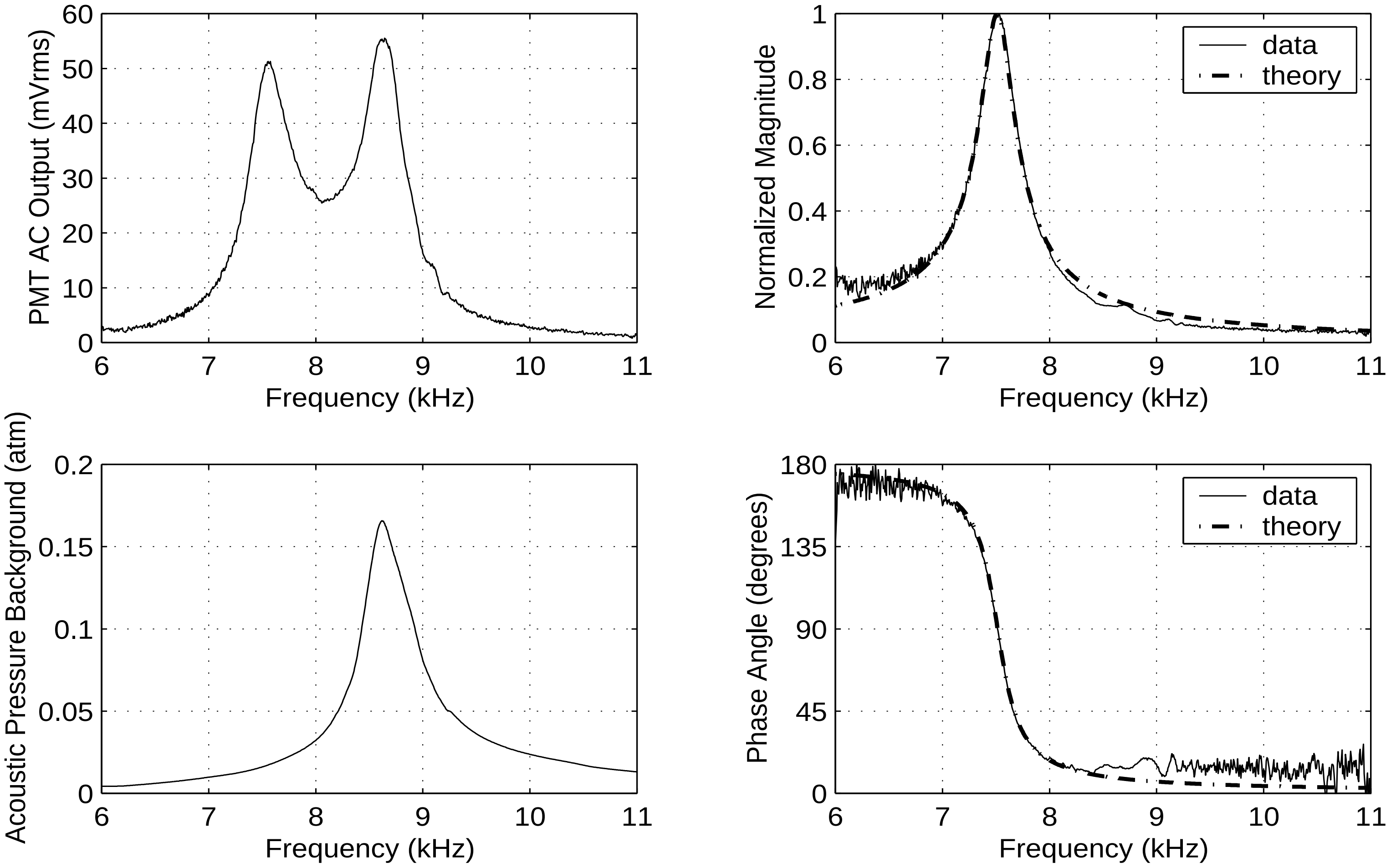

Figure B.17: A 428-μm radius bubble. Fit parameters are: $Q_{\mathrm{fit}} = 24.5$; $f_{0,\mathrm{fit}} = 7515$ Hz; $\beta = 964\ \mathrm{sec}^{-1}$. Phase data was shifted $+8°$.

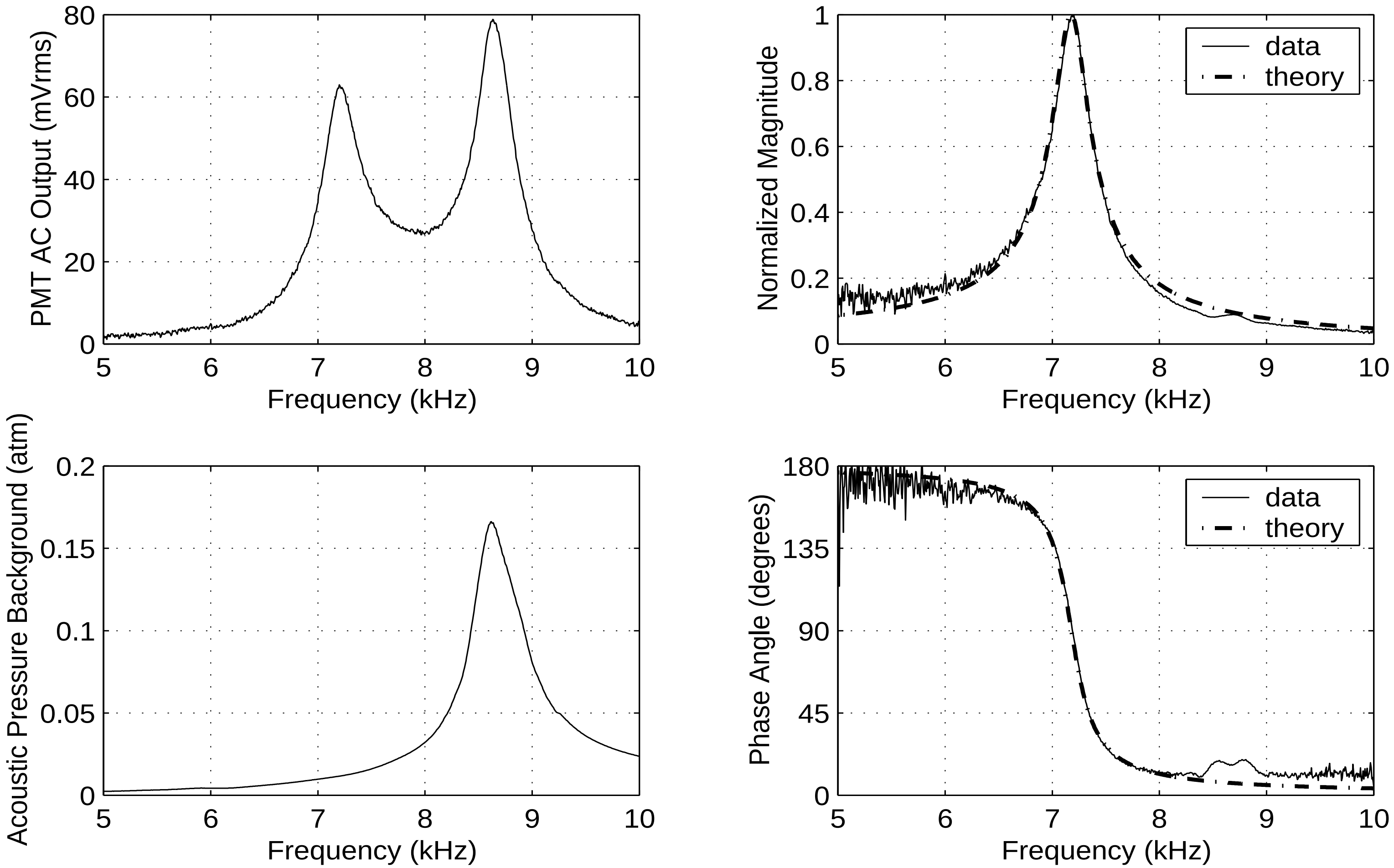

Figure B.18: A 442-μm radius bubble. Fit parameters are: $Q_{\text{fit}} = 22.3$; $f_{0,\text{fit}} = 7179$ Hz; $\beta = 1011\ \text{sec}^{-1}$. Phase data was shifted 5°.

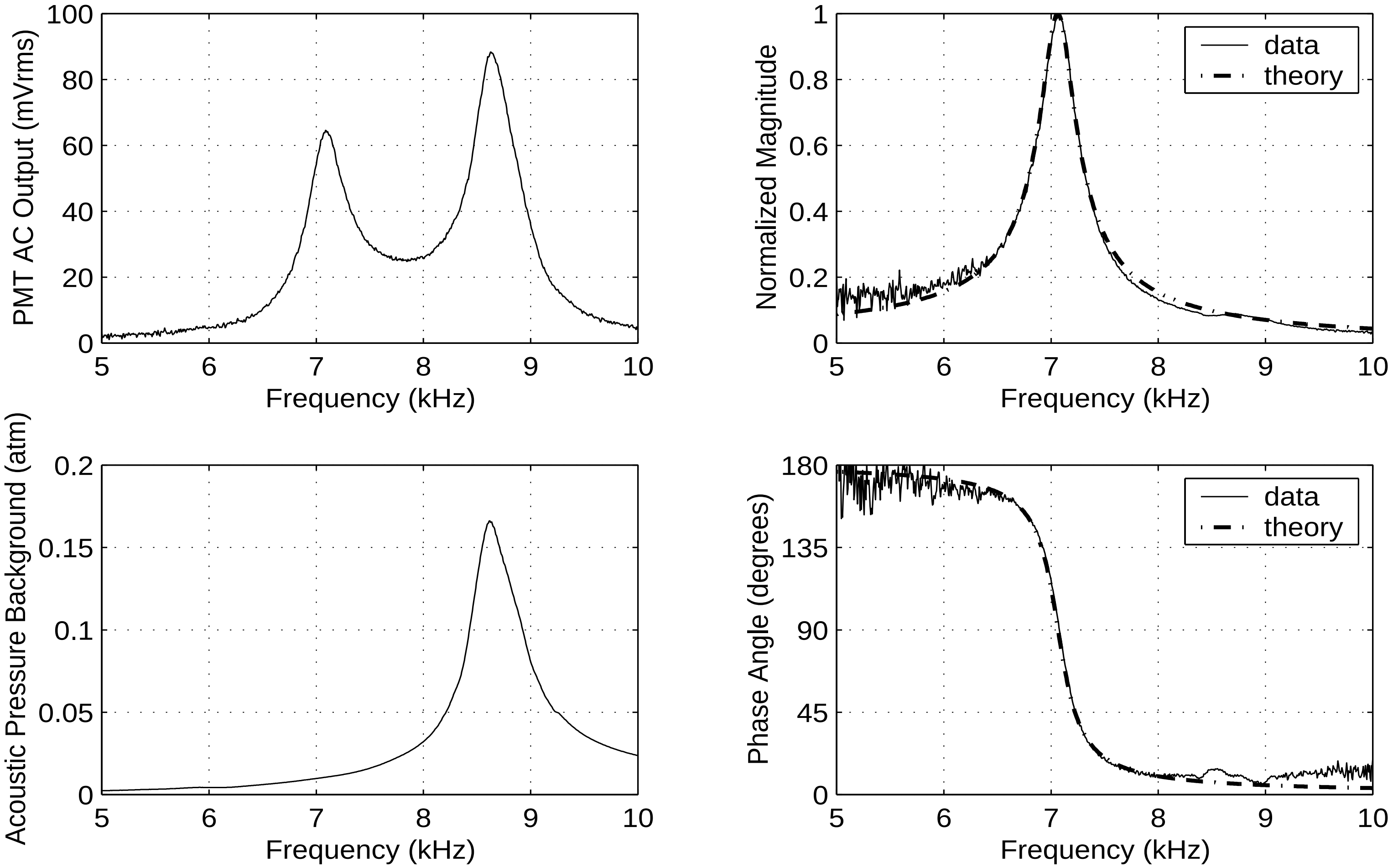

Figure B.19: A 444-μm radius bubble. Fit parameters are: $Q_{\text{fit}} = 22.7$; $f_{0,\text{fit}} = 7066$ Hz; $\beta = 978\ \text{sec}^{-1}$. Phase data was shifted $+12°$.

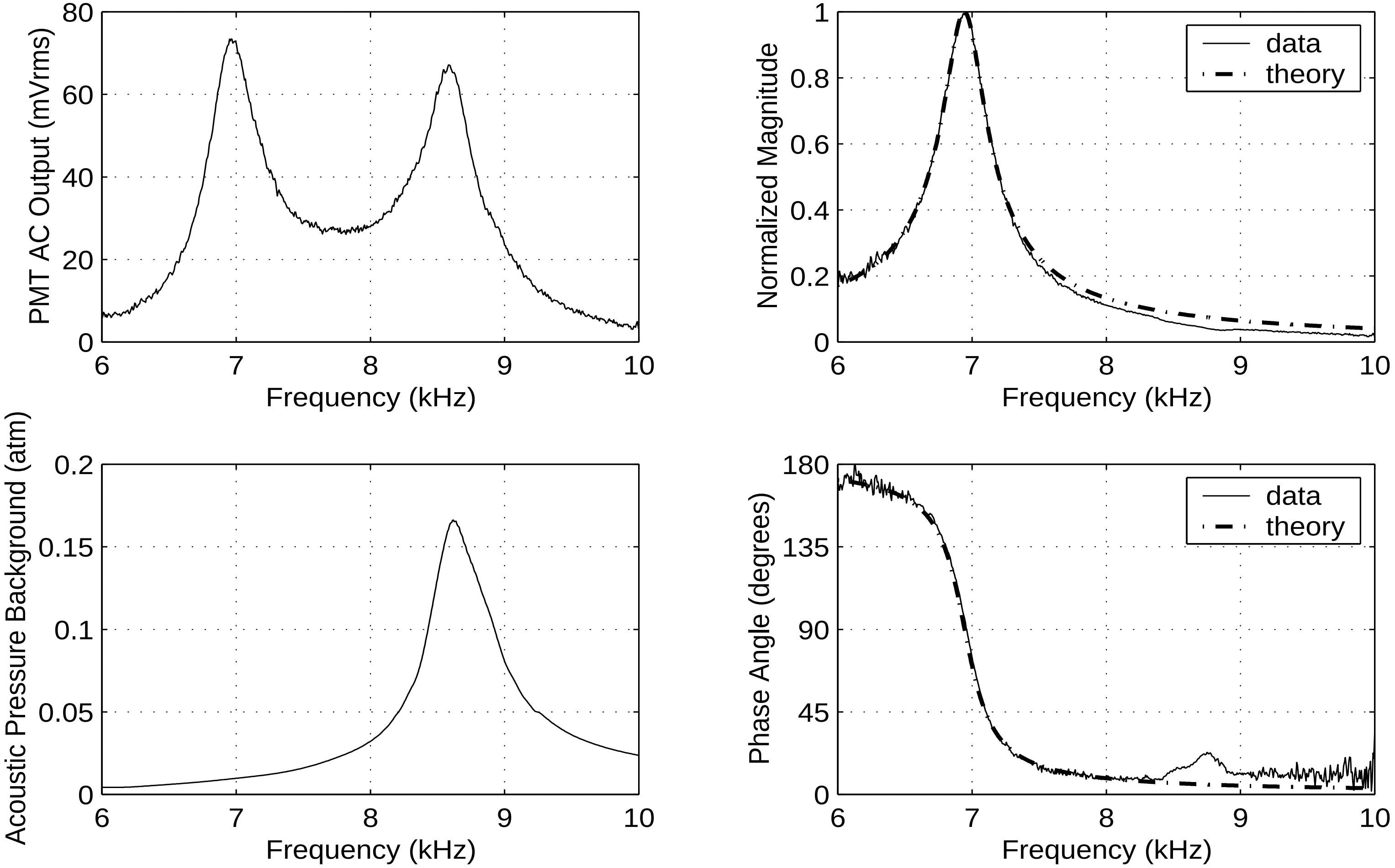

Figure B.20: A 454-μm radius bubble. Fit parameters are: $Q_{\mathrm{fit}} = 22.7$; $f_{0,\mathrm{fit}} = 6945$ Hz; $\beta = 961\ \mathrm{sec}^{-1}$. Phase data was shifted +8°.

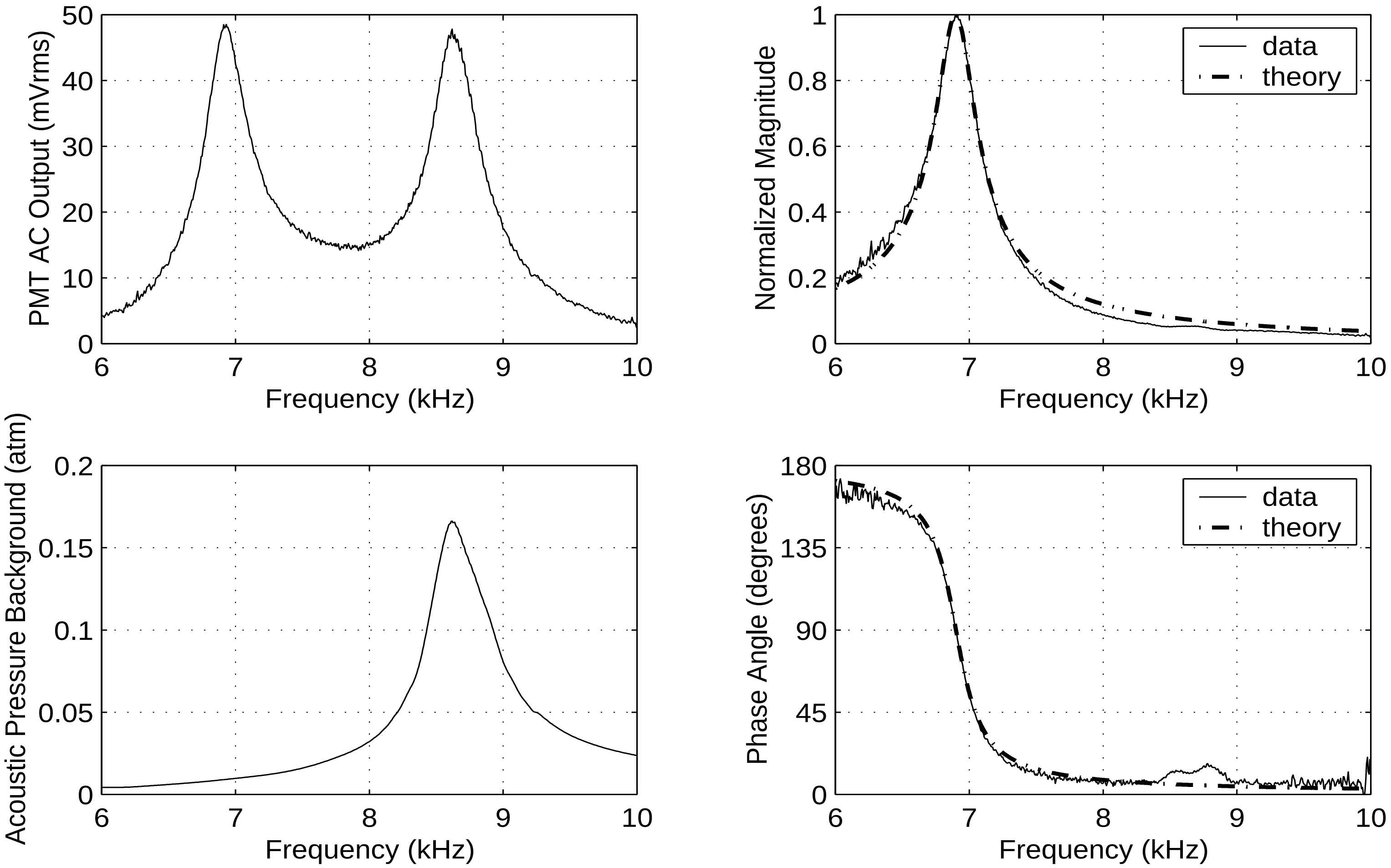

Figure B.21: A 457-μm radius bubble. Fit parameters are: $Q_{\text{fit}} = 24.0$; $f_{0,\text{fit}} = 6901$ Hz; $\beta = 903$ sec^{-1}. Phase data was not altered.

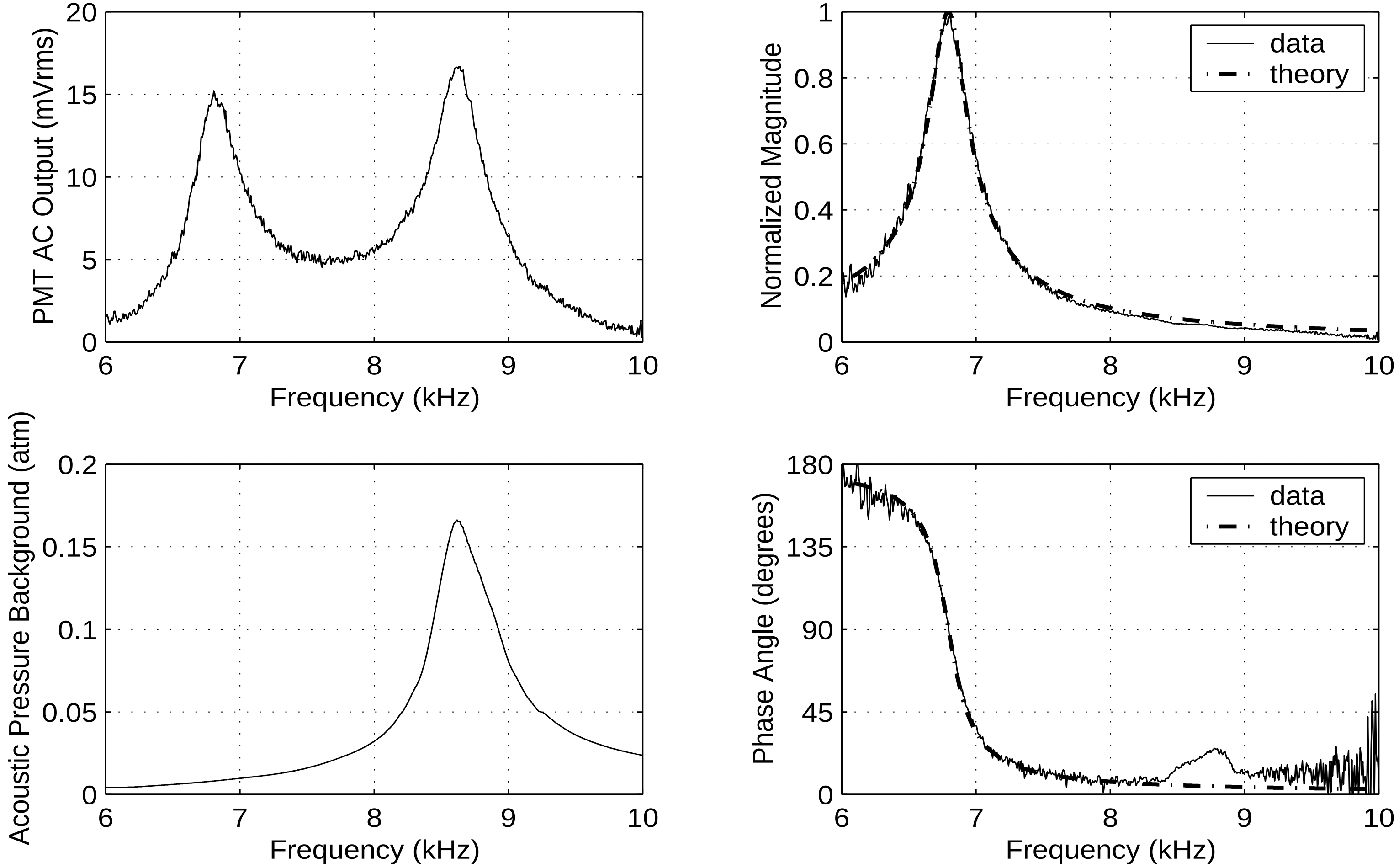

Figure B.22: A 470-μm radius bubble. Fit parameters are: $Q_{\text{fit}} = 25.0$; $f_{0,\text{fit}} = 6796$ Hz; $\beta = 854 \text{ sec}^{-1}$. Phase data was shifted +10°.

Appendix C

Matlab Scripts

This Appendix contains the Matlab scripts written to perform the data processing aspect of this thesis. Although many scripts are dependent on others each script is independently annotated. A short description of the quantity being calculated precedes each script. Note: a '%' symbol precedes a comment line in Matlab. Also, note that all Mie theory plots (see Section 2.1) are computed with the free MIEV0 program written by Wiscombe [47] and are not included here. Matlab, version 11, release 5.3, was used for all computations shown here.

Bubble damping theory: calculates Figures 1.2 and 2.4 without the data and Figures 4.12 and 4.13 with the data. Note that x-axis error bars of Figure 4.12 were added separately.

```
%therm_damp_pros_thesis.m

% This follows the formulation given in:
%       JASA 61, 1, p.17-27 (Jan. 1977) by A. Prosperetti
%       title: Thermal effects and damping mechanisms in the
%       forced radial osciallations of gas bubbles in liquids

ro = 1e-6*(200:500);    %radius of bubble (m)
f = 3.286./ro;      %Minnaert frequency of bubble (Hz)
w = 2*pi*f;         %angular frequency (rad/s)
```

```
mu = 1/1000;        %viscosity of liquid (Pa*s = cP/1000)
c = 1481;       %liquid sound speed (m/s)
T8 = 273.15 + 23.5;     %temperature of the liquid (Kelvin)
Po = 102153;    %ambient pressure (Pa)

% calculate thermal damping by calling phi_ap_thesis.m
[phi rhog rhol G1 G2] = phi_ap_thesis(w,T8,ro);
% Prosperetti "thermal damping"
muth = 0.25.*w.*rhog.*ro.^2.*imag(phi);
% Prosperetti polytropic constant
kappa = (1/3).*1.4.*G1.*G2.*real(phi);

bvis = 2*mu./(rhol*ro.^2);      %viscous damping
bth = 2*muth./(rhol*ro.^2); %thermal damping
bac = .5.*w.*(w.*ro./c)./(1+(w.*ro./c).^2); %radiation damping
btotal = bvis + bth + bac;      %total damping

% resonance frequency
wo = sqrt(3.*kappa.*(Po./(rhol.*ro.^2)));

% bubble radii - measured from CCD images
R = [248;252;263;268;271;289;292;302;306;309;312;318;...
      342;345;410;428;442;444;454;457;470];
% resonance frequency fit parameter
F =
[12979;12505;12092;11792;11392;11001;10832;10510;10411;10310;...
      10220;10065;9379;9297;7722;7515;7179;7066;6945;6945;6796];
% Quality factor fit parameter
Q = [16;13.2;16;17.8;18.3;19;18;18.8;18.3;18.5;20.3;21;20.8;19;...
      20.8;24.5;22.3;22.7;22.7;24;25];
% total damping coefficient - calculated from
B =
[2548;2976;2374;2081;1956;1819;1891;1756;1787;1751;1582;1506;...
      1417;1532;1166;964;1011;978;961;903;854];

% damping ratio
zeta = (1./(2*Q))
% correct damping to match exact damping formulation
B = sqrt(1-zeta.^2).*B;
% convert resonance to natural frequency for Minnaert comp.
F = (1 - 2*zeta.^2).^-0.5.*F;
```

```
%damping error in percent:
% dbeta calculated from damping_error.m for df0=62,dQ=2.1
dbeta = [6.57;7.96;6.57;5.90;5.74;5.53;5.84;5.59;5.75;5.68;...
   5.18;5.01;5.06;5.54;5.06;4.31;4.73;4.65;4.65;4.40;4.22];
Berr = B.*dbeta_plus/100;

% plot total damping calculation and data
figure(1)
set(1,'PaperPosition',[1 2 6 5])
ro = 1e6*ro;
plot(ro,btotal,'k',ro,bth,'k-.',ro,bac,'k:',ro,bvis,'k--')
hold
errorbar(R,B,Berr,'k.')
hold
xlabel('Bubble Radius(\mum)')
ylabel('\beta (sec^{-1})')
axis([200 500 0 3500])
legend('total','thermal','radiation','viscous','data',0)

% plot natural frequency data and Minnaert frequency calculation
figure(2)
set(2,'PaperPosition',[1 2 6 5])
plot(ro,1e-3*wo/2/pi,'k')
hold
errorbar(R,F/1e3,1e-3*62*ones(length(F),1),...
   1e-3*(-20)*ones(length(F),1),'k.')
hold
xlabel('Bubble Radius (\mum)')
ylabel('Bubble Resonance Frequency (kHz)')
axis([200 500 6 14])
legend('Minnaert frequency','data',1)
```

Script called by therm_damp_pros_thesis.m to calculate the thermal damping component.

```
function [phi,rhog,rhol,G1,G2] = phi_ap_thesis(w,T8,ro)

% calculates the thermal quantity phi from the Prosperetti paper
% JASA, 61,1,p. 17-27

rhol = density_water(T8)    %density of water (kg/m^3)
```

```
cpl = heat_cap_water(T8); %heat capacity at const. pres. liq.(J/(kg*K))
kl = therm_cond_water(T8); %Thermal conductivity of liquid (W/(m*K))
Dl = kl./(rhol.*cpl);       %Thermal Diffusivity of liquid (m^2/s)

rhog = 1.293;   %density of air (kg/m^3)
cpg = heat_cap_air(T8); %heat capacity at const. pres. air (J/(kg*K))
kg = therm_cond_air(T8); %Thermal conductivity of air (W/(m*K))
Dg = kg./(rhog.*cpg);   %Thermal Diffusivity of Air (m^2/s)

gamma = 1.4; %ratio of specific heats of diatomic gas (air)
Rg = 8314.47;   %universal gas constant (g*m^2/(s^2*K*mol))
M = 28.94;  %molecular weight of air (g/mol)
cg = sqrt(gamma.*Rg.*T8./M);    %sound speed of gas in bubble (m/s)

G1 = Dg.*w./cg.^2;  %G1,G2,G3 parameters in the paper
G2 = w.*ro.^2./Dg; G3 = w.*ro.^2./Dl;
k = kl./kg;             %thermal conductivity ratio

% calculates equations 16-17 in the paper
repeatd = sqrt((i-G1).^2 + 4*i.*G1./gamma);
F1 = i + G1 + repeatd;
F2 = i + G1 - repeatd;
B1 = sqrt(.5*gamma.*G2.*(i - G1 + repeatd));
B2 = sqrt(.5*gamma.*G2.*(i - G1 - repeatd));
lam1 = B1.*coth(B1)-1;
lam2 = B2.*coth(B2)-1;
f = 1 + (1+i).*sqrt(.5.*G3);

phitop = k.*f.*(F2-F1) + lam2.*F2-lam1.*F1;
phibot = k.*f.*(lam2.*F1-lam1.*F2) - lam1.*lam2.*(F2-F1);

phi = phitop./phibot;
```

Script called by phi_ap_thesis, that calculates the density of water for a given temperature: density_water.m

```
function rhol = density_water(T)

% calculates the density of water (kg/m^3)
% at a given temp by interpolating between values given
% in the CRC Handbook of Chemistry and Physics article
```

```
% Thermodynamic Properties of Air

t = 0:40; %temp values for given density values (Celsius)
rhog_disc = [999.8426;999.9015;999.9429;999.9672;999.9750;...
      999.9668;999.9430;999.9043;999.8509;999.7834;999.7021;...
      999.6074;999.4996;999.3792;999.2464;999.1016;998.9450;...
      998.7769;998.5976;998.4073;998.2063;997.9948;997.7730;...
      997.5412;997.2994;997.0480;996.7870;996.5166;996.2371;...
      995.9486;995.6511;995.3450;995.0302;994.7071;994.3756;...
      994.0359;993.6883;993.3328;992.9695;992.5987;992.2204];

T = T - 273.15;  %convert Kelvin to Celsius

rhol = interp1(t,rhog_disc,T); %interpolate the the desired value
```

Script called by phi_ap_thesis, that calculates the heat capacity of water for a given temperature: heat_cap_water.m

```
function cp = heat_cap_water(T)

% calculates the heat capacity at const pres. of water (J/kg*K)
% using a formula given by NIST

A = -203.6060; B = 1523.290; C = -3196.413;
D = 2474.455; E = 3.855326;

t = T/1000;
%good for T = 298-500 K; cp in J/(mol*K)

%molar mass of water (g/mol)
M = 18.01528;
M = M/1000; %g/mol -> kg/mol

cp = (A + B*t + C*t.^2 + D*t.^3 + E*t.^-2)/M;
```

Script called by phi_ap_thesis, that calculates the thermal conductivity of water for a given temperature: therm_cond_water.m

```
function k = therm_cond_water(T)
```

```
% calculates the thermal conductivity of water (W/(K*m))
% at a given temp by interpolating between values given
% in the CRC Handbook of Chemistry and Physics article
%  Properties of Water in the Range 0-100 C.

temp = 0:10:100; %temperature corresponding to given values
k_disc = 1e-3*[561;580;598.4;615.4;630.5;643.5;654.3;...
      663.1;670;675.3;679.1];

T = T - 273.15;     %Convert temp from Kelvin to Celsius

k = interp1(temp,k_disc,T);     %interpolate to desired k
```

Script called by phi_ap_thesis, that calculates the heat capacity of air for a given temperature: heat_cap_air.m

```
function cp = heat_cap_air(T)

%calculates the heat capacity at const pres. of air (J/(kg*K))
% at a given temp by interpolating between values given
% in the CRC Handbook of Chemistry and Physics article
%  Thermodynamic Properties of Air

temp = [100;200;300;500;1000];
cp_disc = [1032;1007;1007;1030;1141];

cp = interp1(temp,cp_disc,T);
```

Script called by phi_ap_thesis, that calculates the thermal conductivity of air for a given temperature: therm_cond_air.m

```
function k = therm_cond_air(T)

% Originally from SFPE Handbook of Fire Protection Engineering,
% 2nd Ed., Table B-2, but also found on
% http://www.wpi.edu/~ierardi/FireTools/air_prop.html

k = 1.5207e-11*T.^3 - 4.8574e-8*T.^2 + 1.0184e-4*T - 3.9333e-4;
```

An example of the script used to fit parameters f_0 and Q to the magnitude of a bubble response: Qfit_01112803_appendix_b.m – a 318 μm bubble

```
%Qfit_01112803_appendix_b.m

clear

% raw pmt output data file
file1 = '01112803.txt';
[re1 im1 f1] = textread(file1,'%f %f %f');
% hydrophone output data file
[re2 im2 f2] = textread('01112803-7bg.txt','%f %f %f');

% Pick frequency range you want to look at
startf = 8000; endf = 12000;

[q1 i1] = min(abs(startf-f1));
[q2 i2] = min(abs(endf-f1));
numpts = i2-i1+1;

d1 = complex(re1,im1);
d1 = d1(i1:i2);
mag1 = abs(d1);
d2 = complex(re2,im2);
d2 = d2(i1:i2);
mag2 = abs(d2);

f = f1(i1:i2)/1e3;  %Frequency points for range chosen (kHz)

eps = 1e-4;     %Wiener filter parameter
d = d1.*conj(d2)./(d2.*conj(d2) + eps); %calculate bub. resp.
dmag = abs(d)/max(abs(d));      %normalize to peak of mag. plot
dph = atan(imag(d)./real(d));   %calculate phase data
dphdeg = 180/pi*dph;        %convert phase to degrees
index = 526-i1+1;
dphdeg(1:index) = dphdeg(1:index) + 180; %unwrap phase

fontsize = 10;
figure(5)
set(5,'PaperPosition',[0.25 1 8 5])
subplot(2,2,1)
plot(f,1e3*mag1,'k')
```

```
set(gca,'FontSize',fontsize)
xlabel('Frequency (kHz)')
ylabel('PMT AC Output (mVrms)')
grid on

% convert to absolute pressure using hydrophone calibration
mag2 = mag2/1e-3/101325;

subplot(2,2,3)
plot(f,mag2,'k')
set(gca,'FontSize',fontsize)
xlabel('Frequency (kHz)') y
label('Acoustic Pressure Background (atm)')
grid on

%-------------------------------------------------------
% Fit damped oscillator theory to the equalized data

Q = 21;         %quality factor parameter guess
fo = 10340;     %initial resonance frequency guess from Minnaert

% call the least-square-error fit script
[Q fo] = magfit_iter_thesis(f,dmag,Q,fo);
w = 2*pi*1e3*f;     %angular frequency range
wo = 2*pi*fo;       %resonance frequency parameter

beta = wo/2/Q;      %calculate total damping coefficient

% normalized amplitude calculated from fit parameters
A = ((wo^2-w.^2).^2 + (w*wo/Q).^2).^-.5;
Am = max(A);
A = A/Am;

% unwrapped phase calculated from fit parameters
phi = -atan(w.*wo./(Q.*(wo^2-w.^2)));
for q = 1:length(phi)
   if phi(q) < 0
      phi(q) = phi(q) + pi;
   end
end
phi = phi*180/pi;  %convert to degrees
```

```
% plot the magnitude calculation and data
subplot(2,2,2)
plot(f,dmag,'k','LineWidth',0.5)
hold
plot(f,A,'k-.','LineWidth',1.5)
hold
set(gca,'FontSize',fontsize)
xlabel('Frequency (kHz)')
ylabel('Normalized Magnitude')
grid on
axis([startf/1e3 endf/1e3 0 1])
legend('data','theory',1)

r = 318e-6;     %measured radius from CCD image
offset = -40;   %data phase offset <- normalize the phase

% plot the phase calculation and data
subplot(2,2,4)
plot(f,dphdeg+offset,'k','LineWidth',0.5)
hold
plot(f,phi,'k-.','LineWidth',1.5)
hold
set(gca,'FontSize',fontsize,'YTick',[0 45 90 135 180])
xlabel('Frequency (kHz)')
ylabel('Phase Angle (degrees)')
grid on
axis([startf/1e3 endf/1e3 0 180])
legend('data','theory',1)
```

The script that calls the parameter fit script twice: magfit_iter_thesis.m

```
function [Qi2,foi2] = magfit_iter_thesis(f,dmag,Q,fo)

% This function calls the fitting script twice.  Each time
% it calls with a set of ranges for f0 and Q

% 1st iteration
fo_r = (fo-1000):10:(fo+1000); %f0 range
Qr = (Q-5):.5:(Q+5);    %Q range

[Qi1 foi1 ei1] = magfit(f,dmag,Qr,fo_r); %call to fit script
```

```
% 2nd iteration using results from 1st iteration
fo_r = (foi1-30):(foi1+30); %f0 range
Qr = (Q1-1):.1:(Q1+1);  %Q range

[Qi2 foi2 ei2] = magfit(f,dmag,Qr,fo_r)
```

The script that calculates the parameter fit to the bubble magnitude response: magfit.m

```
function [Q_calc,fo_calc,err] = magfit(fr,m,Q,fo)

%Fit damped oscillator theory to the equalized data
%
% fr: the frequency data points (in kHz)
% m: the corresponding magnitude points
% Q: a range of Q's (a vector)
% fo: a range of fo's (a vector)

w = 2*pi*1e3*fr;        %angular frequency range
wo = 2*pi*fo;       %resonance frequency parameter

for n = 1:length(wo)
   for p = 1:length(Q)

      A = ((wo(n)^2-w.^2).^2 + (w*wo(n)/Q(p)).^2).^-.5;
      Am = max(A);
      A = A/Am;     %Normalized theoretical magnitude

      magerr = m-A;             %Magnitude error
      me2 = magerr.^2;          %Squared mag error
      sme2(n,p) = sum(me2);     %Total sqrd mag error

   end
end

% find minimum squared error
[ival iind] = min(sme2);
[jval jind] = min(ival);

% minimum-squared error, f0 fit parameter, Q fit paramter
```

```
err = sme2(iind(1),jind);
fo_calc = fo(iind(1));
Q_calc = Q(jind);
```

An example of the script used to fit parameter Q to the phase of a bubble response holding constant the f_0 magnitude-fit parameter: phasefit_thesis_318um.m – a 318 μm bubble

```
%function [mag,err] = phasefit_thesis_318um(fr,dph,Q,fo)

% Fit damped oscillator theory to the equalized data
%   using phase data only.  This serves as a check on the
%   magnitude fit.

clear

% raw pmt output data file
file1 = '01112803.txt';
[re1 im1 f1] = textread(file1,'%f %f %f');
% hydrophone output data file
[re2 im2 f2] = textread('01112803-7bg.txt','%f %f %f');

% Pick frequency range you want to look at - calculation
% of Q needs only the phase data close to resonance
startf = 9865; endf = 10265;

[q1 i1] = min(abs(startf-f1));
[q2 i2] = min(abs(endf-f1));
numpts = i2-i1+1;

d1 = complex(re1,im1);  %complex pmt data
d1 = d1(i1:i2);
d2 = complex(re2,im2);  %complex hydrophone data
d2 = d2(i1:i2);

f = f1(i1:i2)/1e3;  %Frequency points for range chosen (kHz)

eps = 1e-4;     %Wiener filter parameter
d = d1.*conj(d2)./(d2.*conj(d2) + eps);     %equalization
dphase = atan(imag(d)./real(d));    %compute phase
dphdeg = 180/pi*dphase;     %convert to degrees
```

```
index = 523-i1+1;
dphdeg(1:index) = dphdeg(1:index) + 180; %unwrap phase
dph = pi/180*(dphdeg-40);       %normalize phase

Q = 10:.1:25;           %range of Q
fo = 10065;             %frequency from magnitude
w = 2*pi*f*1e3;     %angular frequency range (rad/sec)
wo = 2*pi*fo;       %resonance frequency parameter

for p = 1:length(Q)

   %calculate phase with range of Q
   phi(:,p) = -atan(w.*wo./(Q(p).*(wo^2-w.^2)));

   %unwrap phase
   for q = 1:length(w)
      if phi(q,p) < 0
         phi(q,p) = phi(q,p) + pi;
      end
   end

   phaseerr = dph-phi(:,p); %deviation between calc. and data
   pe2 = phaseerr.^2;          %squared deviation(error)
   spe2(p) = sum(pe2);         %sumed squared error

end

[ival iind] = min(spe2);    %minimum total squared error

spe_min = spe2(iind);
Q_calc = Q(iind);           %corresponding Q parameter

figure(2)
plot(f,180/pi*phi(:,iind),f,180/pi*dph,[f(1),f(length(f))],[90,90])
title(['R_0 = 318 \mum; Q_{fit} = ',num2str(Q_calc)])
```

The script that computes Equation 4.9: resfreq_error.m.

```
%resfreq_error.m

% This script determines the error inherent in the
```

```
% resonance frequency measurement.

dR0 = 14e-6;     %bubble radius uncertainty
dP0 = 1391;      %ambient pressure uncertainty
dq = 0.12;       %density uncertainty

R0 = 240e-6:1e-6:470e-6;    %range of bubble radii
P0 = 102153;            %mean ambient pressure (Pa)
q = 997.42;             %mean density of liquid (kg/m^3)

term1 = -dR0./R0;
term2 = dP0./2/P0;
term3 = -dq./2/q;

% Minnaert natural frequency of bubble
f0 = (2*pi)^-1*sqrt(3*1.4*P0/q)./R0;

% uncertainty in f0
df0 = f0.*sqrt(term1.^2 + term2.^2 + term3.^2);
df0 = df0./f0;      %expressed as a percent

figure(1) set(1,'PaperPosition',[1 3 4 3.3])
plot(1e6*R0,100*abs(df0),'k')
set(gca,'FontSize',9)
xlabel('Bubble Radius (\mum)')
ylabel('% Error')
grid on
axis([240 470 3 6])
```

The script that computes Equation 4.11: fit_precision.m.

```
%fit_precision.m

R = [248;252;263;268;271;289;292;302;306;309;312;318;342;345;...
      410;428;442;444;454;457;470];
SqrdErr = [0.869;0.715;0.105;0.177;0.178;0.317;0.149;0.088;...
      0.173;0.130;0.237;0.118;0.764;0.114;0.387;0.459;0.578;...
      0.491;0.249;0.360;0.183];
```

```
N = 801; m = 2; nu = N-(m+1);

StdDev = SqrdErr./nu;

figure(1)
set(1,'PaperPosition',[1 3 4 3.3])
plot(R,StdDev,'k*')
set(gca,'FontSize',9)
grid on
xlabel('Bubble Radius (\mum)')
ylabel('Standard Error of the Fit, \sigma')
```

The script that computes Equation 4.13: damping_error.m.

```
%damping_error.m

% This script determines the error inherent in the
% calculation of the damping coeffiecient.

%bubble radius data
R = [248;252;263;268;271;289;292;302;306;309;312;318;...
      342;345;410;428;442;444;454;457;470];

%resonance frequency fit to data
f0=[12979;12505;12092;11792;11392;11001;10832;10510;10411;10310;...
      10220;10065;9379;9297;7722;7515;7179;7066;6945;6945;6796];

%Q fit to data
Q=[16;13.2;16;17.8;18.3;19;18;18.8;18.3;18.5;20.3;21;20.8;19;...
      20.8;24.5;22.3;22.7;22.7;24;25];

%damping coefficient calculated from f0 and Q
beta=[2548;2976;2374;2081;1956;1819;1891;1756;1787;1751;1582;1506;...
      1417;1532;1166;964;1011;978;961;903;854];

%uncertainty in f0 and Q
df0 = 62; dQ = 2.1;

term1 = df0/2./f0;
term2 = -dQ./2./Q;

%percent error for damping coefficient
dbeta = 100*sqrt(term1.^2 + term2.^2);
```

```
figure(1)
set(1,'PaperPosition',[1 3 4 3.3])
plot(R,dbeta,'k*')
set(gca,'FontSize',9)
xlabel('Bubble Radius (\mum)')
ylabel('% Error in Calculated Damping')
grid on
```

Bibliography

[1] Julius S. Bendat and Allan G. Piersol. *Engineering Applications of Correlation and Spectral Analysis*, pages 49–55. John Wiley and Sons, New York, 1980.

[2] Julius S. Bendat and Allan G. Piersol. *Random Data Analysis and Measurement Procedures*, pages 22–23. John Wiley and Sons, New York, 3rd edition, 2000.

[3] V. F. K. Bjerknes. *Fields of Force.* Columbia University Press, New York, 1906.

[4] J.E. Blue. Resonance of a bubble on an infinite rigid boundary. *Journal of the Acoustical Society of America*, 41(2):555–560, 1967.

[5] W. M. Carey and M. Browning. Low frequency ocean ambient noise measurement and theory. In B. R. Kerman, editor, *Sea Surface Sound*, pages 361–376. Kluwer Press, 1988.

[6] W. M. Carey, J. W. Fitzgerald, E. C. Monahan, and Q. Wang. Measurement of the sound produced by a tipping trough with fresh and salt water. *Journal of the Acoustical Society of America*, 93(6):3178–3192, 1993.

[7] E. L. Carstensen and L. L. Foldy. Propagation of sound through a liquid containing bubbles. *Journal of the Acoustical Society of America*, 19(3):481–501, 1947.

[8] R. B. Chapman and M. S. Plesset. Thermal effects in the free oscillations of gas bubbles. *Journal of Basic Engineering*, 94:142–145, 1971.

[9] Kerry W. Commander and Andrea Prosperetti. Linear pressure waves in bubbly liquids: Comparison between theory and experiments. *Journal of the Acoustical Society of America*, 85(2):732–746, 1989.

[10] Charles Devin, Jr. Survey of thermal, radiation, and viscous damping of pulsating air bubbles in water. *Journal of the Acoustical Society of America*, 31(12):1654–1667, 1959.

[11] A. A. Doinikov. Acoustic radiation pressure on a compressible sphere in a viscous fluid. *Journal of Fluid Mechanics*, 267:1–21, 1994.

[12] Richard S. Figliola and Donald E. Beasley. *Theory and Design for Mechanical Measurements*, pages 88–94. John Wiley and Sons, Inc, New York, 2000.

[13] G. J. Franz. Splashes as sources of sound in liquids. *Journal of the Acoustical Society of America*, 31(8):1080–1096, 1959.

[14] A. P. French. *Vibrations and Waves*, pages 83–91. W. W. Norton & Company, Inc, New York, 1971.

[15] Hamamatsu. 7696 photomultiplier tube, technical data sheet pm-227. Sent by mail, 2001. (Hamamatsu Corporation).

[16] Gary M. Hansen. *Mie Scattering as a Technique for the Sizing of Air Bubbles.* Ph.D Dissertation, The University of Mississippi, Oxford, 1983.

[17] R. G. Holt. Optical Mie scattering to observe single cavitation bubble dynamics. *Journal of the Acoustical Society of America*, 108(5,pt.2):2516, 2000.

[18] R. Glynn Holt and Lawrence A. Crum. Experimental observation of the nonlinear response of single bubbles to an applied acoustic field. Technical Report NCPA LC.02 1988, National Center for Physical Acoustics, 1988.

[19] S. D. Howkins. Measurements of the resonant frequency of a bubble near a rigid boundary. *Journal of the Acoustical Society of America*, 37(3):504–508, 1990.

[20] Paul A. Hwang, Ronald A. Roy, and Lawrence A. Crum. Artificial bubble cloud targets for underwater acoustic remote sensing. *Journal of Atmospheric and Oceanic Technology*, 12(6):1287–1302, 1995.

[21] Kelco. Xanthan gum technical booklet. Sent by fax, 2000. (Monsanto Company).

[22] Lawrence E. Kinsler, Austin R. Frey, Alan B. Coppens, and James V. Sanders. *Fundamentals of Acoustics*, pages 120–1, 184–8, 238–9. John Wiley and Sons, Inc., New York, 4th edition, 2000.

[23] V. O. Knudsen, R. S. Alford, and J. W. Emling. Underwater ambient noise. *Journal of Marine Research*, 7:410–429, 1948.

[24] Dean S. Langley and Philip L. Marston. Critical angle scattering of laser light from bubbles in water: measurements, models, and application to sizing of bubbles. *Applied Optics*, 23:1044, 1984.

[25] T. G. Leighton. *The Acoustic Bubble.* Academic Press, London, 1994.

[26] Timothy Leighton. Surf zone bubble spectrometry: The role of the acoustic cross section. *Journal of the Acoustical Society of America*, 110(5):2694, 2001.

[27] M. S. Longuet-Higgins and J. S. Turner. An 'entraining plume' model of a spilling breaker. *Journal of Fluid Mechanics*, 63:1–20, 1974.

[28] N. Q. Lu, A. Prosperetti, and S. W. Yoon. Underwater noise emissions from bubble clouds. *IEEE Journal of Oceanic Engineering*, 15(4):275–281, 1990.

[29] A. Mallock. The damping of sound by frothy liquids. *Proceedings of The Royal Society, Series A*, 84(A 572):391–395, 1910.

[30] Philip L. Marston. Critical angle scattering by a bubble: physical-optics approximation and observations. *Journal of the Optical Society of America*, 69:1205, 1979.

[31] Gustav Mie. Beiträge zür optik trüber medien, speziell kolloidaler metallösungen. *Annalen der Physik, vierte Folge*, 25(3):377–445, 1908.

[32] M. Minnaert. On musical air-bubbles and the sound of running water. *The London, Edinburgh and Dublin Philosophical Magazine and Journal of Science, Series 7*, 16:235–248, 1933.

[33] M. Nicholas, R. A. Roy, L. A. Crum, H. N. Oğuz, and A. Prosperetti. Sound emissions by a laboratory bubble cloud. *Journal of the Acoustical Society of America*, 95(6):3171–3182, 1994.

[34] Alan V. Oppenheim, editor. *Applications of Digital Signal Processing*, pages 206–210. Prentice-Hall, Inc., Englewood Cliffs, New Jersey, 1978.

[35] Andrea Prosperetti. Thermal effects and damping mechanisms in the forced radial oscillations of gas bubbles in liquids. *Journal of the Acoustical Society of America*, 61(1):17–27, 1977.

[36] Andrea Prosperetti. Bubble-related ambient noise in the ocean. *Journal of the Acoustical Society of America*, 84(3):1042–1054, 1988.

[37] Lord Rayleigh (J. W. Strutt). *The Theory of Sound.* Dover Publications, Inc., New York, 1945.

[38] Ronald A. Roy, William Carey, Michael Nicholas, Jeffrey Schindall, and Lawrence A. Crum. Low-frequency scattering from submerged bubble clouds. *Journal of the Acoustical Society of America*, 92(5):2993–2996, 1992.

[39] Jeffery A. Schindall. *Acoustic Scattering from Compact Bubble Clouds.* Ph.D Dissertation, The University of Mississippi, Oxford, 1995.

[40] Scion Corporation, www.scioncorp.com. *Scion Image Beta release 4.0.2*, 2000.

[41] D. L. Storm. Interfacial distortions of a pulsating gas bubble. In *Finite-amplitude wave effects in fluids, Proceedings of the Ultrasonics International 1973 Conference*, pages 234–239, Guildford, Surrey, 1974. IPC Science and Technology Press.

[42] Donald Leo Storm. *Frequency Spectrum of Finite-Amplitude Radiation from the Nonlinear Pulsation of a Gas Bubble.* Ph.D Dissertation, The University of Vermont, 1975.

[43] M. Strassberg. The pulsation frequency of nonspherical gas bubbles in liquids. *Journal of the Acoustical Society of America*, 25(3):536–537, 1953.

[44] H. C. van de Hulst. *Light Scattering by Small Particles.* Dover Publications, Inc., New York, 1st edition, 1981.

[45] Gordon M. Wenz. Acoustic ambient noise in the ocean: Spectra and sources. *Journal of the Acoustical Society of America*, 34(12):1936–1956, 1962.

[46] Norbert Wiener. *Extrapolation, Interpolation, and Smoothing of Stationary Time Series.* MIT Press, Cambridge, MA, 1949.

[47] Warren J. Wiscombe. Mie scattering calculations: Advances in technique and fast, vector-speed computer codes. Technical Report NCAR/TN-140+STR, National Center for Atmospheric Research, 1996.

[48] A. B. Wood. *A TextBook of Sound.* MacMillan, New York, 1st edition, 1930.

[49] S. W. Yoon, L. A. Crum, A. Prosperetti, and N. Q. Lu. An investigation of the collective oscillations of a bubble cloud. *Journal of the Acoustical Society of America*, 89(2):700–706, 1991.

[50] K. Yosioka and Y. Kawasima. Acoustic radiation pressure on a compressible sphere. *Acustica*, 5:167–173, 1955.

Vita

Ryan Daniel McCormick was born in Omaha, Nebraska on December 15, 1976. He attended elementary and junior high school in La Vista, a suburb of Omaha. In 1990, at the age of 13, he moved with his step-father, mother and brother and sisters, to Marietta, Georgia, a suburb of Atlanta. Here he attended Walton High School from 1990 to 1994, and graduated with highest honor.

In the fall of 1994, he enrolled as an undergraduate at the Georgia Institute of Technology majoring in civil engineering. During this time, he held a co-op job with Willmer Engineering, a geotechnical engineering firm in Atlanta. The duties of the job included quality assurance of poured concrete and soil compaction at building and landfill job sites, as well as determination of the cause of failure of a retaining wall behind a retail store.

In 1997, he changed majors to physics and began working in the laboratories of Drs. Phillip First and Tom Gaylord, which was a collaboration between solid state physics and electrical engineering. The lab specialized in the production and characterization of quantum heterostructure semiconductor devices via a scanning tunnelling microscope at cryogenic temperatures. The project he worked on for one and a half years involved design and production of a thermal and electron-gun metallic sputtering system, which was intended eventually to lead to study of magnetic monolayer semiconductor devices.

Upon graduation in 1999 with highest honors from Georgia Tech, Ryan decided to pursue a Master's Degree in Mechanical Engineering at Boston University in the field of Acoustics under the direction of Dr. Ronald Roy. Here he worked on projects involving propagation of sound through sand, measurement of acoustical scattering from small polyurethane spheres filled with bubbly Xanthan gel, and measurement of sound propagation through a column of bubbly gel, before settling on this project. The result of this endeavor is the work you hold now in your hands.

Permanent address: 2341 Chestnut Springs Trail; Marietta, GA, 30062